# 論文 / 著書情報
# Article / Book Information

| | |
|---|---|
| 題目(和文) | 1060nm 単一モード VCSEL とモードフィルタを使用した標準単一モードファイバー伝送に関する研究 |
| Title(English) | Study on standard single-mode fiber transmission using 1060nm VCSELs and mode filters |
| 著者(和文) | ZHANGBoXuan |
| Author(English) | Boxuan Zhang |
| 出典(和文) | 学位:博士(工学),<br>学位授与機関:東京工業大学,<br>報告番号:甲第12693号,<br>授与年月日:2024年3月26日,<br>学位の種別:課程博士,<br>審査員:植之原 裕行,小山 二三夫,中村 健太郎,西山 伸彦,宮本 智之,渡辺 正裕,粕川 秋彦 |
| Citation(English) | Degree:Doctor (Engineering),<br>Conferring organization: Tokyo Institute of Technology,<br>Report number:甲第12693号,<br>Conferred date:2024/3/26,<br>Degree Type:Course doctor,<br>Examiner:,,,,,, |
| 学位種別(和文) | 博士論文 |
| Type(English) | Doctoral Thesis |

博士論文

# Study on standard single-mode fiber transmission using 1060nm VCSELs and mode filters

# (1060nm 単一モード VCSEL とモードフィルタを使用した標準単一モードファイバー伝送に関する研究)

令和 5 年（2023 年）12 月版

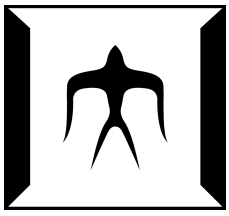


提出者

東京工業大学 工学院 電気電子系 電気電子コース

学籍番号　20D10440

**Boxuan Zhang**

指導教員　　小山二三夫特任教授

植之原裕行教授

# 内容

# Important abbreviations used in the thesis

| Abbreviations | Full words |
|---|---|
| VCSEL | Vertical cavity surface emitting laser |
| DFB | Distributed feedback |
| RMS | Root Mean Square |
| CW | Continuous Wave |
| BER | Bit Error Rate |
| SMF | Single-Mode Fiber |
| MMF | Multi-Mode Fiber |
| DBR | Distributed Bragg Reflector |
| SMSR | Side-Mode Suppression Ratio |
| RIN | Relative Intensity Noise |
| NRZ-OOK | Non-Return to Zero-On Off Keying |

# Important symbols used in the thesis

| Symbols | Physical meaning |
|---|---|
| $n_1$ | Fiber core refractive index |
| $n_2$ | Fiber cladding refractive index |
| $\theta_1$ | Incidence angle |
| $\theta_2$ | Refraction angle |
| $\theta_c$ | Critical angle for total reflection |
| $\Delta$ | Relative refractive index difference |
| $V$ | Normalized frequency |
| $a$ | Fiber core radius |
| $A_{01}$ | LP01 attenuation (dB/km) |
| $A_{11}$ | LP11 attenuation (dB/km) |
| $\alpha_{01}$ | LP01 attenuation ratio |
| $\alpha_{11}$ | LP11 attenuation ratio |
| $L$ | Fiber segment length divided by N connectors |
| $\eta$ | Coupling efficiency of connectors due to lateral offset |
| $\tau$ | Time delay between LP01 and LP11 |
| $r_e$ | Extinction ratio |
| $\sigma_0$ | Thermal noise |
| $\sigma_{01\_m}$ | Modal noise in LP01 for “mark” level |
| $\sigma_{01\_s}$ | Modal noise in LP01 for “space” level |
| $\sigma_{11}$ | Modal noise in LP11 |
| $\Delta f$ | Laser linewidth |
| $\beta$ | Spontaneous emission factor |
| $\Gamma$ | Optical confinement factor |
| $\eta_i$ | Internal quantum efficiency |
| $I_{th}$ | Threshold current |
| $h$ | Planck constant |
| $v$ | Light frequency |
| $\tau_m$ | Mirror energy loss |
| $e$ | Elementary charge |
| $\alpha$ | Linewidth enhancement factor |

# Chapter1
# Introduction

## 1.1 Background

### *1.1.1 Optical communication system based on conventional single-mode optical fiber and 1060nm single-mode VCSEL*

In today's society, the rapid development and advancement of network technology are leading the global technology trend. In recent years, various Internet-related applications and technologies have exploded, such as short video apps on smartphones [1-3], the metaverse concept [4-6], and video conferencing that has been widely used since the COVID-19 pandemic [7-10]. These new technologies are not only changing our lifestyles, but also posing new challenges to the optical communication demands of 5G networks and data centers [11-13]. The metaverse and video conferencing require high-quality real-time image or video transmission; short video apps perform real-time analysis of user preferences to deliver content precisely.

Against this backdrop, the demand for optical communication in 5G networks and data centers is soaring. On the one hand, the advent of 5G networks has made it possible for faster and larger capacity data transmission. However, this also means that data centers need to handle more data, which imposes higher requirements on the optical communication capability of data centers.

The figure below shows some common optical communication solutions and their pros and cons:

| Scheme | | Advantages | Disadvantages |
|---|---|---|---|
| Laser | Fiber | | |
| 1.3/1.5μm SM-DFB | Conventional SMF | • High speed<br>• Long distance | • High energy consumption |
| 850nm MM-VCSEL | MMF | • High speed<br>• Low power consumption | • Distance limitation (<500m) |
| 1060nm MM-VCSEL | MMF | • High speed<br>• Low power consumption | • Distance limitation (<500m) |
| 1.3/1.5μm SM-VCSEL | Conventional SMF | • High speed<br>• Low power consumption | • Sophisticated fabrication process |

Fig. 1-1 Schemes of optical transmission system

Among them, the most widely used system is based on a 1.3μm/1.5μm single-mode DFB laser and standard single-mode fiber [14-16]. This system can meet the needs of high-speed, long-distance transmission. However, the significant power consumption of DFB lasers are very unfavorable for their large-scale deployment. Compared with DFB lasers, VCSEL with a wavelength below 1.1μm have much lower power consumption [17-19]. A common scheme is using an 850nm or 1060nm multimode VCSEL in conjunction with a multimode fiber for high-speed transmission [20-25]. However, due to the influence of factors such as modal dispersion, this scheme can usually only transmit over a short distance. Additionally, 1.3μm/1.5μm single-mode VCSEL, due to its low power consumption characteristics, has also been proposed as a substitute for DFB laser. But its complex manufacturing process limits the possibility of its large-scale application [26-29].

Under these circumstances, we propose the solution of combining a 1060nm single-mode VCSEL with conventional single-mode fiber [30-33]. The 1060nm single-mode VCSEL has a low power consumption. It has very considerable prospects in large-scale deployments. Because the standard single-mode fiber is still utilized, it does not require significant changes to the existing optical communication system, which greatly saves

costs. However, since the single-mode cutoff frequency of conventional single-mode fiber is 1260nm, the fiber can support two modes [34], LP01 and LP11, at 1060nm, as shown in the figure below. The presence of the LP11 mode will inevitably have a negative impact on the system. This paper will conduct detailed research on this issue and propose solutions.

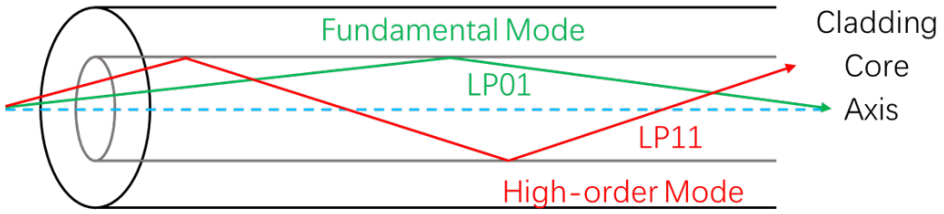


Fig. 1-2 Schematic diagram of 2-mode transmission

### *1.1.2 Structured cabling of large-scale data center*

Based on various applications and technologies of the Internet, their data ultimately needs to be processed and exchanged in data centers. This has given rise to large-scale data centers. 400G Ethernet is a common transmission scheme in large-scale data centers. The optical modules that realize 400G Ethernet are also constantly changing with the development of data centers. *Statista* has made predictions about its changes, as shown in the following figure:

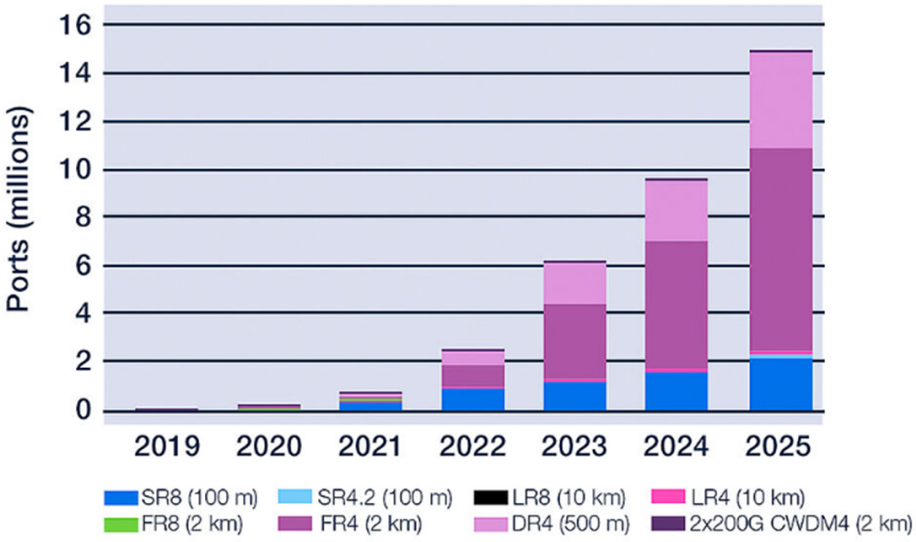


Fig. 1-3 Variance of 400G optical module [35]

As can be discerned from Fig.1-3, there is a marked annual increase in the adoption rates of the single-mode transmission systems, 400GBASE-FR4 (2km) and 400GBASE-DR4 (500m). In contrast, the expansion of the multimode transmission system, 400GBASE-SR8 (100m), has been sluggish. This can be primarily attributed to the evolving dynamics in data center sizes, wherein the need for longer transmission distances becomes more pronounced. Regrettably, multimode transmission systems, which are inherently designed for shorter distance transmission, are failing to meet these extended requirements.

It should be noted that the choice of cabling systems exhibits a direct correlation with the data center's scale [36-38]. In small data centers, point-to-point cabling is usually adopted. As shown in the following figure:

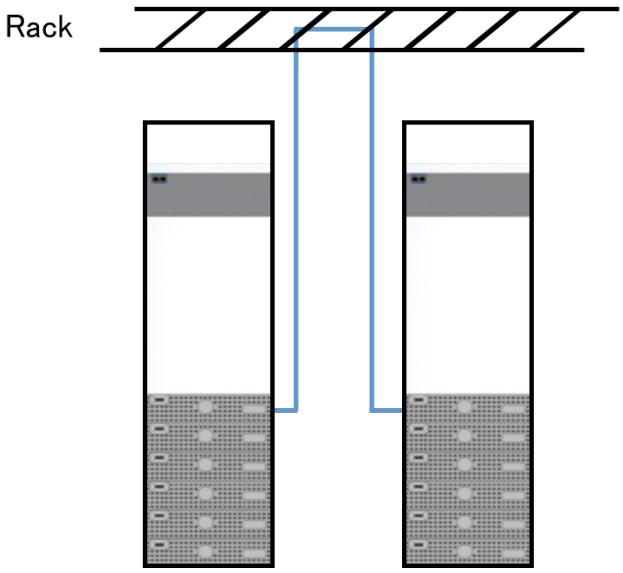


Fig. 1-4 Schematic diagram of point-to-point cabling

Point-to-point cabling refers to the direct connection between two terminals that need to transmit data using optical fibers. Its advantages are convenience, simple, and no need for fiber connectors, thus ensuring nearly lossless data transmission. However, the low flexibility and difficulty in management of the point-to-point cabling scheme are its biggest drawbacks, which also make it only suitable for small data centers.

In large-scale data centers, a structured cabling system is usually adopted. By introducing a distribution area as an intermediary, the connections between various terminals are managed through the distribution area. This method can significantly improve the flexibility of the cabling system. As shown in the following figure:

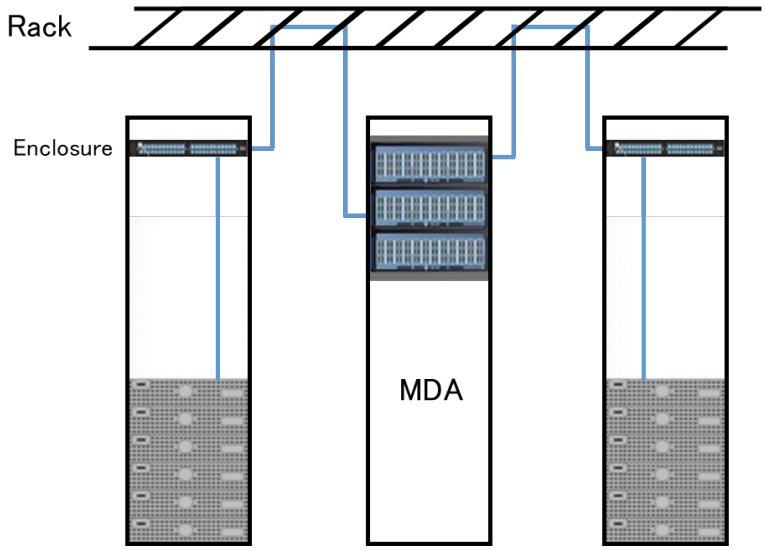


Fig. 1-5 Schematic diagram of structured cabling system. MDA: main distribution area

As depicted in Fig.1-5, the optical pathway connects optical fibers extending from two terminals to an enclosure housed within a cabinet. Subsequently, the output of this enclosure is directed towards the Main Distribution Area (MDA), where the final interconnection will be accomplished. Such a connection method provides the system with exceptional scalability and simplifies maintenance procedures. However, given the multiple "transfers" involved in the optical path, structured cabling necessitates the use of more fiber connectors compared to point-to-point cabling. For instance, in the system demonstrated in Fig.1-5, each of the two terminals traverses a cabinet enclosure and the Main Distribution Area to accomplish the connection, which includes a total of 4 connection points. The coupling loss attributable to these connection points could detrimentally impact communication. A detailed analysis of this system will be carried out in Chapter 2.

## 1.2 Previous work

### *1.2.1 Previous research of modal noise*

In the 1060nm optical communication system based on conventional single-mode fiber, the biggest issue is the modal noise caused by LP11 mode. There have been many related studies on this issue in the past [39-43]. We will analyze the key points of these studies in this section.

The transmission models employed in prior research are fundamentally congruent. The model posits that when light in the LP01/LP11 mode traverses a fiber connection experiencing coupling loss, the energy dissipated stimulates the LP11/LP01 mode. This concept is illustrated in the ensuing figure:

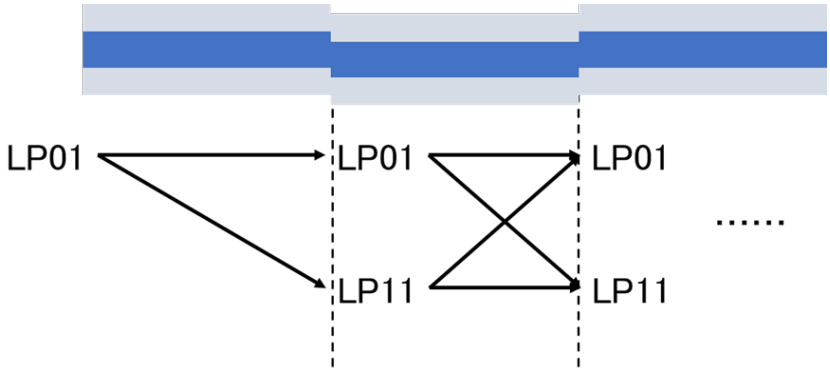


Fig. 1-6 Schematic diagram of 2-mode transmission model

In the case that interference arises between the excited LP01 and LP11 modes and the signal (LP01), this can instigate the occurrence of modal noise. This theory aligns with our understanding of the production of modal noise. However, we contend that these studies harbor considerable limitations and require further refinement.

Firstly, numerous previous studies postulate that the phase difference during interference is a random variable ranging from 0 to π. This phase difference originates from the distinct propagation constants of the LP01 and LP11 modes and alterations in environmental

factors such as temperature, which can induce phase shifts. We contend that this assumption is flawed as the phase changes instigated by propagation or environmental conditions are of low frequency. Under such conditions, if interference takes place, the resultant changes in light intensity are likewise low-frequency. This implies that the average optical power shifts slowly over time, leaving the root mean square (RMS) value of the optical power, i.e., the noise, unaffected. In our assessment, the noise source should be attributed to the phase noise of the laser, which is characterized by high-frequency phase changes. The interference of light translates this high-frequency phase variation into a high-frequency change in optical power, thereby causing modal noise.

Simultaneously, as these studies presume the phase difference to be a random variable, they do not need to consider the LP01 and LP11 mode light components generated at each fiber connection as independent entities. Typically, a rudimentary analysis using a model containing only 2 connection points, as depicted in Fig. 1-7, is performed. However, considering that the light generated at each connection point bears different phase differences compared to other lights within the system, when calculating the interference between any two lights, the phase difference varies accordingly. Therefore, it is imperative to establish a model incorporating a larger number of connection points. This model would facilitate a step-by-step analysis of the mode coupling process and phase differences and enable the derivation of a universal formula.

Secondly, in the equations presented in these studies, only the interference of the LP01 mode is typically calculated. Certain research suggests that due to the considerable transmission loss of the LP11 mode, the noise it engenders can be disregarded. While this assumption is tenable for long-distance communication, it may not hold for the optical paths within the data centers under our consideration, where the transmission distance

typically falls short of 2km. Hence, it becomes necessary to factor in the noise induced by the LP11 mode.

Thirdly, a prevailing consensus in most studies is that the transmission loss of the LP01 mode can be deemed negligible. However, our research indicates that in conventional single-mode fibers, the transmission loss of the LP01 mode hovers around 0.8dB/km. To attain more accurate computation results, particularly in instances where the transmission distance surpasses 1km, the loss attributable to the LP01 mode should be incorporated.

Grounded in these three insights, we have devised a more precise model, detailed in the second chapter, to facilitate a more comprehensive and accurate analysis of modal noise.

### *1.2.1 Analysis of different types of mode filter*

In addressing the complications introduced by the existence of higher-order modes in systems deploying single-mode transmission utilizing light below the cutoff wavelength within conventional single-mode fibers, mode filters emerge as a potent solution. The implementation of mode filters for the purging of high-order modes has the potential to significantly enhance system performance. The topic of mode filters has been the nexus of abundant research endeavors, resulting in the development of an array of mode filter prototypes [48-50].

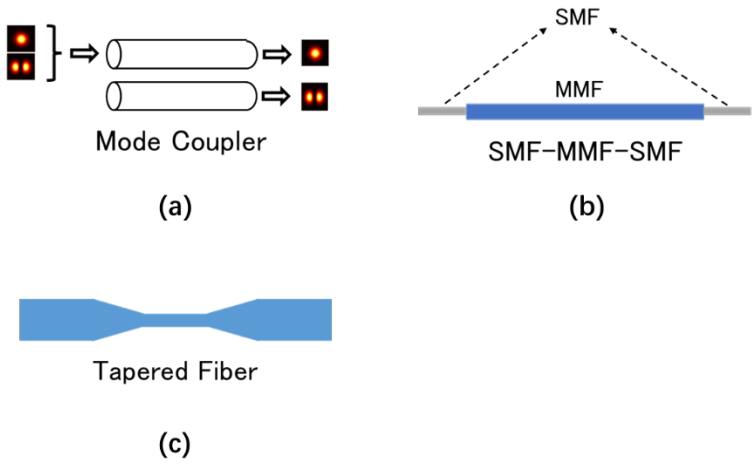


Fig. 1-7 Different types of mode filter: (a)by using mode coupler,(b)remove high-order modes by using single-mode fiber at operation wavelength,(c)by using tapered fiber

We shall expound on the underpinnings of mode filtering by showcasing three disparate archetypes of mode filters. Fig. 1-7(a) portrays a mode filter that capitalizes on a mode coupler. As light bearing both LP01 and LP11 modes impinges from the left-top port into the coupler, the LP11 mode light is transposed into the bottom waveguide, thereby effectuating the disentanglement of LP01 and LP11 modes. Fig.1-7(b) incorporates a single-mode fiber, calibrated with the operative wavelength, as a mode filter; it is interfaced at both termini of the multimode fiber to execute high-order mode filtering. Fig. 1-7(c) delineates the technique of fiber tapering, attenuating core dimensions, and in turn enabling the fiber segment to support solely the LP01 mode, culminating in efficacious higher-order mode eradication. These mode filter configurations render admirable performance, adeptly expunging higher-order modes extant within the system. However, these methodologies call for the integration of specialized apparatus and procedures into the system, inevitably amplifying expenditures and inducing certain insertion losses. In juxtaposition, we advocate that inducing fiber bends can elicit a

commensurate higher-order mode filtering effect. This premise is anchored in the observation that at a given bending radius, higher-order modes incur more pronounced bending losses [51]. Consequently, through judicious selection of the bending radius and the number of coils, it becomes theoretically plausible to sieve out higher-order modes whilst leaving the LP01 mode largely unscathed. Informed by this theoretical framework, we proffer two distinct mode filter designs, which are meticulously elucidated in Chapters 3 and 4.

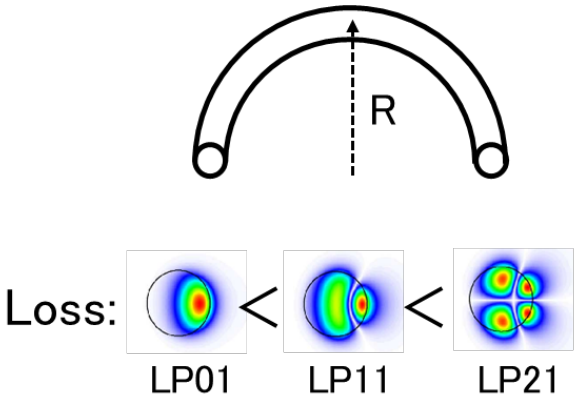


Fig. 1-7 Bending loss for different order of modes

## 1.3 Research purpose

Drawing from our appraisal of prior research, the primary objectives of our study can be delineated as follows:

- Establish a light transmission model predicated on a 1060nm single-mode VCSEL and conventional single-mode fiber. Undertake an analysis and computation of the potential emergence of the LP11 mode in the system and the concomitant modal noise. Moreover, calculate the power penalty induced by modal noise and prognosticate the performance augmentation attributable to mode filters.

- Develop a simulation model for mode filters based on bent fibers. Evaluate its effects and design experiments to measure the bending losses of LP01 and LP11 modes.
- Propose a mode filter design based on a 90-degree fiber array. Simulate its characteristics, identify potential problems and corresponding solutions in the mode filter, and conduct a theoretical analysis.
- Construct an experimental system using a 1060nm single-mode VCSEL and conventional single-mode fiber. Measure modal noise using an oscilloscope under continuous wave (CW) conditions, simultaneously testing the effectiveness of mode filters in reducing modal noise. Subsequently, compare and analyze the experimental results with the theoretical outcomes.
- Based on the same experimental system, conduct data transmission experiments, and analyze the impact of modal noise on system transmission capabilities by measuring eye pattern. Simultaneously, assess the effect of the mode filters by comparing the quality of the eye patterns with and without the use of mode filters.
- Expectations are to achieve 100 Gb/s transmission over a distance exceeding 1 km.

## 1.4 Organization of the thesis

- **Chapter 1**: Present the research background and previous research findings of the topic.
- **Chapter 2**: Introduce the theory of optical fiber modes, analyze coupling losses caused by optical fiber connectors, and establish a dual-mode transmission model to analyze mode coupling through fiber connectors and calculate modal noise and the resulting power penalty.
- **Chapter 3**: Present the principle of fiber bending loss, establish a simulation model

based on conventional single-mode fiber and calculate bending loss. Design a bending loss measurement experiment, propose the method of lateral-offset splicing of optical fibers to excite LP11 mode, the excitation ratio of LP11 mode is calculated and measured. Compare and analyze the experimental results and measurement results of fiber bending loss.

- **Chapter 4**: Propose a mode filter design based on a 90-degree fiber array. Predict the effect of this scheme through simulation and validate it through experiments. Analyze the issues of coupling loss that may be caused by fiber bending, and propose possible solutions to reduce coupling loss and evaluate their effects.
- **Chapter 5**: Establish an experimental system based on a 1060nm single-mode VCSEL and conventional single-mode fiber. Measure the modal noise and power penalty in the system under both continuous wave (CW) and OOK-NRZ modulation. The effect of the mode filter is also validated in the experiment. Compare and analyze the experimental results with the theoretical calculations.
- **Chapter 6**: Discuss the prospects of optical communication systems based on 1060nm single-mode VCSEL and conventional single-mode fiber, and summarize the thesis will be concluded.

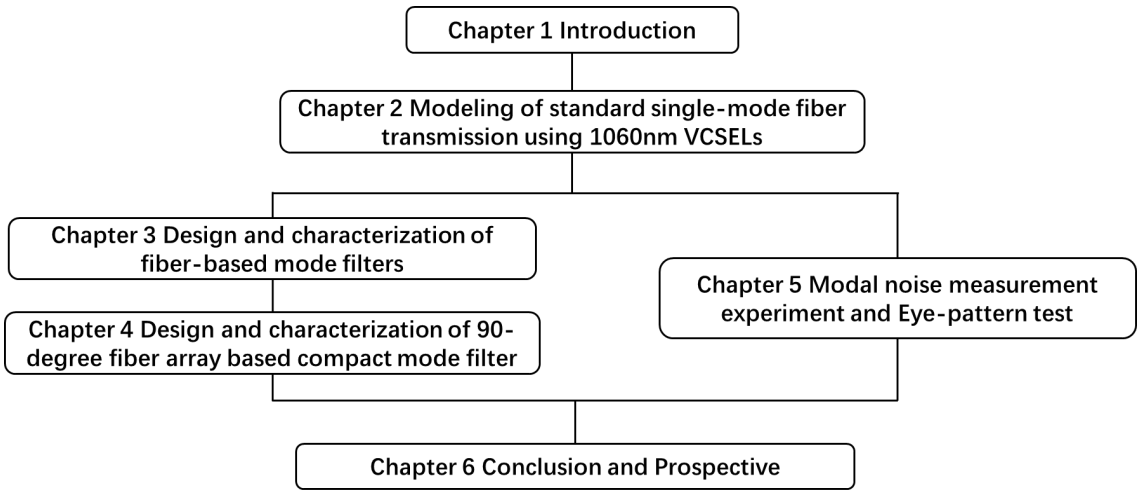

Fig 1-9 Organization frame of the thesis

## Reference in Chapter 1


1-1. N. P. Abdullah, M. Kassim and Y. M. Yussoff, "Analysis of Internet Application Services Traffic on WAN Metro-E Network," ICSGRC. IEEE, (2022).

1-2. D. Zhang, M. Zuo, H. Chen, D. Ge, Z. Feng, B. Yan, D. Wang, H. Shi, S. Cao, Y. Li, L. Han, B. Ye, Y. He, T. Wang and H. Li, "Technological Prospection and Requirements of 800G Transmission Systems for Ultra-Long-Haul All-Optical Terrestrial Backbone Networks," J. Lightwave Technol. 41(12), 3774-3782 (2023).

1-3 M. Han and X. Zhang, "Prospects for the advancement of the TikTok in the age of 5G communication," CMI, (2020).

1-4 H. Daki, A. El Hannani, A. Aqqal, A. Haidine and A. Dahbi, "Big Data management in smart grid: concepts, requirements and implementation," J. Big Data 4(1), 1-19 (2017).

1-5 A. M. Aslam, R. Chaudhary, A. Bhardwaj, I. Budhiraja, N. Kumar and S. Zeadally, "Metaverse for 6G and Beyond: the next revolution and deployMent ChallenGes," IEEE Internet Things Mag. 6(1), 32-39 (2023).

1-6 Y. Cai, J. Llorca, A. M. Tulino, and A. F. Molisch, "Compute- and Data-Intensive Networks: The Key to the Metaverse," 6GNet, (2022).

1-7 R. Miglani, J. S. Malhotra, A. K. Majumdar, F. Tubbal, and R. Raad, "Multi-Hop Relay Based Free Space Optical Communication Link for Delivering Medical Services in Remote Areas," IEEE Photon. J. 12(4), 1-21 (2020).

1-8 F. Q. Kareem, S. RM Zeebaree, H. I. Dino, M. A. M Sadeeq, Z. N. Rashid, D. A. Hasan, and K. H. Sharif, "A survey of optical fiber communications: challenges

and processing time influences," Asian J. Res. Comput. Sci. 7(4), 48-58 (2021).

1-9 M. Singh, A. Atieh, A. Grover, and O. Barukab, "Performance analysis of 40 Gb/s free space optics transmission based on orbital angular momentum multiplexed beams," Alex. Eng. J. 61(7), 5203-5212 (2022).

1-10 D. Lai, Z. Li, D. Zou, X. Yi, Z. Li, and F. Li, "Transmission of 50-Gb/s/λ PAM-4 over 100-km SMF for LR-PON utilizing Low Complexity Polarization-insensitive Quasi-coherent Receiver," Asia Commun. Photon. Conf., (2020).

1-11 J. Wei, T. Rahman, S. Calabrò, N. Stojanovic, L. Zhang, C. Xie, Z. Ye, and M. Kuschnerov, "Experimental demonstration of advanced modulation formats for data center networks on 200 Gb/s lane rate IMDD links," Opt. Express 28(23), 35240-35250 (2020).

1-12 T. Sudo, Y. Matsui, G. Carey, A. Verma, D. Wang, V. Lowalekar, M. Kwakernaak, F. Khan, N. Dalida, R. Patel, et al., "Challenges and opportunities of directly modulated lasers in future data center and 5G networks," Opt. Fiber Commun. Conf., (2021).

1-13 E. El-Fiky, A. Samani, M. S. Alam, M. Sowailem, O. Carpentier, M. Jacques, L. Guenin, D. Patel, and D. V. Plant, "A 4-lane 400 Gb/s silicon photonic transceiver for intra-datacenter optical interconnects," OFC, (2019).

1-14 N. Sasada, T. Nakajima, Y. Sekino, A. Nakanishi, M. Mukaikubo, M. Ebisu, M. Mitaki, S. Hayakawa, and K. Naoe, "Wide-temperature-range (25--80° C) 53-Gbaud PAM4 (106-Gb/s) operation of 1.3-μm directly modulated DFB lasers for 10-km transmission," J. Lightwave Technol. 37(7), 1686-1689 (2019).

1-15 T. Nakajima, M. Onga, Y. Sekino, A. Nakanishi, N. Sasada, S. Hayakawa, S. Hamada, and K. Naoe, "106-Gb/s PAM4 Operation of Directly Modulated DFB

Lasers from 25 to 70° C for Transmission Over 2-km SMF in the CWDM Range," J. Lightwave Technol. 40(6), 1815-1820 (2022).

1-16 Q. Tang, Y. Liu, L. Zhang, X. La, S. Liang, L. Zhao, and W. Wang, "25 Gb/s directly modulated widely tunable 1.3 μm dual wavelength DFB laser for THz communication," IEEE Photon. Technol. Lett. 32(7), 410-413 (2020).

1-17 K. Iga, J. Tatum, "Single-Mode VCSELs for Communications Applications," VCSEL Industry: Communication and Sensing, pp. 189, (2021), John Wiley & Sons.

1-18 M. Scalabroni, "VCSEL-based transmission system for optical and RF convergence in automotive applications," Italy, (2019).

1-19 H. R. Ibrahim, A. M. A. Hassan, X. Gu, S. Shinada, M. Ahmed, and F. Koyama, "1060nm Single-mode Metal-aperture VCSEL Array with Transverse Resonance and Low Power Consumption below 50 fJ/bit," ECOC, (2021).

1-20 J. Wang, Y. Ji, Z. Yang, H. Hu, J. Chen, H. Li, F. Li, S. Li, J. Kapraun, C. Shen, et al., "300-m Multimode Fiber Transmission of 106Gbps PAM-4 Using 850nm High-Contrast-Grating Few-mode VCSELs," ECOC, (2022).

1-21 W.-C. Lo, W.-L. Wu, C.-H. Cheng, H.-Y. Wang, C.-T. Tsai, C.-H. Wu, and G.-R. Lin, "Effect of chirped dispersion and modal partition noise on multimode VCSEL encoded with NRZ-OOK and PAM-4 formats," IEEE J. Sel. Top. Quantum Electron. 28(1: Semiconductor Lasers), 1-9 (2021).

1-22 J.-H. Weng, W.-C. Lo, J. Wang, P. Qiao, C.-C. Shen, C.-H. Cheng, C. J. Chang-Hasnain, and G.-R. Lin, "Effect of Transmission-Line Contact Length on the 50-Gbit/s Data Encoding Performance of a Multimode VCSEL," Photonics 9(2), 114 (2022).

1-23 J. Lavrencik, E. Simpanen, S. Varughese, A. Melgar, V. A. Thomas, J. S. Gustavsson, W. V. Sorin, S. Mathai, M. Tan, A. Larsson, et al., "Error-free 100Gbps PAM-4 transmission over 100m OM5 MMF using 1060nm VCSELs," Opt. Fiber Commun. Conf., pp. M1F-3, (2019).

1-24 B. Wang, W. V. Sorin, P. Rosenberg, L. Kiyama, S. Mathai, and M. R. T. Tan, "4× 112 Gbps/Fiber CWDM VCSEL arrays for co-packaged interconnects," J. Lightwave Technol. 38(13), 3439-3444 (2020).

1-25 A. Khurana, V. A. Thomas, J. T. Gallo, and S. E. Ralph, "Impact of Link Limitations in 50 Gbps PAM-2 VCSEL MMF Links: Alignment, Equalization and Fiber Type," CLEO: Sci. Innovations, pp. SM3J-1, (2022).

1-26 W. Soenen, R. Vaernewyck, X. Yin, S. Spiga, M.-C. Amann, K. S. Kaur, P. Bakopoulos, and J. Bauwelinck, "40 Gb/s PAM-4 transmitter IC for long-wavelength VCSEL links," IEEE Photon. Technol. Lett. 27(4), 344-347 (2014).

1-27 J. Zhou, C. Yu, and H. Kim, "Transmission performance of OOK and 4-PAM signals using directly modulated 1.5-μm VCSEL for optical access network," J. Lightwave Technol. 33(15), 3243-3249 (2015).

1-28 F. Karinou, C. Prodaniuc, N. Stojanovic, M. Ortsiefer, A. Daly, R. Hohenleitner, B. Kögel, and C. Neumeyr, "Directly PAM-4 Modulated 1530-nm VCSEL Enabling 56 Gb/s/λ Data-Center Interconnects," IEEE Photon. Technol. Lett. 27(17), 1872-1875 (2015).

1-29 A. Malacarne, V. Sorianello, A. Daly, B. Kögels, M. Ortsiefer, C. Neumeyr, M. Romagnoli, and A. Bogoni, "Performance analysis of 40-Gb/s transmission based on directly modulated high-speed 1530-nm VCSEL," IEEE Photon. Technol. Lett. 28(16), 1735-1738 (2016).

1-30 E. Simpanen, J. S. Gustavsson, A. Larsson, M. Karlsson, W. V. Sorin, S. Mathai, M. R. Tan, and S. R. Bickham, "1060 nm single-mode VCSEL and single-mode fiber links for long-reach optical interconnects," J. Lightwave Technol. 37(13), 2963-2969 (2019).

1-31 S. Hu, X. Gu, H. R. Ibrahim, and F. Koyama, "5-km Single-mode Fiber Data Transmission with 1060nm Single-mode Intra-cavity Surface Relief Transverse Coupled Cavity VCSELs," ISLC, pp. 1-2, (2022).

1-32 L. Dong, X. Gu, and F. Koyama, "16-ch 1060-nm Single-mode Bottom-emitting Metal-aperture VCSEL Array for Co-packaged Optics," OFC, pp. 1-3, (2023).

1-33 C. Ge, B. Zhang, X. Gu, S. Kinoshita, and F. Koyama, "Full 3-inch Wafer Processed 1060 nm Single-mode Transverse Coupled-cavity VCSEL for Data Transmission in Standard 1300nm Single-mode Fiber," Optical Fiber Commun. Conf., Th2A-9, (2023).

1-34 M.-J. Li, K. Li, X. Chen, S. K. Mishra, A. A. Juarez, J. E. Hurley, J. S. Stone, C.-H. Wang, H.-T. Cheng, C.-H. Wu, et al., "Single-mode VCSEL transmission for short reach communications," J. Lightwave Technol. 39(4), 868-880 (2020).

1-35 " https://osi.rosenberger.com/fr/news-media/400-gigabit-800g-ethernet/ "

1-36 C. F. Lam, H. Liu, and R. Urata, "What devices do data centers need?," Optical Fiber Commun. Conf., pp. M2K-5, (2014).

1-37 L. Schares, D. M. Kuchta, and A. F. Benner, "Optics in future data center networks," in 18th IEEE Symposium on High Performance Interconnects, pp. 104-108, (2010).

1-38 S. Pogorelskiy and I. Kocsis, "Automation for structured cabling system in data centers using Building Information Modelling," Int. Rev. Appl. Sci. Eng., (2022).

1-39 P. M. Shankar, "Effect of modal noise on single mode fiber optic networks," Opt. Commun. 65(5), 347-350 (1988).

1-40 G. A. Olson and R. M. Fortenberry, "Modal noise in single-mode fiber-optic systems with closely spaced splices," Fiber Integr. Opt. 9(3), 237-244 (1990).

1-41 FT Stone, "Modal noise in single-mode-fiber communication system," in Fiber Optics: Short-Haul and Long-Haul Measurements and Applications II, vol. 500, pp. 17-22, (1984).

1-42 JC Goodwin and PJ Vella, "Modal noise in short fiber sections," Journal of Lightwave Technol. 9(8), 954-958 (1991).

1-43 DG Duff, FT Stone, and J. Wu, "Measurements of modal noise in single-mode lightwave systems," Optical Fiber Commun. Conf., pp. TUO1, (1985).

1-44 J. L. Gimlett and N. K. Cheung, "Effects of phase-to-intensity noise conversion by multiple reflections on gigabit-per-second DFB laser transmission systems," J. Lightwave Technol. 7(6), 888-895 (1989).

1-45 M. R. Salehi and B. Cabon, "Theoretical and experimental analysis of influence of phase-to-intensity noise conversion in interferometric systems," J. Lightwave Technol. 22(6), 1510 (2004).

1-46 M. Tur and E. L. Goldstein, "Dependence of error rate on signal-to-noise ratio in fiber-optic communication systems with phase-induced intensity noise," J. Lightwave Technol. 7(12), 2055-2058 (1989).

1-47 M. Li, "MMF for high data rate and short length applications," in OFC 2014, pp. 1-3, (2014).

1-48 Z. Haas and M. A. Santoro, "A mode-filtering scheme for improvement of the bandwidth-distance product in multimode fiber systems," J. Lightwave Technol.

11(7), 1125-1131 (1993).

1-49 Z. Tian, C. Chen, and D. V. Plant, "850-nm VCSEL transmission over standard single-mode fiber using fiber mode filter," IEEE Photonics Technol. Lett. 24(5), 368-370 (2011).

1-50 Donlagic, "In-line higher order mode filters based on long highly uniform fiber tapers," J. Lightwave Technol. 24(9), 3532-3539 (2006).

1-51 C. Schulze, A. Lorenz, D. Flamm, A. Hartung, S. Schröter, H. Bartelt, and M. Duparré, "Mode resolved bend loss in few-mode optical fibers," Opt. Express 21(3), 3170-3181 (2013).

# Chapter2

# Modeling of standard single-mode fiber transmission using 1060nm VCSELs

In this chapter, we commenced by elucidating the theory of light transmission and mode theory in step-index refractive index fibers. Subsequently, we established a transmission model for 1060nm light predicated on conventional single-mode fiber and scrutinized the issue of crosstalk in this system instigated by mode coupling. We derived the expressions depicting the variation of optical intensity during the transmission process. Our attention was particularly riveted on the modal noise engendered by crosstalk and the power penalty engendered by this modal noise, leading us to perform corresponding analyses and computations. Concurrently, we advocated the utilization of a mode filter as a remedy to the crosstalk issue, and conducted pertinent analyses and calculations to quantify its efficacy.

## 2.1 Optical fiber mode theory

### *2.1.1 Principle of light transmission in fiber*

Step-index fibers are a type of optical fiber with a uniform refractive index within the core and a sharp decrease in the refractive index at the cladding. As shown by Fig.2-1. The refractive index of core and cladding is presented as $n_1$ and $n_2$, respectively.

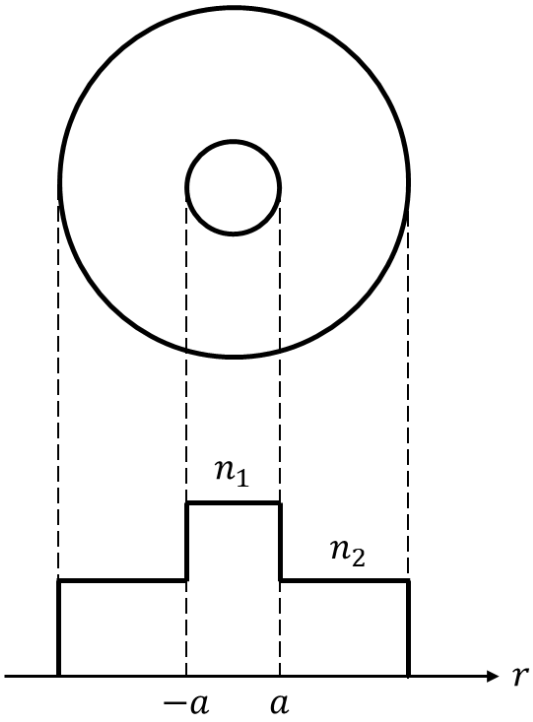


Fig. 2−8 Step-index fiber refractive index distribution

This configuration enables light to travel in almost straight lines, or modes, along the fiber. Understanding the theory behind this light transmission provides key insights into the design, application, and optimization of fiber optic communications systems.

The fundamental principle governing light transmission in step-index fibers is total internal reflection. As shown in Fig.2-2

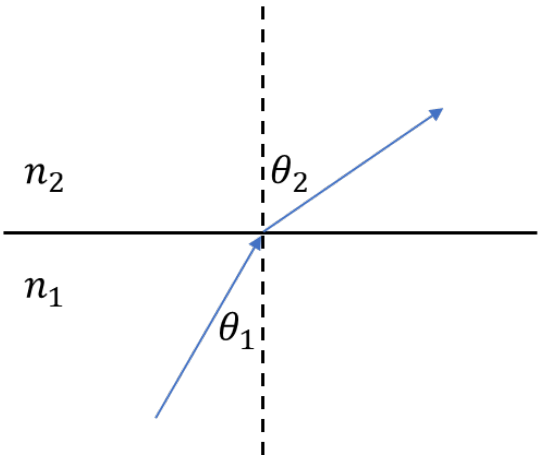


Fig. 2-2 Total internal reflection

When light travels from a medium with a higher refractive index ($n_1$) to a medium with a lower refractive index ($n_2$), and the incidence angle exceeds a critical angle ($\theta_c$), the light will be totally internally reflected. This phenomenon can be described by Snell's law:

$$n_1 \sin\theta_1 = n_2 \sin\theta_2 \qquad (2-1)$$

where $\theta_1$ is the incidence angle and $\theta_2$is the refraction angle. The critical angle ($\theta_c$) is derived when $\theta_2$ equals 90 degrees, which gives:

$$\theta_c = \arcsin\frac{n_2}{n_1} \qquad (2-2)$$

In step-index fibers, the core (with refractive index $n_1$) and the cladding (with refractive index $n_2$) play crucial roles. If the incidence angle ($\theta_1$) is greater than the critical angle ($\theta_c$), light will propagate along the fiber through total internal reflection.

When light is coupled into the fiber from air at an incidence angle $\theta_i$. Suppose $\theta_i$ just satisfies the total reflection condition, i.e., $\theta_i = \frac{\pi}{2} - \theta_c$. As shown in Figure 2-3.

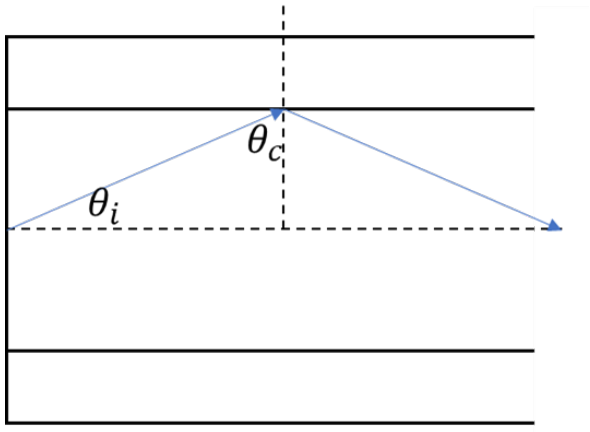


Fig. 9-3 Light propagation within the fiber

It can be obtained:

$$\sin\theta_i = \cos\theta_c = \sqrt{1-\frac{n_2^2}{n_1^2}} = \sqrt{2\Delta} \qquad (2-3)$$

In Eq.2-3, Δ is referred to as the relative refractive index difference of the fiber.

$$\Delta = \frac{n_1^2 - n_2^2}{2n_1^2} \approx \frac{n_1 - n_2}{n_1} \qquad (2-4)$$

In the realm of weakly guiding fibers, given the close proximity between $n_1$ and $n_2$, the portion following the approximation in Eq.2-4 remains valid. Upon examining the relationship between Δ, the incidence angle $\theta_i$ from air, and the critical angle of total reflection $\theta_c$, it is clear that a larger Δ precipitates a smaller $\theta_c$, signaling a stronger confinement of light within the fiber.

### *2.1.2 Theoretical analysis of fiber optic modes*

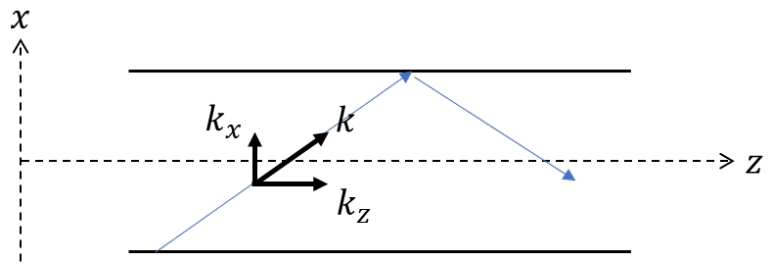


Fig. 2-4 Wave transmission along fiber

As demonstrated in Fig.2-4, the radial direction of the fiber is designated as the z-direction. Hence, when light propagates in the fiber, its wave vector k can be decomposed into $k_z$ along the propagation direction and $k_x$ perpendicular to the propagation direction (for the sake of simplifying the discussion, we posit here that light is confined solely within the k-x plane, with no light in the y direction). Radially, the light will continue to transmit along the fiber until it reaches its terminus. In the transverse direction, light will ricochet between the upper and lower interfaces of the core. Stable oscillations can only be established when the light ricocheting in the transverse direction can form standing waves, as depicted in Fig.2-5.

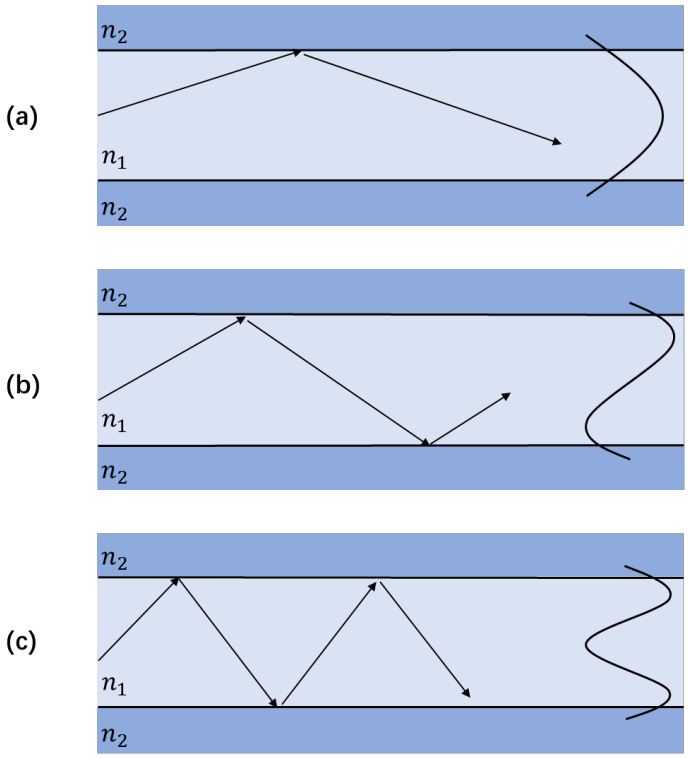


Fig. 2-5 Different order of mode in fiber

Only light that meets a specific incidence angle can satisfy the transverse resonance condition and form standing waves [1]. The formula is expressed as shown in Eq.2-5

$$2k_x d + 2\varphi_2(\theta_1) = 2m\pi \qquad (2-5)$$

In the given formula, $d$ denotes the core diameter. $\varphi_2(\theta_1)$ signifies the phase shift incurred as the light reflects at the core-cladding interface, a function connected to the incidence angle $\theta_1$. If the light reflects back-and-forth transversely for a complete period and the phase change is integral multiple of 2π, a stable standing wave can be established, termed as transverse resonance.

When m = 0, a single antinode exists within the fiber, corresponding to the condition where the mode present in the fiber is identified as the fundamental mode (LP01). Conversely, when m = 1, the system exhibits two antinodes, resulting in the classification of the mode as the first-order higher-order mode (LP11), and the pattern extends in similar

fashion for increasing values of m.

Distinct wave modes exhibit different transverse field (standing wave) distributions. Concurrently, due to varying $k_x$, the propagation constant $\beta = k_x$ also varies, implying that different wave modes possess distinct propagation constants, and thus, different transmission speeds. In specific scenarios, different modes might share the same propagation constant, a phenomenon known as degeneracy. Because the $\varphi_2(\theta_1)$ of the transverse electric (TE) and transverse magnetic (TM) modes may not align, even when m is identical, their field distributions can vary, therefore corresponding to different modes. These modes are designated as TE_m and TM_m, with 'm' serving as a subscript. When the angle of incidence, $\theta_1$, is less than the critical angle ($\theta_c$) for total internal reflection, a part of the light refracts from the core into the cladding. As this light continues to travel along the fiber, its energy is depleted after undergoing multiple refractions. Such a wave pattern is referred to as a radiation mode.

Within the same fiber, different wavelengths will result in different critical angles for total internal reflection. The larger the wavelength, the smaller the critical angle, and hence the fewer the guided modes that can be retained within the fiber. When the wavelength exceeds a certain value, only one mode, the fundamental mode, can exist in the fiber. That value is referred to as the cut-off wavelength for single-mode operation in that fiber.

As previously discussed, the larger the fiber's relative refractive index difference (Δ), the stronger its capacity to confine light, which implies that the fiber can support a greater number of modes. The quantity of modes supported within the fiber, besides being dependent on the light's wavelength and the difference in refractive indices, also relates to the size of the fiber. These factors can be articulated through a single equation.

$$\mathrm{V} = \frac{2\pi a}{\lambda}\sqrt{n_1^2 - n_2^2} \qquad (2-6)$$

EQ.2-6 is known as the fiber's normalized frequency (V), where '$a$' is the radius of the fiber core. The relationship between the vector modes within the fiber and V can be reviewed in the following table.

Table 2-1 Vector modes under different normalized frequencies

| **V** | **Vector Mode** |
|---|---|
| 0 | $HE11_x$, $HE11_y$ |
| 2.405 | TE01, TM01, $HE21_x$, $HE21_y$ |
| 3.832 | $EH11_x$, $EH11_y$, $HE31_x$, $HE31_y$ |
| 5.136 | $HE12_x$, $HE12_y$ |
| 5.520 | $EH21_x$, $EH21_y$, $HE41_x$, $HE41_y$ |
| 6.380 | TE02, TM02, $HE22_x$, $HE22_y$ |

The x and y subscripts in the table correspond to identical vector modes with distinct polarization states. The quantity of vector modes supported varies with different normalized frequency values. When $0 \leq V < 2.405$, only two HE11 modes with different polarization states can be supported. For $2.405 \leq V < 3.832$, the fiber can support the initial two groups of vector modes indicated in Table 2-1. This pattern continues accordingly. Fig.2-6 illustrates a schematic of the first two groups of vector modes within the fiber [2].

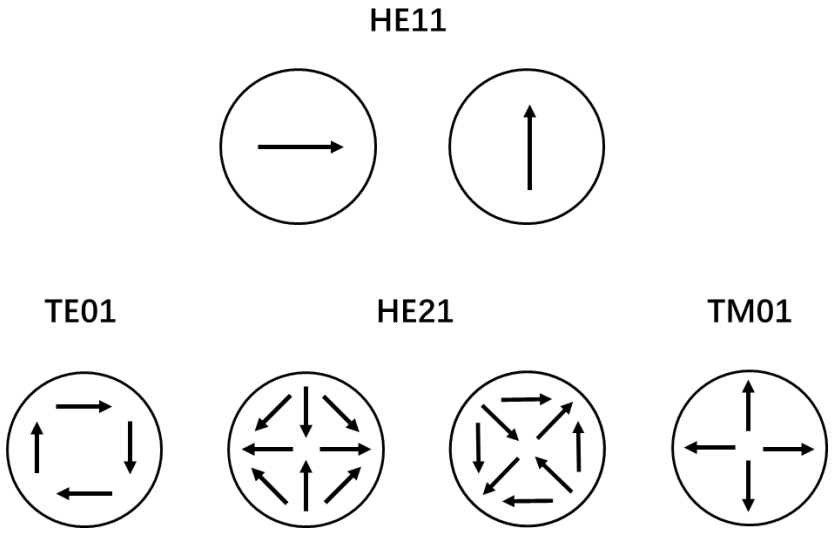


Fig. 2-6 Vector modes for 0≤V<3.832

Vector modes are the product of a meticulous solution to the wave equation for the electromagnetic field within the step-index fiber, devoid of any approximations. Owing to the intricate distribution (both in magnitude and direction) and mathematical expression of the transverse field components of vector modes across the fiber's cross-section, they are not advantageous for fiber problem analysis.

In weakly guiding fibers, given the nearly identical refractive indices of the core and cladding, the critical angle for total internal reflection approximates 90 degrees. As a result, the trajectory of light propagation aligns almost parallel to the fiber axis, and the orientations of the electric and magnetic fields are nearly perpendicular to the fiber axis. Consequently, the distribution of the electromagnetic field within weakly guiding fibers approximates transverse electromagnetic (TEM) waves. Therefore, the vector mode of weakly guiding fibers can be simplified into linearly polarized (LP) modes.

Figure 2-7 illustrates the process of the second group of vector modes (2.405≤V<3.832) degenerating into linearly polarized modes. The degenerated linearly polarized mode is known as the first order higher mode, LP11 mode. The LP11 mode is four-fold degenerate,

each with distinct 2-lobe intensity distributions and polarization directions.

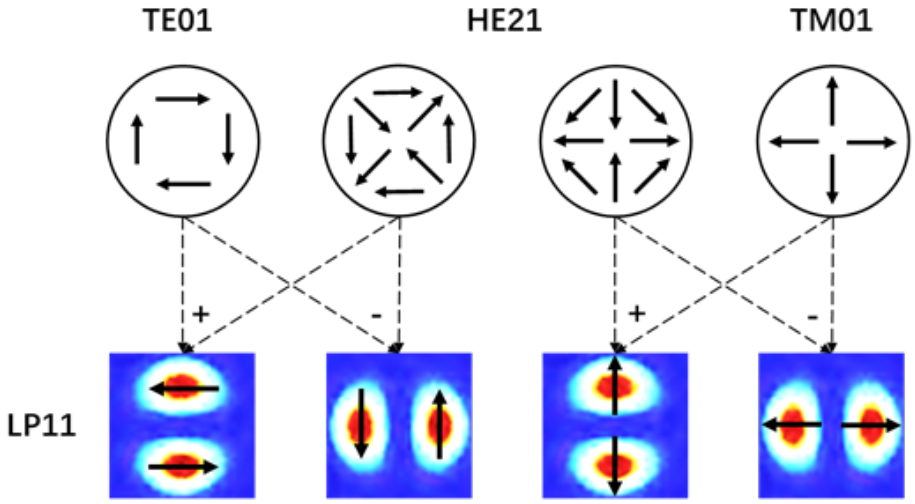


**Fig. 2-7 The degeneration process of the LP11 mode**

The '+' and '-' in the figure represent constructive and destructive interference respectively. They will cause the intensity distribution of the resulting LP11 mode to present a 90-degree rotation. The relationship between the linearly polarized mode and the normalized frequency (V) is shown in the following table.

Table 2-2 Linearly polarized modes under different normalized frequencies

| LP mode | V | Degeneracy |
|---|---|---|
| LP01 | 0 | 2 |
| LP11 | 2.405 | 4 |
| LP21 | 3.832 | 4 |
| LP02 | 5.136 | 2 |
| LP31 | 5.520 | 4 |
| LP12 | 6.380 | 4 |

When V is less than 2.405, only the LP01 mode, also known as the fundamental mode, will be present, indicating that the system is in single-mode transmission. According to Eq.(2-6), employing a shorter wavelength in the same fiber will result in a larger value of

V. This is why the single-mode cut-off wavelength is specified in single-mode fiber product manuals. In other words, when the operational wavelength is below this value, the fiber will support higher-order modes.

Given that the envisioned system in our study involves the transmission of light at a wavelength of 1060nm through conventional single-mode fibers with a cut-off wavelength of 1260nm, the calculated normalized frequency (V) resides between 2.405 and 3.832. Consequently, this system contains both the fundamental mode (LP01) and the first high-order mode (LP11).

## 2.2 Two-modes transmission model and effect of mode filter

### *2.2.1 Mode coupling and expression derivation in 2-mode transmission*

Mode coupling within optical fibers denotes the process whereby energy migrates from one propagating mode to another [3]. This phenomenon significantly determines the operational behavior of the fiber, impacting crucial performance attributes such as dispersion, bandwidth, and holistic system capacity.

The genesis of mode coupling lies in mismatches within the modal field of the optical fiber. A multitude of factors such as pressure variations, bending, temperature fluctuations, impurities within the fiber, and refractive index aberrations induced by manufacturing processes can catalyze inconsistencies in the modal field, thus instigating mode coupling. Nevertheless, the mode coupling engendered by the aforementioned factors is comparatively minute and is frequently considered an ideal state, hence disregarded. In optical fiber transmission systems, the most prevalent and significant location for mode coupling manifestation is at the fiber connection points, such as fiber connectors or fiber

fusion splices.

The reasons for mode coupling at the connection point can be divided into two categories. The first is connecting fibers with different mode field diameters, such as multimode fibers with larger mode fields and single-mode fibers with smaller mode fields [4]. The difference in mode field size will inevitably lead to a mismatch in the mode field, resulting in coupling. The second is imperfect connections of the fiber [5]. For instance, the longitudinal gaps, angles, and lateral displacements between the two end faces at the connection point can all lead to mode coupling, as depicted in the following figure.

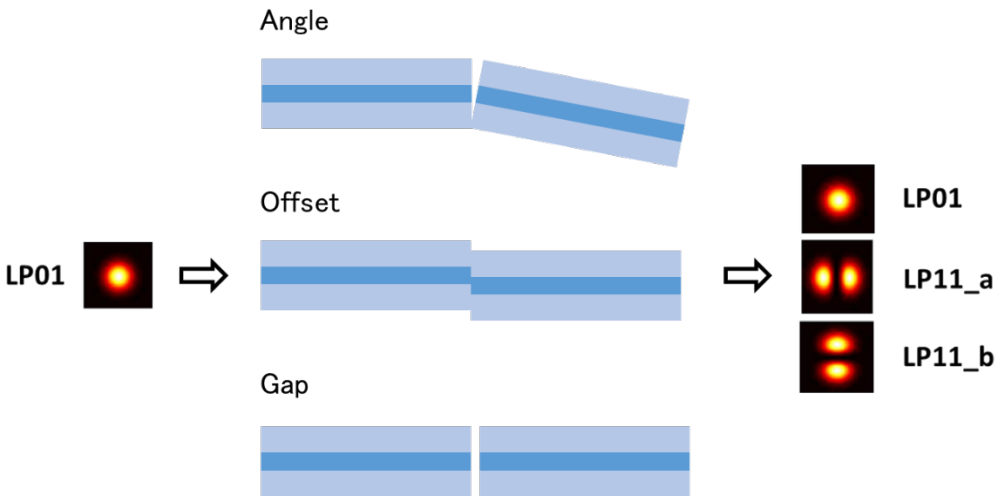


Fig. 2-8 The origins of mode coupling in the fiber connection

Among the three reasons shown in Fig.2-8, the coupling caused by lateral offset far exceeds the other two. Hence, in this study, we assume that mode coupling is solely induced by the lateral offset at the fiber junctions.

As previously mentioned, the focus of this study lies on an optical communication system that integrates a 1060nm single-mode VCSEL with conventional single-mode fibers. Two modes, LP01 and LP11, are concurrently supported within the fiber. Consequently, mode coupling triggers a certain degree of energy transfer, oscillating between the LP01 and

LP11 modes [6]. The process is illustrated in the following diagram.

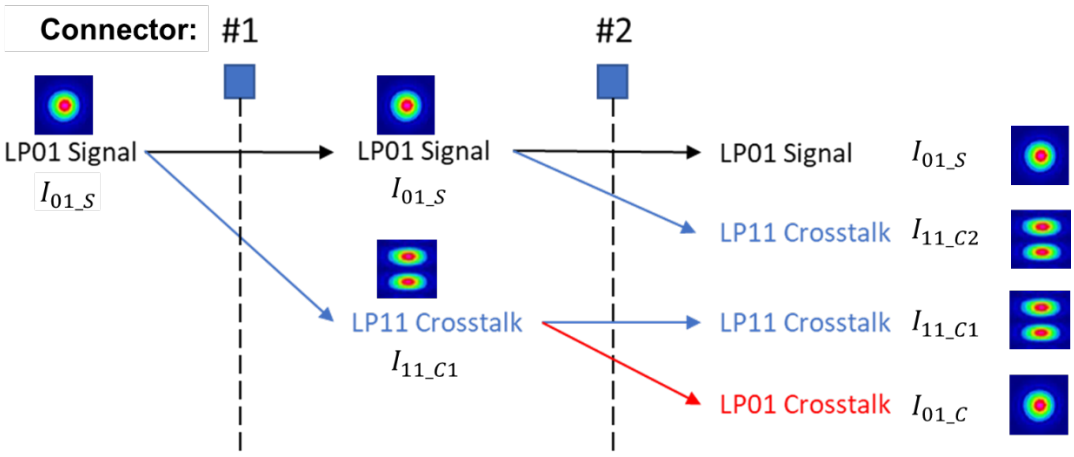


Fig. 2-9 Mode coupling process between LP01 and LP11

Taking an optical system that only includes two imperfect fiber connectors (with coupling efficiency less than 100%) as an example, we assume the incident light is the fundamental mode (LP01), and mode coupling only occurs within the fiber connectors.

Upon reaching the first fiber connector (#1), the incident LP01 mode signal light ($I_{01\_S}$) is subjected to coupling loss, resulting in the dissipation of a portion of its energy. This dissipated energy is converted into the LP11 mode, generating the LP11 mode crosstalk light ($I_{11\_C1}$). Consequently, $I_{11\_C1}$ and $I_{01\_S}$ transmit from the first connector to the second in unison. Upon encountering the second connector, the signal light once more undergoes coupling loss, engendering an additional LP11 crosstalk light ($I_{11\_C2}$). Simultaneously, the $I_{11\_C1}$ originating from the first connector also experiences coupling loss at the second connector, with the energy lost from this loss being recoupled back into the LP01 mode ($I_{01\_C}$).

It is crucial to underscore that the LP11 mode and LP01 mode harbor different propagation constants, hence facilitating disparate propagation speeds within the fiber [7]. This distinction in propagation speeds subsequently engenders a differential in delay for

the same transmission distance. The LP01 light engendered by the loss of LP11 crosstalk light ($I_{11\_C1}$) inherits the same delay difference with the signal light, thus it is also characterized as crosstalk light ($I_{01\_C}$), with the potential to impart detrimental effects on the system [8]. Figure 2-9 exclusively portrays a scenario featuring two connectors. However, should the optical path encompass more connectors, additional crosstalk light components would be generated.

In order to furnish a quantitative estimation of mode coupling and the corresponding intensity variation within this system, we made several plausible assumptions regarding the system, and subsequently derived expressions for each light component (signal light, LP11 crosstalk, and LP01 crosstalk) throughout transmission. Additionally, we performed quantitative calculations, employing reasonable system parameters for reference. The derivation process is depicted in the subsequent figure.

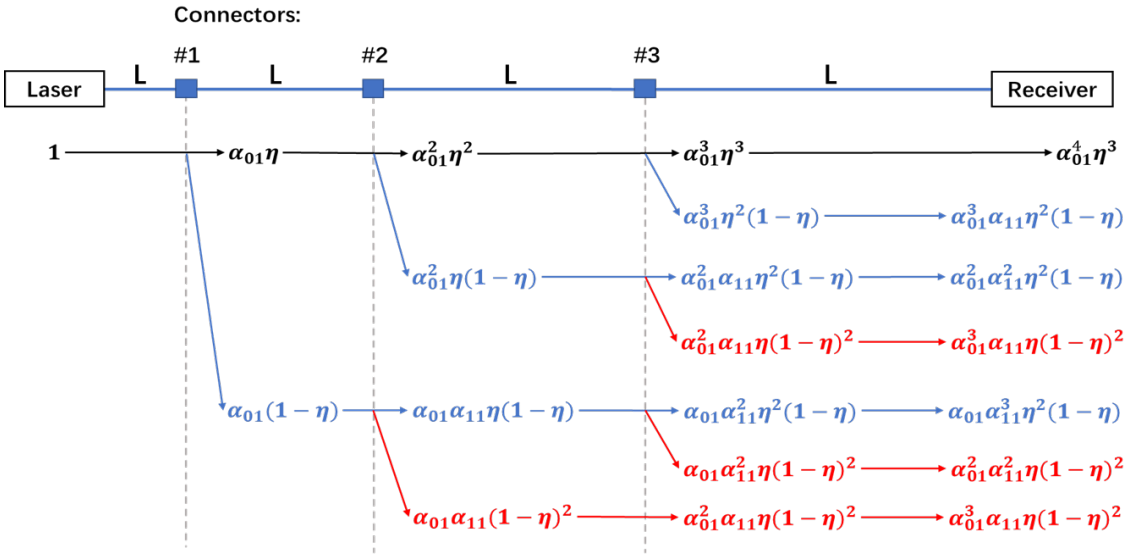


Fig. 2-10 Derivation process and expressions for each light component (LP01 signal, LP11 crosstalk and LP01 crosstalk) during transmission

Within this system, the following assumptions are posited:

Firstly, it is conjectured that the signal light emitted by the laser is solely the fundamental mode (LP01), and its power is normalized to unity.

Secondly, it is commonly observed that the lateral offset of the fiber connector falls below 1um [9-11]. At such a diminutive level of lateral offset, the coupling loss associated with both the LP01 and LP11 modes is relatively insignificant, thereby warranting the assumption that both modes bear an equivalent degree of coupling loss, denoted as $\eta$.

Thirdly, in many previous studies, it was assumed that 100% of the energy lost due to coupling between LP01 and LP11 modes was converted to the other mode. We simulated the coupling losses and the proportion of LP11 and LP01 modes excited for both LP01 and LP11 mode incidence, as shown in the following diagram. According to the simulation result, below an offset of 1μm, almost all the energy lost during LP01 incidence indeed converts to the LP11 mode. However, when LP11 is incident, only about 20% of its lost energy converts to LP01 mode light. The remaining 80% of the lost energy is emitted out of the fiber in the form of radiation modes. This means that in optical fibers, the crosstalk light is predominantly in the LP11 mode.

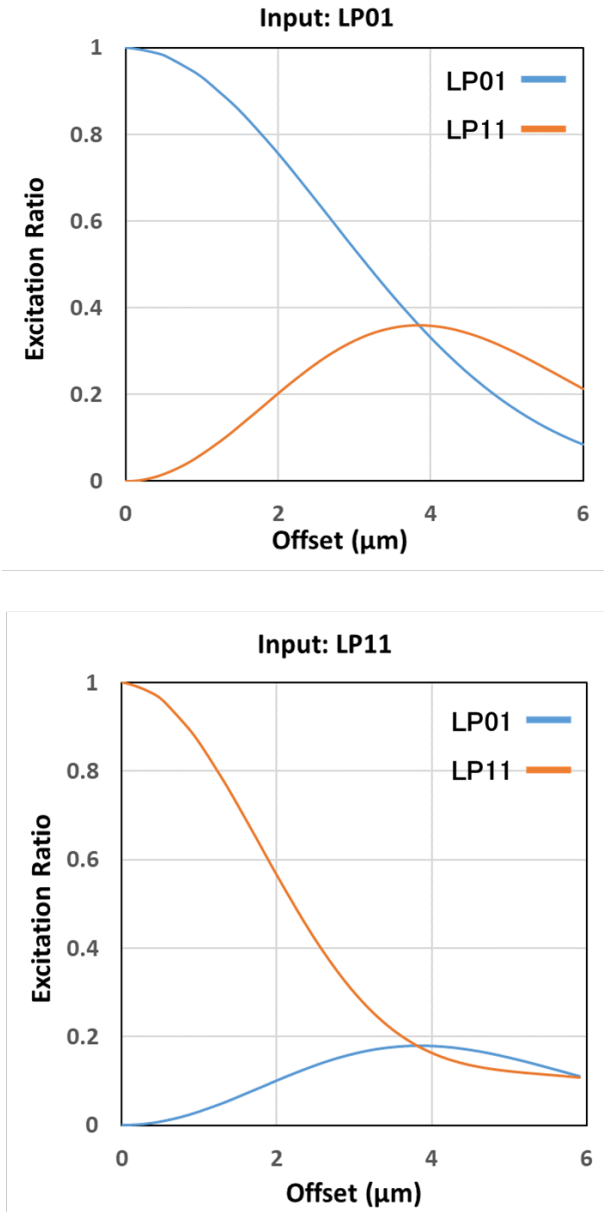


Fig. 2-11 Excitation efficiency of the 2 modes for both LP01 and LP11 incidence

Fourthly, it is presupposed that the fiber connectors are uniformly distributed along the optical path, with the length of each segment denoted as $L$. Additionally, the transmission loss has been factored into our calculations. The transmission losses experienced by the LP01 mode and the LP11 mode are denoted as $A_{01}$ and $A_{11}$, respectively, where the units are expressed in dB/km. Accordingly, after propagation over a length $L$, the associated

attenuation for the LP01 and LP11 modes is quantified as$A_{01}L$ and $A_{11}L$ respectively. For simplicity in calculations, we convert these attenuation measurements from dB to ratio format, represented by $\alpha_{01}$ and $\alpha_{11}$. This provides a more convenient form for subsequent analysis and calculation in the propagation system.

Furthermore, we have also considered the reflection of fiber connectors. Generally, the reflected light is typically less than -50dB, so it can be considered negligible.

In Fig.2-10, we employ different colors to distinguish between various light components for the sake of clarity. The signal light (LP01) is written in black, LP11 crosstalk in blue, and LP01 crosstalk in red. We will now proceed with a step-by-step analysis of the changes in light energy within this system.

Based on the stipulated assumptions, when the LP01 mode signal light first reaches the fiber connector #1, it undergoes a decrease in power to $\alpha_{01}$ as a result of attenuation. As it traverses through the first connector, it experiences coupling loss, which further decreases its optical power to $\alpha_{01}\eta$. Simultaneously, the energy lost is transformed into crosstalk light in the LP11 mode, which proceeds to propagate within the fiber with a magnitude of $\alpha_{01}(1-\eta)$.

Following this, both the LP01 mode signal light and the LP11 mode crosstalk light traverse a distance $L$ to arrive at the second connector (#2). As they have different transmission losses, by the time they reach the second connector, the power of the LP01 mode signal light has been reduced to $\alpha_{01}^2\eta$, while the LP11 mode crosstalk light is reduced to $\alpha_{01}\alpha_{11}(1-\eta)$. Both the LP01 signal and LP11 crosstalk components undergo coupling loss $\eta$ at the second connector. This coupling loss induces the generation of a second LP11 crosstalk light from the LP01 mode signal light and the creation of LP01 crosstalk light from the first LP11 crosstalk light. Consequently, at this juncture, there are

a total of four distinct light components present in the system: the LP01 mode signal light, two separate LP11 crosstalk lights, and one LP01 crosstalk light. Their expressions are denoted in Fig.2-10.

In the progression of our analysis, when these light components reach the third connector, they once again induce the generation of new LP01 and LP11 crosstalk lights. The corresponding expressions for these are indicated in Fig.2-10. However, it is crucial to note that while the coupling loss $\eta$ of the LP01 crosstalk light is calculated as it passes through the connector, we have disregarded the LP11 light generated by the coupling loss of this LP01 crosstalk light. The rationale behind this omission lies in the fact that our assumed value of $\eta$ is quite high, exceeding 90%. The LP11 crosstalk generated by LP01 crosstalk and signal has coefficient of $(1-\eta)^3$ and $(1-\eta)$, respectively. Therefore, there is a difference of over 100 times between the two. If the system has more than 8 connectors, the LP11 crosstalk generated by LP01 crosstalk becomes significant for calculation. However, for transmission distances within 2 km in large-scale data centers, there won't be as many connectors on a single optical path. Therefore, neglecting the LP11 crosstalk will not have any impact on the calculation.

Finally, after these light components have propagated an additional distance $L$, they reach the optical receiver, marking the completion of the transmission process.

When the number of fiber connectors within the system is increased to a total of $N$, it becomes possible to derive general formulae that depict the overall optical intensity of the various components of light within the system. These include the LP01 mode signal light, the LP11 mode crosstalk light, and the LP01 mode crosstalk light. The derivations of these formulae are given as Equations 2-7, 2-8, and 2-9 respectively. These equations provide a comprehensive understanding of how the optical intensity of different light

components varies as a function of the number of fiber connectors in the system.

$$I_{signal} = \alpha_{01}^{N+1}\eta^{N}I_{in} \quad (2-7)$$

$$I_{LP11} = (\alpha_{01}^{N}\alpha_{11} + \alpha_{01}^{N-1}\alpha_{11}^{2} + \cdots + \alpha_{01}\alpha_{11}^{N})\eta^{N-1}(1-\eta)I_{in} \quad (2-8)$$

$$I_{LP01} = 0.2 \cdot [(N-1)\alpha_{01}^{N}\alpha_{11} + (N-2)\alpha_{01}^{N-1}\alpha_{11}^{2} + \cdots + \alpha_{01}^{2}\alpha_{11}^{N-1}] \cdot \eta^{N-2}(1-\eta)^{2}I_{in} \quad (2-9)$$

In the aforementioned general formulas, $I_{in}$ symbolizes the light intensity of the incident signal light. After progressing through $N$ fiber connectors, a total of $N$ instances of LP11 crosstalk light and $N(N-1)/2$ instances of LP01 crosstalk light will be present within the system. These bear different time delays in relation to the signal light. To provide clarity, let's define a situation where the LP01 mode and the LP11 mode concurrently depart from the Nth connector and traverse through a fiber of length $L$ to the N+1th connector. In this scenario, a time delay $\tau$ is observed between the arrival times of the LP01 and LP11 modes. The illustration of this concept is depicted in the ensuing figure.

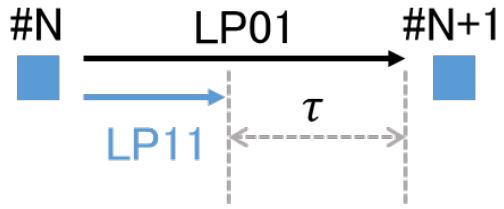


Fig.2-12 Time delay between LP01 and LP11 after propagating along same distance

In our model, given that the connectors are uniformly distributed along the optical path, the time delay between each crosstalk component and the signal light is an integer multiple of $\tau$. Upon derivation, this multiple is found to equate to the power of the $\alpha_{11}$ coefficient within each crosstalk component. This observation stems from the fact that only the transmission of the LP11 mode results in a change in the time delay relative to the signal light. The earlier the LP11 crosstalk is generated, the longer its path of travel

along the optical fiber, and hence, the greater its time delay relative to the signal light. Conversely, the LP01 crosstalk travels at the same speed as the signal light. Thus, regardless of the point of origin of the LP01 crosstalk, its subsequent propagation does not increase the time delay relative to the signal light.

Both LP11 and LP01 crosstalks can have detrimental effects on the system, inducing issues such as modal noise and dispersion, leading to a reduction in the system's data transmission capacity. To mitigate these effects, a simple yet effective solution is the introduction of a mode filter at the terminus of the system to eliminate the LP11 mode. To some extent, this approach can alleviate the damage imparted by the system. The effectiveness of the mode filter will be illustrated in forthcoming sections through quantitative calculations.

### *2.2.2 Calculation of modal noise w/ and w/o mode filter*

The deleterious effects of crosstalk light on the system are principally manifested in the noise it introduces. A time delay exists between the LP01 crosstalk and the signal light (LP01), as well as amongst LP11 crosstalk components. This leads to interference, engendering fluctuations in light intensity. As previously mentioned in Chapter 1, this form of intermodal interference transduces the phase noise of the laser into intensity noise, a phenomenon referred to as modal noise. This is illustrated in the ensuing figure.

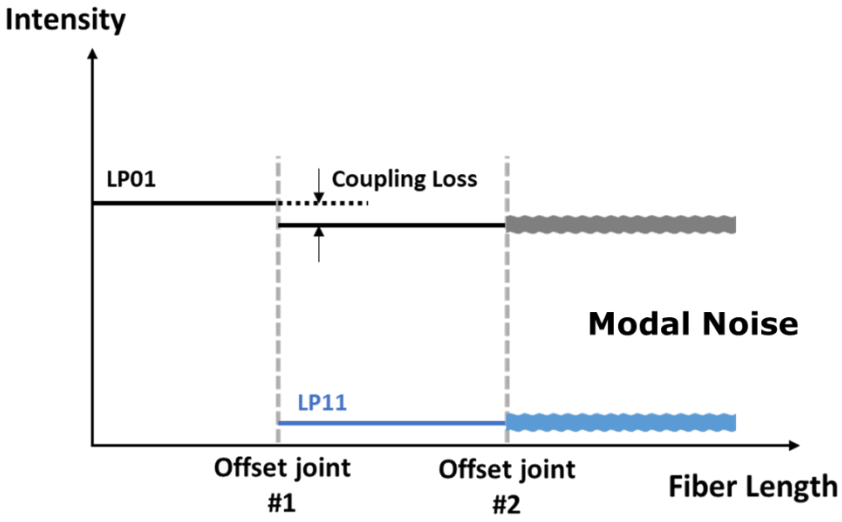


Fig. 2-13 Modal noise induced by interference

The expression for the optical field is defined as follows:

$$E_i = A_i \cos[\omega_0 t + \varphi_i(t)] \qquad (2-10)$$

In this expression, $A_i$ represents amplitude, and $\omega_0$ symbolizes the optical frequency. $\varphi_i(t)$ signifies its phase; given that the laser has phase noise, the phase is a function of time. Its light intensity satisfies $I_i = |A_i|^2$. When two lights of the same frequency, with light intensities $I_1$ and $I_2$ respectively, interfere, the light intensity after interference can be expressed as:

$$I = |E_1 E_2|^2 = I_1 + I_2 + 2\sqrt{I_1 I_2} \cos[\omega_0 \tau + \varphi(t,\tau)] \qquad (2-11)$$

The third term in the equation is the interference term. As one can see, the phase difference in interference is affected by the phase noise of the laser [12], including a random factor $\varphi(t,\tau)$ related to the time delay. This factor is assumed to have a Gaussian probability distribution function.

$$P(\varphi) = \frac{1}{\sqrt{2\pi}\sigma_\varphi(\tau)} e^{\frac{-\varphi^2}{2\sigma_\varphi^2(\tau)}} \qquad (2-12)$$

Indeed, as the phase difference in interference, affected by phase noise, is a random

variable, it leads to random changes in interference intensity, forming intensity noise. The power spectrum of the noise, $P(f)$, can be obtained by performing a Fourier transform on its autocorrelation function. Here, the autocorrelation function, $R(t,\tau)$, is defined as follows [13]:

$$R(t,\tau) = 2I_1 I_2 \begin{cases} e^{-\sigma_\varphi^2|t|}\left[1+\cos(2\omega_0\tau)\, e^{-2\sigma_\varphi^2(\tau-|t|)}\right] & |t|<\tau \\ e^{-\sigma_\varphi^2(\tau)}[1+\cos(2\omega_0\tau)] & |t|>\tau \end{cases} \qquad (2-13)$$

Where $\sigma_\varphi^2(\tau)$ is the variance of the phase noise, satisfying $\sigma_\varphi^2(\tau) = 2\pi\Delta f \cdot \tau$. Here, $\Delta f$ is the linewidth of the laser.

Next, by performing a Fourier transform on $R(t,\tau)$ and removing the DC component, the power spectrum can be obtained as follows:

$$P(f) = \frac{4I_1 I_2}{\pi}\left[\frac{\Delta f}{f^2+(\Delta f)^2}\right] \cdot \left\{ \begin{matrix} \sin^2(\omega_0\tau)\cdot[1+e^{-4\pi\Delta f\tau}-2e^{-2\pi\Delta f\tau}\cos(2\pi f\tau)]+ \\ \cos^2(\omega_0\tau)\cdot\left[1-e^{-4\pi\Delta f\tau}-2e^{-2\pi\Delta f\tau}\cdot\frac{\Delta f}{f}\sin(2\pi f\tau)\right] \end{matrix} \right\} \qquad (2-14)$$

The noise $\sigma_{1,2}^2$ can be obtained by integrating the power spectrum over the receiver bandwidth. For high-speed transmission systems, if the bandwidth is much larger than the laser linewidth $\Delta f$, a larger integral result will be achieved. In our system, the linewidth of the 1060nm single-mode VCSEL laser used is below 30MHz, while the system bandwidth exceeds 20GHz. Under these conditions, the integral of the power spectrum $P(f)$ can be approximated as follows:

$$\sigma_{1,2}^2 \approx \int_0^\infty P(f)df = 2I_1 I_2(1-e^{-4\pi\Delta f\tau}) \qquad \omega_0\tau = \left(n+\frac{1}{2}\right)\pi \qquad (2-15a)$$

$$\sigma_{1,2}^2 \approx \int_0^\infty P(f)df = 2I_1 I_2(1+e^{-4\pi\Delta f\tau}-2e^{-2\pi\Delta f\tau}) \qquad \omega_0\tau = n\pi \qquad (2-15b)$$

Eq.2-15a and Eq.2-15b respectively provide the upper and lower noise boundaries in circumstances where interference occurs in quadrature and in-phase conditions. In reality, the extent of interference also depends on the polarization directions of the two light

waves. However, for the purposes of this study, we assume that the polarization directions of the interfering lights are consistent. This simplification allows us to calculate the maximum noise to estimate the worst-case scenario for the system [15].

As depicted in Fig.2-13, our system experiences interference and subsequent noise from both LP01 and LP11 mode lights. Therefore, by substituting Eqs. 2-7 through 2-9 into Eq. 2-15a, we can calculate the maximum noise induced by crosstalk. For the LP01 mode, $I_1$=$I_{signal}$ represents the signal light, and $I_2 = I_{LP01\_i}$ represents any LP01 crosstalk light. For the LP11 mode, $I_1$ and $I_2$ respectively represent any two different LP11 crosstalks, denoted as $I_{LP11\_m}$ and $I_{LP11\_n}$. Simultaneously, the time delay differences $\tau_i$ (LP01 mode) and $|\tau_m - \tau_n|$ (LP11 mode) will replace the original variable $\tau$ in Equation 2-15a. It's important to note that LP01 crosstalk light can also interfere with each other. However, given its relatively small magnitude, it can be ignored. The equations representing the noise generated by the LP01 and LP11 modes are as follows:

$$\begin{aligned}\sigma_{01}^2 &= 2I_{signal}I_{LP01\_i}\cdot(1-e^{-4\pi\Delta f\tau_i}) \\ &= 2I_{in}^2\sum_{i=1}^{N-1}(N-i)\alpha_{01}^{2N+2-i}\alpha_{11}^{i}\cdot\eta^{2N-2}(1-\eta)^2 \\ &\qquad\cdot(1-e^{-4\pi\Delta f\tau_i}) \qquad (2-16)\end{aligned}$$

$$\begin{aligned}\sigma_{11}^2 &= 2I_{LP11\_m}I_{LP11\_n}\cdot\left(1-e^{-4\pi\Delta f|\tau_m-\tau_n|}\right) \\ &= 2I_{in}^2\sum_{m\neq n}^{N}\alpha_{01}^{2N+2-(m+n)}\alpha_{11}^{m+n}\cdot\eta^{2N-2}(1-\eta)^2 \\ &\qquad\cdot\left(1-e^{-4\pi\Delta f|\tau_m-\tau_n|}\right) \qquad (2-17)\end{aligned}$$

Here we will assume specific parameters within the system to compute the extent of modal noise. Calculations will be performed for scenarios both with and without the use of a mode filter. The parameters assumed for these computations are listed in the following table:

Table 2-3 Parameters used in modal noise calculation

| | | |
|---|---|---|
| Segment length | L (km) | 0.4 |
| Connector number | N | 4 |
| LP01 attenuation | $\alpha_{01}$ (dB/km) | 0.8 |
| LP11 attenuation | $\alpha_{11}$ (dB/km) | 4 |
| Time delay between LP01/LP11 | τ (ps/m) | 0.4 |
| Coupling efficiency of connector | η | 0.93 |

In current large-scale data centers, the transmission distance of optical cables can extend up to 2 km. While structured cabling systems utilized improve flexibility, they simultaneously introduce more connection points into the optical path. As discussed in Chapter 1, we set the transmission distance in our model to 2 km, incorporating 4 optical fiber connectors. The attenuation of the LP01 and LP11 modes, along with the time delay difference between them, are theoretical values acquired from reference papers and relevant materials [15-17]. The coupling efficiency ($\eta$) of the fiber connector is based on our simulation results, assuming a lateral offset of 1μm, which results in a coupling efficiency of 93%. A detailed explanation of the lateral-offset splicing simulation will be provided in the subsequent chapter.

In the model of the mode coupling process discussed in the previous section, we assumed that the optical fiber connectors are uniformly distributed along the optical path. $N$ connectors will divide the fiber into $N + 1$ segments, each with a length of $L$. Therefore, according to the data in the table above, L=0.4km. Given that the linewidth of the laser varies inversely with its output power, these parameters can be substituted into Eq.2-16 and Eq.2-17 to derive the noise-linewidth curve of the system. The results are depicted in the following figure:

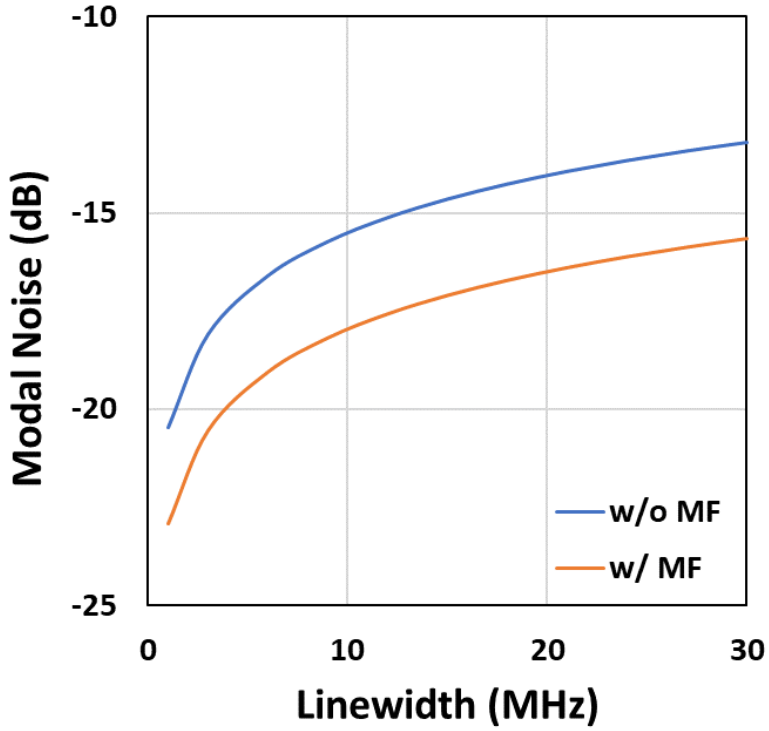


Fig. 2-14 Modal noise vs laser linewidth w/ and w/o mode filter

Under linewidths ranging from 1 to 30 MHz, we calculated the modal noise both with and without the application of a mode filter. It can be observed that the deployment of a mode filter can mitigate modal noise by approximately 2.5dB through the elimination of the LP11 mode. This reduction can significantly enhance the bit error rate (BER) of the system, particularly in scenarios where the thermal noise within the system is low and modal noise serves as the primary contributor.

### *2.2.3 Analysis of power penalty induced by modal noise*

In order to calculate the power penalty incurred due to modal noise within the system, it is first necessary to compute its impact on the system's BER. Let's assume that the modulation format is Non-Return to Zero-On Off Keying (NRZ-OOK). The levels of the "mark" and "space" signals transmitted are represented by $i_1$ and $i_0$, respectively. The

Extinction Ratio ($r_e$) is defined as $i_1 = r_e i_0$. We will assume a back-to-back connection between the transmitter and receiver, with no system loss. Further, let's assume that only thermal noise $\sigma_0$ exists within the system. Both the "mark" and "space" signals share the same thermal noise. Consequently, the decision level ($i_D$) of the system is the average value of the "mark" and "space" signals, $i_D = (i_1 + i_0)/2$. The BER can be depicted as illustrated in the forthcoming figure:

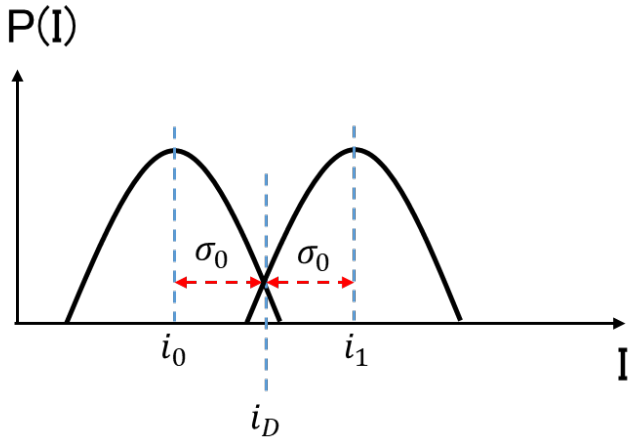


Fig. 2-15 The bit error rate of ideal transmission system

The system's BER can be expressed as:

$$BER = \frac{1}{4} erfc\left(\frac{1}{\sqrt{2}} \frac{i_1 - i_D}{\sigma_0}\right) + \frac{1}{4} erfc\left(\frac{1}{\sqrt{2}} \frac{i_D - i_0}{\sigma_0}\right) \quad (2-18)$$

Since $i_1 - i_D = i_D - i_0 = (i_1 - i_0)/2$, Eq. 2-18 can be simplified to:

$$BER = \frac{1}{2} erfc\left(\frac{1}{\sqrt{2}} \frac{i_1 - i_0}{2\sigma_0}\right) \quad (2-19)$$

Expressing $i_1$ and $i_0$ in terms of $i_D$ and $r_e$. Then the $Q$ value could be expressed as:

$$Q = \frac{i_1 - i_0}{2\sigma_0} = \frac{(r_e - 1) i_D}{(r_e + 1)\sigma_0} \quad (2-20)$$

Therefore, the expression for thermal noise can be obtained as:

$$\sigma_0 = \frac{(r_e - 1) i_D}{(r_e + 1) Q} \quad (2-21)$$

When considering the system's target BER, the required Q value can be determined. For

instance, when targeting a BER of $1 \times 10^{-12}$, the corresponding $Q$ value would be approximately 7. Given this Q value and taking into account the extinction ratio ($r_e$), we can then compute the level of thermal noise present.

In our data transmission system, the presence of coupling loss and modal noise has a detrimental impact. The signal received will be diminished due to losses, while the noise level will be augmented. This dynamic can be visualized in the following diagram:

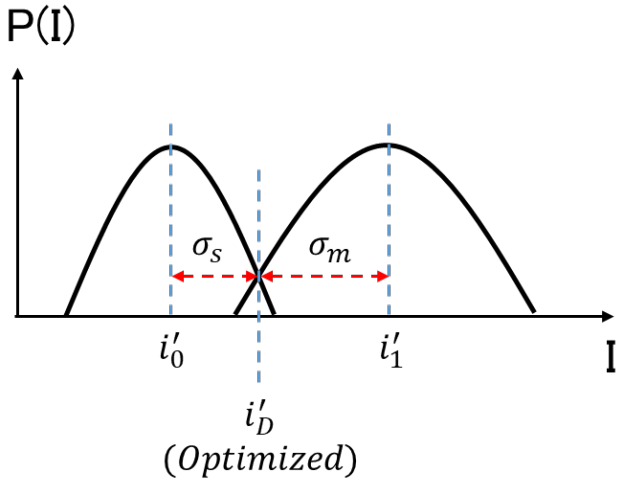


Fig. 2-16 Bit error rate after transmission along the fiber with imperfect connectors

In this diagram, $i_1'$ and $i_0'$ represent the optical intensities of the "mark" and "space" signals, respectively, after incurring various transmission losses. Since the modal noise is a function of the input power, the noise associated with the "mark" and "space" signals no longer remains identical, hence denoted separately as $\sigma_m$ and $\sigma_s$.

Under these circumstances, the new optimal decision level ($i_D'$) no longer equals the average of $i_1'$ and $i_0'$, as previously. Instead, it is co-determined by the intensities of the "mark" and "space" signals ($i_1'$ and $i_0'$) and their respective noise levels ($\sigma_m$ and $\sigma_s$). The equation that expresses this relation is:

$$i_D' = i_0' + \frac{\sigma_s}{\sigma_s + \sigma_m}(i_1' - i_0')$$

$$= \frac{i_1'\sigma_s + i_0'\sigma_m}{\sigma_s + \sigma_m} \qquad (2-22)$$

Based on the optimal decision level ($i_D'$), the Q-value expressions of "mark" and "space" level have following relation:

$$\frac{i_1' - i_D'}{\sigma_m} = \frac{i_D' - i_0'}{\sigma_s} = \frac{i_1' - i_0'}{\sigma_s + \sigma_m} \qquad (2-23)$$

Therefore, the BER in this case will be expressed as:

$$BER = \frac{1}{4} erfc\left(\frac{1}{\sqrt{2}} \frac{i_1' - i_D'}{\sigma_m}\right) + \frac{1}{4} erfc\left(\frac{1}{\sqrt{2}} \frac{i_D' - i_0'}{\sigma_s}\right)$$
$$= \frac{1}{2} erfc\left(\frac{1}{\sqrt{2}} \frac{i_1' - i_0'}{\sigma_s + \sigma_m}\right) \qquad (2-24)$$

In Eq.2-24, the $i_1'$ and $i_0'$ could be express by Eq.2-7 with using $i_1$ and $i_0$ as $I_{in}$, respectively. And since $i_1$ and $i_0$ could be expressed by $r_e$ and $i_D$. Therefore, the expressions of $i_1'$ and $i_0'$ could be written as:

$$i_1' = \alpha_{01}^{N+1} \eta^N i_1 = \alpha_{01}^{N+1} \eta^N \frac{2r_e}{r_e + 1} i_D \qquad (2-25)$$

$$i_0' = \alpha_{01}^{N+1} \eta^N i_0 = \alpha_{01}^{N+1} \eta^N \frac{2}{r_e + 1} i_D \qquad (2-26)$$

As previously discussed, the LP01 and LP11 modes introduce modal noises $\sigma_{01}^2$ and $\sigma_{11}^2$ into the system, respectively. The LP01 modal noise ($\sigma_{01}^2$), given its relation to the output signal, is differentiated into $\sigma_{01\_s}^2$ and $\sigma_{01\_m}^2$ for "space" and "mark" signals, correspondingly. Their expressions can be deduced from Eq.2-16 and Eq.2-17. In these equations, $I_{signal}$ should be substituted by $i_0'$ and $i_1'$ for "space" and "mark" signals, respectively.

When examining the crosstalk expressions $I_{LP01}$ (Eq.2-9) and $I_{LP11}$ (Eq.2-8), both contain a common factor, $I_{in}$. In this context, $I_{in}$ should be replaced with the average level $i_D$ rather than $i_1$ and $i_0$ differentiated based on "mark" and "space" levels. This approach is justified because, during data transmission, the "mark" and "space" levels are assumed

to be random with each accounting for 50% of the data. Further, a time delay exists between the crosstalk and the signal, implying that the crosstalk interfering with a given signal does not originate from the signal itself, but rather from multiple preceding signals. Consequently, $i_D$ is employed to calculate the average crosstalk, and the expressions for the LP01 and LP11 modal noise are as follows:

$$\sigma_{01\_\mathrm{s}}^2 = 2i_0' i_D \sum_{i=1}^{N-1} (N-i)\alpha_{01}^{N+1-i}\alpha_{11}^{i} \cdot \eta^{N-2}(1-\eta)^2 \cdot (1-e^{-4\pi\Delta f \tau_i}) \quad (2-27)$$

$$\sigma_{01\_\mathrm{m}}^2 = 2i_1' i_D \sum_{i=1}^{N-1} (N-i)\alpha_{01}^{N+1-i}\alpha_{11}^{i} \cdot \eta^{N-2}(1-\eta)^2 \cdot (1-e^{-4\pi\Delta f \tau_i}) \quad (2-28)$$

$$\sigma_{11}^2 = 2i_D^2 \sum_{m\neq n}^{N} \alpha_{01}^{2N+2-(m+n)}\alpha_{11}^{m+n} \cdot \eta^{2N-2}(1-\eta)^2 \cdot \left(1-e^{-4\pi\Delta f|\tau_m-\tau_n|}\right) \quad (2-29)$$

Therefore, the total noise $\sigma_m$ (mark) and $\sigma_s$ (space) in receiver could be written as:

$$\sigma_s = \sqrt{\sigma_0^2 + \sigma_{01\_\mathrm{s}}^2 + \sigma_{11}^2} \quad (2-30)$$

$$\sigma_m = \sqrt{\sigma_0^2 + \sigma_{01\_\mathrm{m}}^2 + \sigma_{11}^2} \quad (2-31)$$

Incorporating Eq.2-25, Eq.2-26, Eq.2-30, and Eq.2-31 into Eq.2-24, we can determine the system's bit error rate (BER), considering both the loss and modal noise. One straightforward approach to reducing the BER is by increasing the input power, with the ratio of increase termed the power penalty ($\delta$). Consequently, the expression for BER, upon introducing the power penalty, can be modified as follows:

$$BER = \frac{1}{2} erfc\left[\frac{1}{\sqrt{2}} \frac{\delta(i_1' - i_0')}{\sqrt{\sigma_0^2 + \delta^2\sigma_{11}^2 + \delta^2\sigma_{01\_m}^2} + \sqrt{\sigma_0^2 + \delta^2\sigma_{11}^2 + \delta^2\sigma_{01\_s}^2}}\right] \quad (2-32)$$

Indeed, since the modal noise ($\sigma_{01\_s}^2$, $\sigma_{01\_m}^2$ and $\sigma_{11}^2$) is correlated with the transmission power, they will also increase with the introduction of the power penalty. Therefore, when the magnitude of the modal noise equates to, or is less than, the level of thermal noise ($\sigma_0$), introducing a power penalty can effectively reduce the BER. However, when the modal noise escalates to a point where it renders the thermal noise almost negligible, the system reaches its lower BER limit. At this point, enhancing the transmission power further no longer aids in reducing the BER. However, the use of a mode filter to eliminate the LP11 mode can remove the $\sigma_{11}^2$ term from the total noise, effectively reducing the BER.

In order to compute the power penalty, in addition to the parameters that have already been defined in Table 2-3, we also need to presume the target BER, extinction ratio ($r_e$), and thermal noise. The values for each parameter are displayed in the following table:

Table 2-4 Parameters for power penalty calculation

| | | |
|---|---|---|
| Q value | w/ FEC | 2.678 |
| | w/o FEC | 7 |
| Extinction ratio | $r_e$ (dB) | 4 |
| Thermal noise (25Gb/s) | $\sigma_0$ (dB) | -20.9 |

We've computed scenarios both incorporating and excluding Forward Error Correction (FEC). With the application of FEC, the system tolerates a maximal BER of 3.7e-3, correlating to the Q value of 2.678. In the absence of FEC, the system's acceptable BER peaks at 1e-12, translating to the Q value of 7.

The Eq.5-3 was employed as a foundation to deduce the thermal noise. Herein, '$k$' stands for Boltzmann's constant. '$T$' symbolizes the temperature, which under ambient conditions, is 295K. It's predicated on an assumed resistance value, $R_f$, of 500Ω. Under these

stipulated parameters, it becomes evident that the thermal noise escalates in conjunction with an increase in the system's bandwidth.

$$\sigma_0 = \sqrt{\frac{4kTB}{R_f}} \qquad (5-3)$$

Additionally, we operate under the assumption that the average power of the input signal is 1mW, and the system responsivity stands at 0.5A/W. Without factoring in attenuation, the photo-current is calculated at 0.5mA. Based on these premises, we postulate transmission rates at 50Gb/s, which correspond to minimum bandwidths of 25GHz. From our computations, the thermal noise amounts to -20.9dB.

In the computational process, the initial step entailed calculating the minimum input power required to meet the system's maximal bit error rate criteria. Subsequently, by juxtaposing the minimum power values under varied conditions, we discerned the power penalty. The calculated penalties w/ and w/o using mode filter are depicted in the subsequent figure.

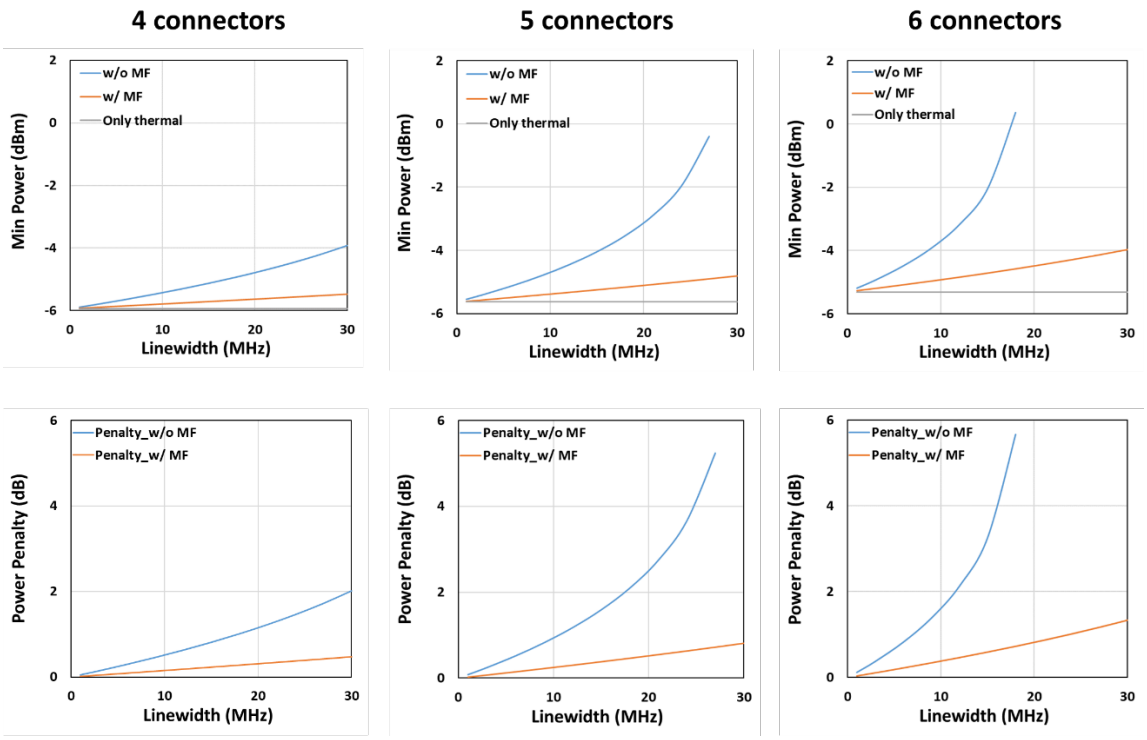


Fig. 2-17 Minimum power and power penalty w/ and w/o use mode filter of NRZ modulation for 2km transmission

Figure 2-17 presents the computed results for a 2km transmission based on NRZ modulation. The three graphs positioned above pertain to the minimum power requirement. Among these, the grey line labeled "Only thermal" represents the minimal power required by the system when only considering thermal noise and transmission losses. Consequently, this value is independent of the laser linewidth. By subtracting this baseline value from the minimal power computed after introducing modal noise, the resulting difference represents the power penalty attributable to modal noise only.

The calculations encompass both scenarios: with and without the use of a mode filter, under varying quantities of optical fiber connectors. It is observed that the power penalty required by the system significantly escalates with an increase in the number of connectors. In scenarios where mode filter is not employed, and the linewidth of the light

source is comparatively large, the system's BER floor exceeds the maximum permissible BER for transmission. This suggests that the system's transmission capability falls short of meeting the requirements. However, the application of a mode filter substantially mitigates noise, thereby reducing both the system BER and the power penalty.

Employing the same computational methodology, we also calculated the power penalty associated with PAM4 modulation. Given the heightened sensitivity of PAM4 modulation to noise, the calculations distinctly accounted for scenarios both with and without Forward Error Correction (FEC). In these computations, the impact of varying distances, in addition to different numbers of connectors, was also considered. The results of these calculations are illustrated in Figures 2-18 and 2-19.

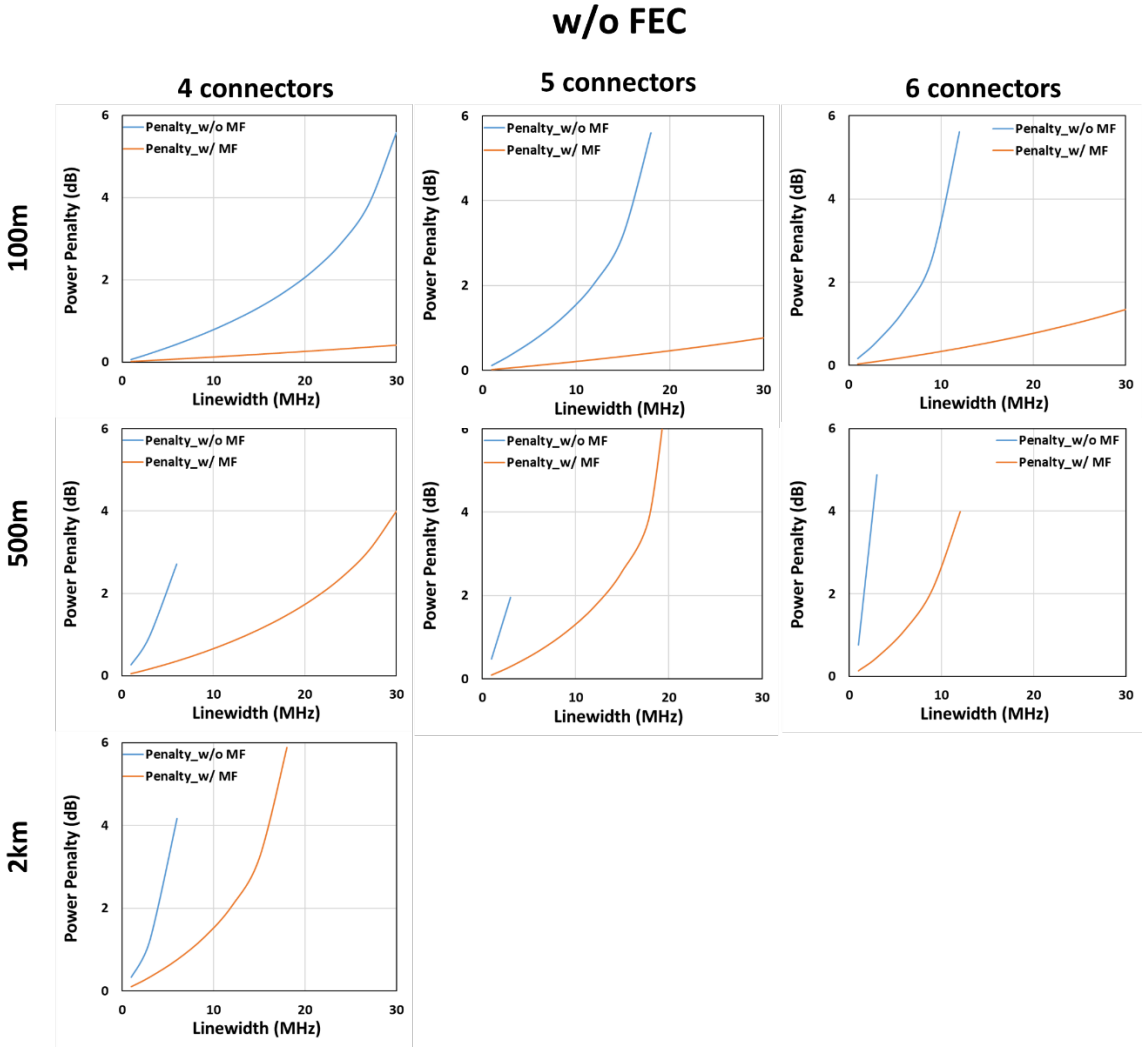


Fig. 2-18 The power penalty of PAM4 modulation w/o FEC

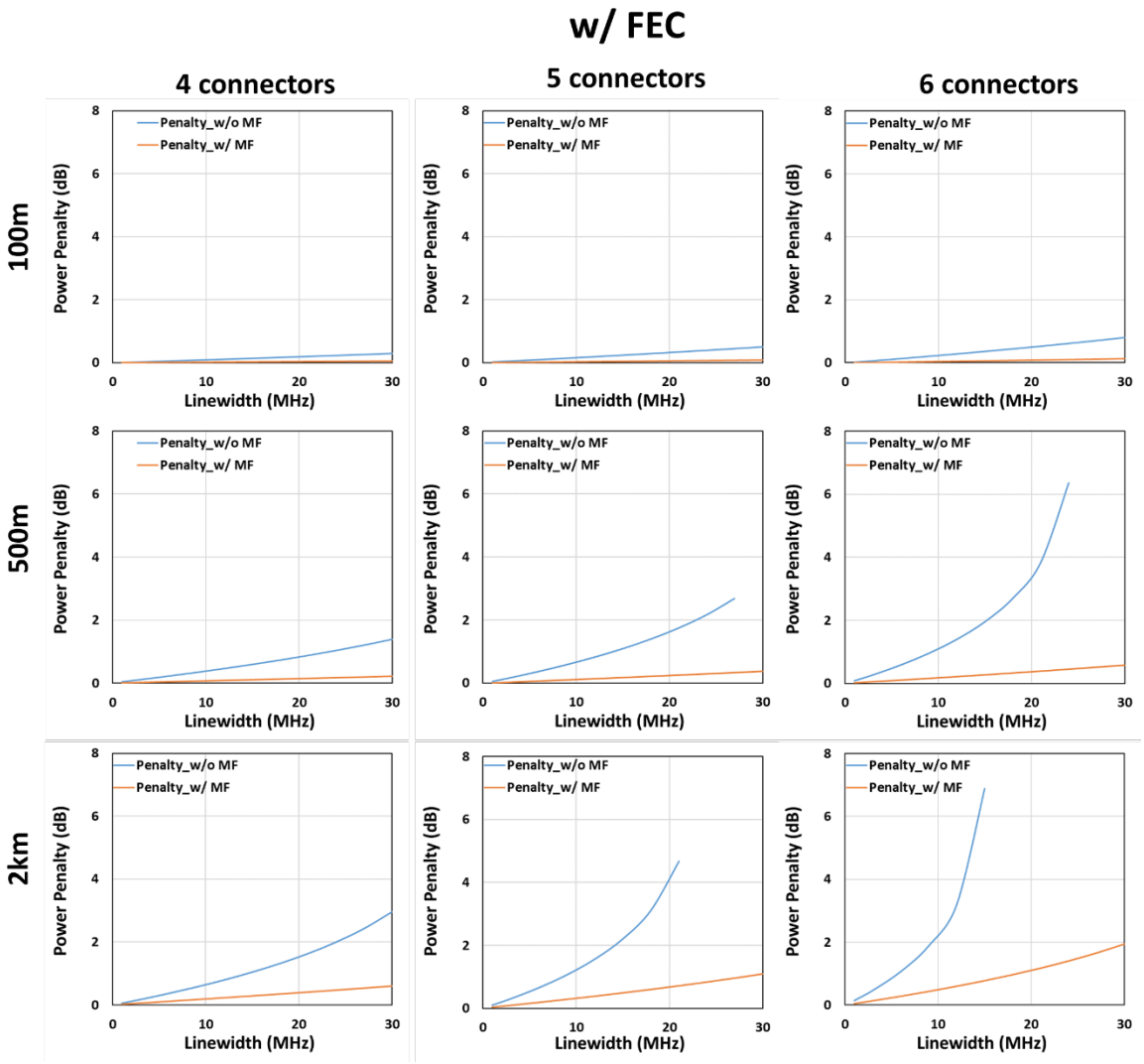


Fig. 2-19 The power penalty of PAM4 modulation w/ FEC

It should be noted that in Fig.2-18, only the results for a transmission distance of 2km with four connectors are presented. This limitation arises because when the number of connectors exceeds four, the noise becomes so substantial that it precludes the derivation of valid computational results.

A horizontal comparison across the charts in the figure reveals the impact of the number of fiber connectors on the results at the same transmission distance. Conversely, a vertical comparison shows the influence of transmission distance on the results for the same

number of connectors. It is evident that both an increase in the number of connectors and a longer transmission distance significantly amplify modal noise, leading to a steep rise in system power penalty until the Bit Error Rate (BER) exceeds its upper limit. Even in scenarios with Forward Error Correction (FEC), where the system's tolerable BER upper limit is substantially higher, the occurrence of BER exceeding this limit is still possible when the number of connectors surpasses four, and the transmission distance exceeds 500m, particularly if the laser linewidth is broad. However, the use of mode filter, as demonstrated in Fig.2-19, effectively prevents BER from exceeding its limit in all cases, with the maximum power penalty being only about 2dB.

Furthermore, the utilization of FEC introduces additional latency to the system and exhibits a diminished capability to combat packet loss. Consequently, FEC is not suitable for applications such as VoIP and video conferencing. In such scenarios, the system will be much more sensitive to modal noise as the results exhibited in Fig.2-18. Under such circumstances, the deployment of mode filter becomes more imperative.

## Reference in Chapter 2


2-1 Yariv, A., "Optical electronics in modern communications," in Proc. Conf. Abbreviation, (1997).

2-2 R. Hui, "Introduction to fiber-optic communications," Academic Press, (2019).

2-3 Olshansky, R., "Mode coupling effects in graded-index optical fibers," Appl. Opt., (1975)

2-4 S. Mikroulis, O. Omomukuyo, M. P. Thakur, and J. E. Mitchell, "Investigation of a SMF-MMF link for a remote heterodyne 60-GHz OFDM RoF based gigabit wireless access topology," J. Lightwave Technol. 32(20), 3645–3653 (2014).

2-5 J. Vuong, P. Ramantanis, Y. Frignac, M. Salsi, P. Genevaux, D. F. Bendimerad, and G. Charlet, "Mode coupling at connectors in mode-division multiplexed transmission over few-mode fiber," Opt. Express 23(2), 1438–1455 (2015).

2-6 M. R. T. Tan, B. Wang, W. V. Sorin, S. Mathai, and P. Rosenberg, "50 Gb/s PAM4 modulated 1065 nm single-mode VCSELs using SMF-28 for mega-data centers," IEEE Photonics Technol. Lett. 29(13), 1128–1131 (2017).

2-7 K. Sulimany and Y. Bromberg, "All-fiber source and sorter for multimode correlated photons," npj Quantum Inf. 8(1), 4 (2022).

2-8 F. Sears, I. White, R. Kummer, and F. Stone, "Probability of modal noise in single-mode lightguide systems," J. Lightwave Technol. 4(6), 652–655 (1986).

2-9 Y. Ando, S. Iwano, K. Kanayama, and R. Nagase, "Statistical analysis on connection characteristics of optical fiber connectors," IEICE Trans. Electron. 77(12), 1970–1982 (1994).

2-10 Y. Ando, "Statistical analysis of insertion-loss improvement for optical connectors using the orientation method for fiber-core offset," IEEE Photonics Technol. Lett. 3(10), 939–941 (1991).

2-11 E. Sugita, R. Nagase, K. Kanayama, and T. Shintaku, "SC-type single-mode optical fiber connectors," J. Lightwave Technol. 7(11), 1689–1696 (1989).

2-12 R. Tkach and A. Chraplyvy, "Phase noise and linewidth in an InGaAsP DFB laser," J. Lightwave Technol. 4(11), 1711–1716 (1986).

2-13 J. L. Gimlett and N. K. Cheung, "Effects of phase-to-intensity noise conversion by multiple reflections on gigabit-per-second DFB laser transmission systems," J. Lightwave Technol. 7(6), 888–895 (1989).

2-14 H. Takahashi, K. Oda, and H. Toba, "Impact of crosstalk in an arrayed-

waveguide multiplexer on N/spl times/N optical interconnection," J. Lightwave Technol. 14(6), 1097–1105 (1996).

2-15 P. Mondal, R. Haldar, V. Mishra, and S. K. Varshney, "All-optical mode conversion and temperature sensing via transient grating in step-index fiber," IEEE Photonics Technol. Lett. 30(24), 2175–2178 (2018).

2-16 E. Simpanen, J. S. Gustavsson, A. Larsson, M. Karlsson, W. V. Sorin, S. Mathai, M. R. Tan, and S. R. Bickham, "1060 nm single-mode VCSEL and single-mode fiber links for long-reach optical interconnects," J. Lightwave Technol. 37(13), 2963–2969 (2019).

2-17 J. C. Goodwin and P. J. Vella, "Modal noise in short fiber sections," J. Lightwave Technol. 9(8), 954–958 (1991).

# Chapter3

# Design and characterization of fiber-based mode filter

In addressing the modal noise concern elaborated in the preceding chapter, the application of a mode filter facilitates the nullification of the LP11 mode and the concomitant noise ($\sigma_{11}^2$) it proliferates within the system, hence significantly diminishing the system bit error rate and power penalty. An extensive analysis of various mode filters was undertaken in the Chapter 1, demonstrating their consistently superior performance. Nonetheless, the realization of these mode filters invariably necessitates specialized apparatus or processes. Consequently, they introduce additional expenditures and potentially incur non-trivial insertion losses. To circumvent this predicament, we put forward a mode filtering strategy predicated on the bent fiber principle. The ensuing discourse in this chapter will provide an in-depth exposition on the design and performance metrics of this proposed solution.

## 3.1 Theoretical analysis and simulation of bending fiber

Upon the incidence angle of light satisfying the condition for total internal reflection, the light will not incur losses due to refraction at the core-cladding interface. However, in circumstances where the optical fiber undergoes bending, the reflection angle of the light is subsequently altered at the bend. If the incident angle falls below the critical angle requisite for total internal reflection, a fraction of the light will deviate and scatter outward, engendering bending loss. This concept is visually delineated in the following figure:

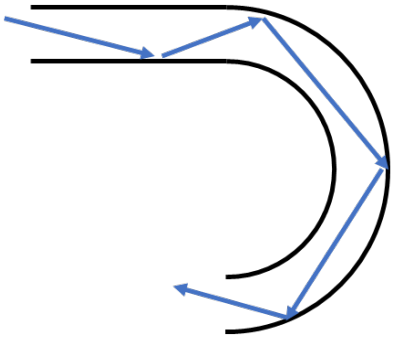

Fig. 3-1 Light transmission in bent fiber

Within an optical fiber, as opposed to the fundamental mode where energy is predominantly concentrated at the core's center, the energy of the higher-order modes tends to be positioned closer to the core's periphery [1]. When the optical fiber undergoes bending, the outermost energy is more prone to penetrate the cladding, thereby resulting in energy loss. Hence, given an identical bending radius, the bending loss experienced by higher-order modes markedly surpasses that of the fundamental mode. By judiciously selecting an appropriate bending radius and the number of windings, the higher-order modes can incur significant loss while the fundamental mode remains largely loss-free.

To explore the bending loss characteristics of 1060nm light in conventional single-mode fibers, we employ Fimmwave software for modeling and simulation purposes. The schematic representation of the bent fiber model is depicted in the ensuing figure:

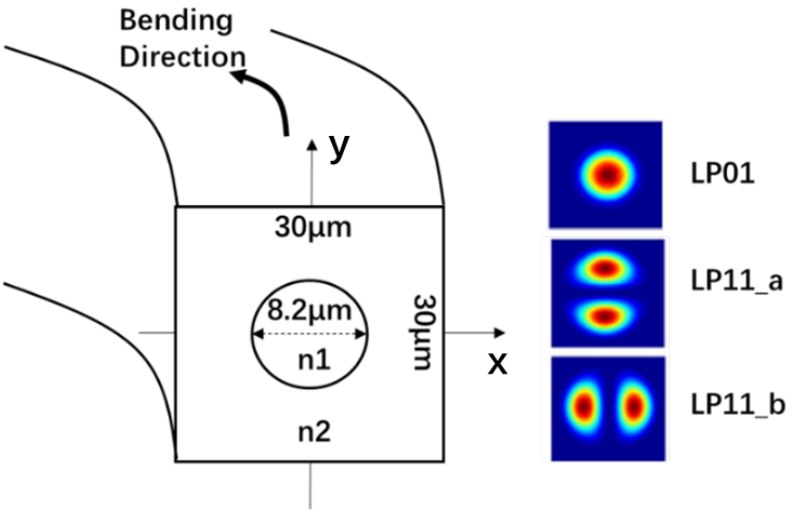


Fig. 3-2 Simulation model of bending fiber

In the construction of the model, we drew reference from the SMF28-ULTRA fiber, a product of Corning Inc [2]. The diameters of the core and cladding measure 8.2μm and 125μm respectively. As demonstrated in Fig.3-2, the morphology and size of the core within our model precisely mirror those of the SMF28-ULTRA. However, the cladding is conceptualized as a square, with each side measuring 30μm. This modification is premised on our experimental observations regarding the influence of the cladding's shape and size on the simulation outcomes. The region beyond the cladding is absorption boundary. Our findings indicate that, provided the cladding size exceeds 20μm, the effect on the results is minimal, irrespective of whether the cladding is circular or square. Thus, in the interest of enhancing computational efficiency, we diverged from the actual shape and size of the fiber cladding. The parameters incorporated within the model are elaborated in the table below:

Table 3-1 Parameters of bending loss simulation model

| | |
|---|---|
| Core index (n1) | 1.47 |
| Cladding index (n2) | 1.4641 |

| | |
|---|---|
| Core diameter (μm) | 8.2 |
| Cladding size (μm) | 30 |
| Δ | 0.4% |

In the preceding chapter, we explicated the degeneracy of fiber modes. As depicted in Fig.2-7, the LP11 mode is four-fold degenerate. The orientation of the intensity distribution bifurcates the four degenerate states of LP11 into two categories: horizontal and vertical. Each category can be further sub-divided into x and y types based on the polarization direction. In the model portrayed in Fig.3-2, we designate the LP11 modes with the intensity distribution directions of horizontal and vertical as LP11_b and LP11_a, respectively. When coupled with their corresponding polarization directions, four permutations emerge: LP11_a_x, LP11_a_y, LP11_b_x, and LP11_b_y. The LP01 mode, bereft of any variance in the direction of intensity distribution, is classified solely into LP01_x and LP01_y, according to the polarization direction. The relevant distinctions are represented in the subsequent table:

Table 3-2 Degeneracy-resolved LP mode profile

| Polarization | LP01 | LP11_a | LP11_b |
|---|---|---|---|
| x | 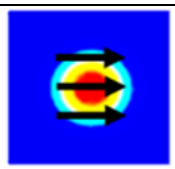 | 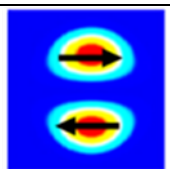 | 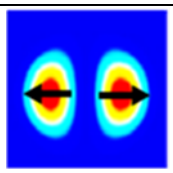 |
| y | 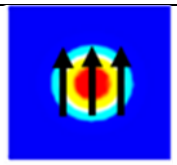 | 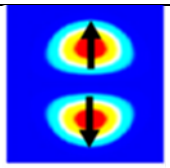 | 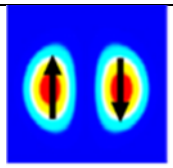 |

In Fig.3-2, the bending occurs within the horizontal plane. Therefore, the bending loss of LP11_b will be higher than that of LP11_a [3]. Based on this model, we calculated the bending loss for bending radii ranging from 4mm to 16mm. The results are shown in the

following graph:

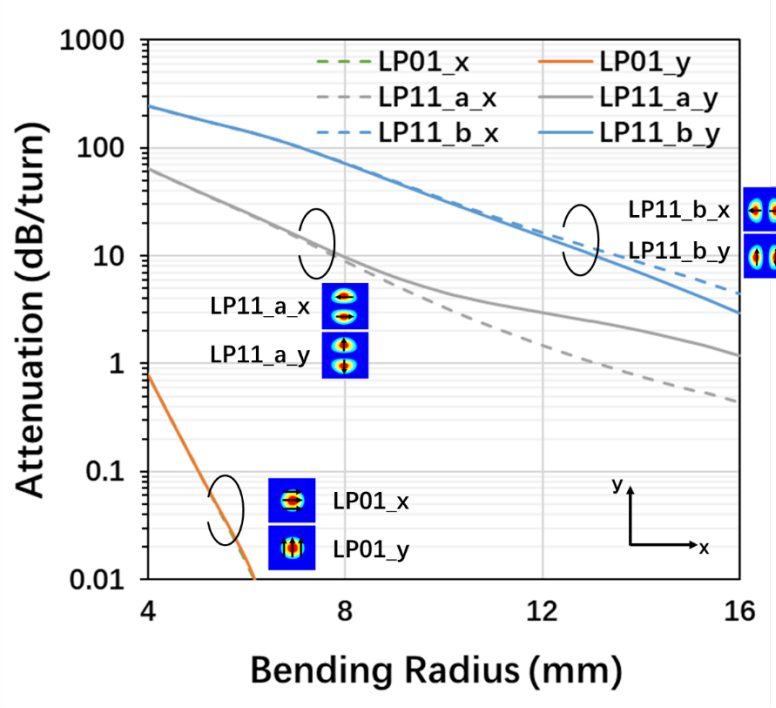


Fig. 3-3 Simulation result of bending loss for both LP01 and LP11 mode

The computational results reaffirm our expectations; at an equivalent bending radius, the bending loss of the LP11 mode significantly outstrips that of the LP01 mode. Moreover, when the bending radius exceeds 6mm, the bending loss of the LP01 mode falls below 0.01dB/turn, rendering it negligible. Even within the realm where the bending radius is less than 8mm, LP11_a, which exhibits the lesser bending loss compared to LP11_b, still incurs a loss exceeding 10dB/turn. This substantial disparity in bending loss unequivocally ensures that the LP01 mode is retained while the LP11 mode is filtered out, laying the groundwork for a bent fiber-based mode filter.

In devising a mode filter, one must weigh the bending losses of LP01 and LP11 modes against the constraints imposed by practical scenarios. For instance, if available space and the length of fiber reserved are limited, it may not be feasible to attain a larger bending radius and the requisite number of bending turns. In cases where a smaller bending radius

is sought, the mechanical reliability of the fiber must be taken into account to safeguard against potential damage such as fiber breakage due to tight bends [4]. Through our model, the mode filter can be designed to adapt to these varying circumstances, and its performance can be forecasted accordingly.

## 3.2 Measurement of bending loss

In this section, we will undertake the task of measuring the bending loss inherent to the conventional single-mode fiber. Through juxtaposing the measurement outcomes with the simulation results derived in section 3.1, we aim to ascertain the validity of our bending-loss simulation model. The measurement of LP11 mode bending loss necessitates the initial generation of a stable, suitably intense LP11 mode light within the fiber to meet measurement requirements. To achieve this, we propose to excite the LP11 mode by splicing fiber with a lateral offset [5]. The efficacy of this approach has been both simulated and tested experimentally, details of which will be expounded in section 3.2.1.

### *3.2.1 Simulation and experiment of lateral-offset spliced fiber*

The selective excitation of modes has been a subject of numerous studies, with approaches encompassing mode selective couplers [6], fiber Bragg gratings [7], and phase masks [8], among others. These methodologies exhibit high efficiency in the excitation of higher-order modes. However, it is undeniable that these techniques are intricate, necessitating the employment of specialized optical devices and the establishment of corresponding systems to effectuate their functions.

In a 1060nm optical communication system predicated on conventional single-mode fiber,

even when the light source employed is a single-mode laser solely emitting the LP01 mode, lateral offsets and other imperfections at the fiber connection points are inevitable. These faults trigger a coupling loss of the LP01 mode, thereby stimulating the LP11 mode. This phenomenon was delineated in detail in section 2.2.1. Consequently, we posit that by augmenting the lateral offset at the fiber connection point, a more pronounced excitation efficiency of the LP11 mode can be realized. We have simulated this strategy, and the schematic representation of the simulation model is as follows:

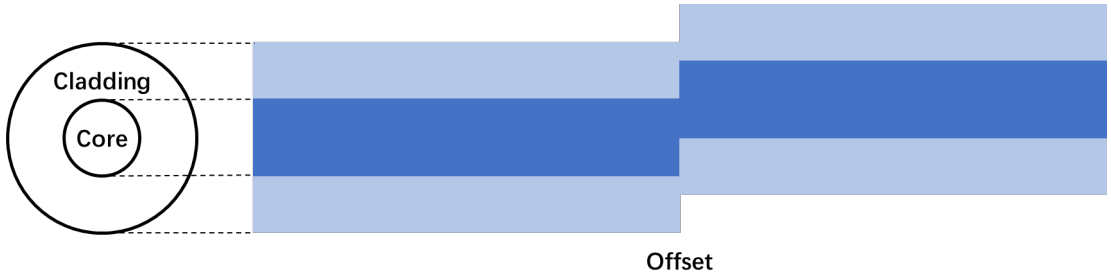


Fig. 3-4 Simulation model of LP11 excitation by lateral offset splicing

The structure and parameters of the simulation model draw upon the characteristics of the SMF28-ULTRA fiber. Since our focus is on the investigation of the impact of lateral offset on LP01 mode coupling loss and LP11 mode excitation efficiency, in contrast to the square cladding design implemented in section 3.1, we meticulously adhere to the fiber's parameters in this instance, representing the cladding as a circle with a diameter of 125μm. The settings for the refractive index mirror those in Table 3-1. The ensuing simulation outcomes are presented as follows:

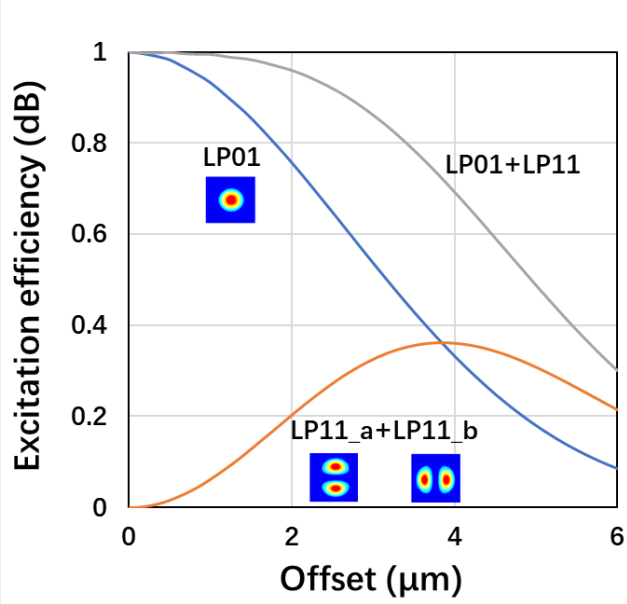


Fig. 3-5 Simulation result of LP01 coupling loss and LP11 excitation ratio vs lateral offset at 1060nm (LP01 input only)

In our simulation, the incident light is designated to be exclusively in the LP01 mode. The lateral offset at the fiber junction varies from 0 to 6μm. The blue curve in the graph symbolizes the coupling efficiency of the LP01 mode, the orange curve signifies the excitation efficiency of the LP11 mode, and the grey curve represents the aggregate efficiency of the two modes. The results for LP11 encapsulate the sum of all degenerate modes (LP11_a and LP11_b).

Evidently, the coupling efficiency of the LP01 mode diminishes monotonically as the offset amplifies. Conversely, the excitation efficiency of LP11 initially increases, subsequently decreases, and attains its peak value at approximately 4μm offset. Given that our intention is to excite the LP11 mode via offset splicing of the fiber, the simulation results suggest that the offset should be managed at around 4μm.

For the experimental component, we employed the Fujikura 90S+ fiber fusion splicer.


Fig. 3-10 Fujikura 90S+ fiber splicer [9]

This device boasts an offset splicing feature, facilitating manual adjustment of the fiber offset. This adjustment can be performed by monitoring the position of the fiber as displayed on the screen, as depicted in the ensuing figure:

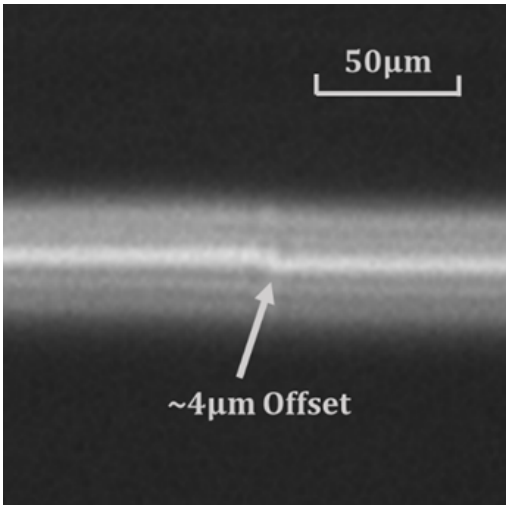


Fig. 3-11 The image on the monitor of 90S+ splicer during fiber fusion

Given our necessity to compare the coupling efficiency acquired from experimental measurements post-splicing with the simulation results, it's crucial to ascertain the precise

offset at the splicing juncture. Regrettably, this offset cannot be directly measured using a microscope or other such techniques. To circumvent this issue, we propose to indirectly glean the offset by measuring the coupling loss of light at 1310nm. This is premised on the fact that our simulation model is predicated on conventional single-mode fiber. At the operational wavelength of 1310nm, the fiber solely supports the LP01 mode. This stipulates that the energy loss within the fiber will not continue to propagate in the form of higher-order modes, and the loss of LP01 is tantamount to the system loss. Consequently, as long as we discern the relationship between coupling loss and offset at 1310nm, we can determine the offset by measuring the system loss.

Drawing from the model portrayed in Fig.3-4, we computed the relationship between the coupling efficiency of the LP01 mode and the lateral offset at 1310nm. The outcome is displayed as follows:

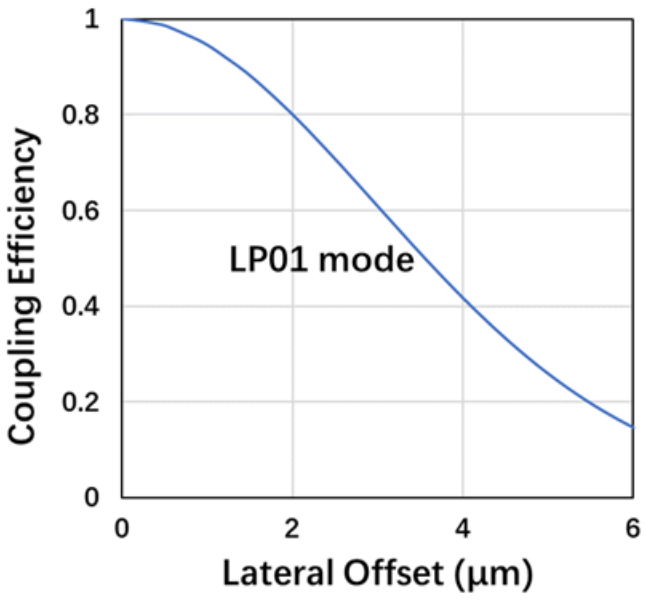


Fig. 3-12 Simulation result of LP01 coupling vs lateral offset at 1310nm

For the experimental phase, we utilized three 5m-long SMF28-ULTRA fibers. Initially,

they were each connected to a 1310nm single-mode laser, and the same power meter was employed to record the output power of each fiber. The fibers were subsequently severed and offset-spliced, adjusting the offset at the splice point to be as proximate to 4μm as feasible. The spliced fibers were then reconnected between the laser and the power meter, and the output power of each fiber was logged. The coupling efficiency at the splice point of each fiber can be derived by comparing the power pre- and post-splicing. The coupling efficiencies of these three fibers, ordered from highest to lowest, are 60%, 40%, and 35%, respectively. Referring to the results displayed in Fig.3-8, the offsets at the splice points of the three fibers are 2.9μm, 4.1μm, and 4.4μm, respectively.

Given our knowledge of the offset of each fiber, the experiment at 1060nm could be executed. The experimental process and apparatus diagram is delineated as follows:

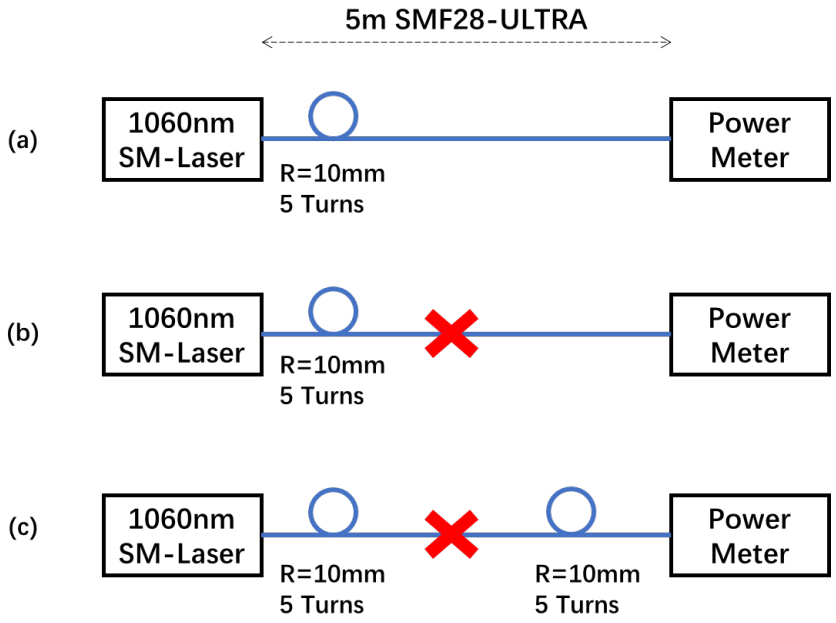


Fig. 3-13 Experiment set-up and process for coupling efficiency measurement at 1060nm

Firstly, prior to severing the fiber, we measured its output power under a 1060nm single-

mode laser, designated as $P_a$. As visible, we incorporated a single bend in the fiber after the laser, with a bend radius of 10mm and it was wound 5 turns. As per the computation result displayed in Fig.3-3, this bend embodies a rejection ratio exceeding 20dB for the LP11 mode, but has no impact on LP01. Consequently, it can be assured that only the light in the LP01 mode continues to propagate in the fiber post-bending.

Subsequently, we measured the output power post-offset fusion, denoted as $P_b$. $P_b$ encompasses the power of LP01 and LP11 after coupling, and its ratio to $P_a$ should conform to the grey curve (LP01+LP11) depicted in Fig.3-5.

Lastly, following the splice point, the fiber is bent yet again with a radius of 10mm and wound 5 turns. In this circumstance, the LP11 mode is entirely filtered out, while the LP01 mode remains unaffected. Thus, the measured result, $P_c$, represents the power of LP01, and $P_b - P_c$ represents the power of LP11. Their respective ratios to $P_a$ represent the blue (LP01) and orange (LP11) curves in Fig.3-5. The juxtaposition of the experimental results with the simulation results is illustrated in the ensuing figure:

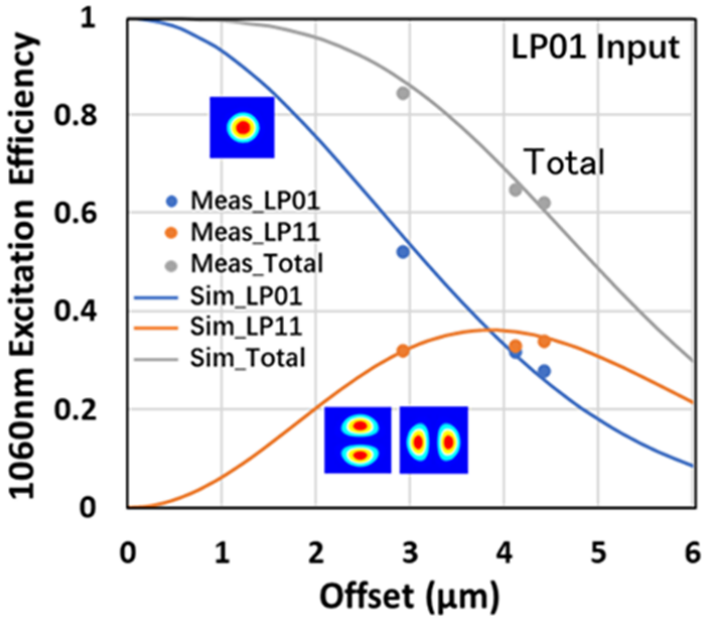


Fig. 3-14 Comparison of measurement and simulation result about LP01 and LP11 excitation efficiency under 1060nm

As observed, the experimental outcomes under three distinct offset values correspond closely with their respective simulation results. This observation verifies the high degree of precision inherent in our simulation model. Concurrently, it also suggests that offset splicing can serve as an effective strategy for exciting the LP11 mode. When the offset is set at 4μm, the maximum excitation efficiency can approach nearly 40%. Furthermore, considering that at this juncture the total power (LP01+LP11) within the fiber constitutes merely about 70% of the incident light, it infers that at this point, the power of LP11 makes up more than half of the total power (LP01+LP11). This proportion adequately fulfills our requirements for bending loss testing.

### *3.2.2 Bending loss measurement and analysis*

Given that we utilize the approach of offset splicing to excite the LP11 mode, the LP01

and LP11 modes coexist within the fiber. When the fiber undergoes bending, potential losses could simultaneously impact both modes. In this circumstance, we must initially measure the bending loss of LP01 mode, following which we can compute the bending loss of the LP11 mode based on the measured total loss. The experimental setup and the corresponding process are outlined as follows:

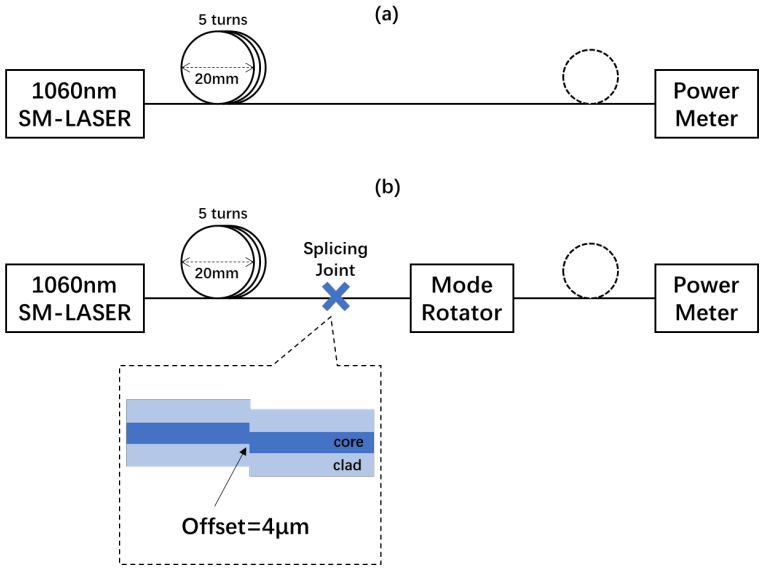


Fig. 3-15 Experiment set-up for bending loss measurement

In this experiment, we continue to use the SMF28-ULTRA fiber. As we previously depicted in Fig. 3-9, we initiate a bend in the fiber with a radius of 10mm and repeat this for 5 turns after the light source, thus ensuring that only the LP01 mode light can propagate onwards. Fig. 3-11(a) and Fig. 3-11(b) are respectively employed to measure the bending loss of the LP01 and LP11 modes. The dashed circles within the figures represent the bending radius to be measured. In Fig. 3-11(b), the fiber is fused with a lateral offset of 4μm to attain the maximum excitation ratio of the LP11 mode. Due to the strong dependence of the LP11 mode's bending loss on the direction of its intensity distribution, we introduce a polarization controller post the fiber's splicing joint, serving as a mode rotator [10]. With the same testing radius, different bending loss values can be

recorded by adjusting the mode rotator to alter the intensity distribution direction of the LP11 mode. The maximum and minimum values of the loss correspond to LP11_b and LP11_a defined in Fig.3-3, respectively.

Throughout the experiment, we choose several cylinders with varying radii as mandrels. By winding the fiber around them, we are able to achieve different bending radii. As shown in the following figure:

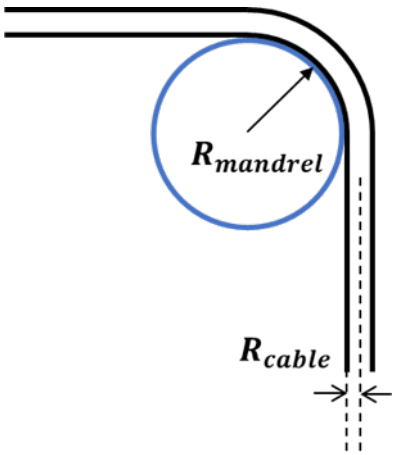


Fig. 3-16 Schematic diagram of bent fiber

Indeed, that's an important factor to consider. The SMF28-ULTRA fiber is enclosed within a protective sheath or cable. If we envision this cable as a uniform cylinder, its radius ($R_{cable}$) measures 0.45mm, as illustrated in Fig.3-12. Therefore, the effective bending radius of the fiber ($R_{eff}$) is equivalent to the sum of the radius of the mandrel ($R_{mandrel}$) and the radius of the cable ($R_{cable}$). This adjustment needs to be incorporated in our calculations to maintain accuracy.

$$R_{eff} = R_{mandrel} + R_{cable} \qquad (3-1)$$

The simulated results presented in Fig.3-3 demonstrate that when the bending radius surpasses 6mm, the bending loss associated with the LP01 mode can be considered negligible (less than 0.01dB/turn). Additionally, a bending radius smaller than 6mm could

potentially compromise the mechanical reliability of the fiber. Accordingly, in this experiment, we selected bending radii all greater than 6mm. The effective radii ($R_{eff}$) were chosen as 6.45mm, 10.45mm, 12.95mm, and 15.3mm. The loss of the LP01 mode under these bending radii was measured using the apparatus displayed in Fig. 3-11(a). The experimental observations revealed that irrespective of the number of turns, the fiber output power remained constant. This reinforces our simulation prediction that for a bending radius greater than 6mm, the bending loss of the LP01 mode is indeed negligible. This holds great implications for us as it signifies that when designing a mode filter, if system conditions can accommodate a bending radius greater than 6mm, it can assure that the mode filter will not incur any insertion loss.

Moreover, the negligible loss of the LP01 mode indicates that when we measure the loss of the LP11 mode under these bending radii, the measured power loss is solely attributed to the LP11 mode. This simplifies our experimental procedure to determine the bending loss of the LP11 mode.

The measurement of the bending loss of the LP11 mode was executed through the following sequence. Initially, no bending of the fiber was conducted after the mode rotator as depicted in Fig. 3-11(b). The total output power for both LP01 and LP11 modes was recorded as $P_T$. Subsequently, the fiber was bent 5 turns with a radius of 10mm to filter out all LP11 modes. The measured power in this scenario was noted as $P_{01}$, symbolizing the power of the LP01 mode within the system. Therefore, the power of LP11 can be calculated as $P_T - P_{01}$. Later, we wound the fiber n times with the testing radius and recorded the power at this time as $P_n$. The bending loss of the LP11 mode ($BL_{LP11}$) could then be determined using the ensuing formula.

$$BL_{LP11} = \sqrt[n]{\frac{P_T - P_n}{P_T - P_{01}}} \qquad (3-2)$$

The formula in decibel form is:

$$BL_{LP11}(dB/turn) = 10log\ (BL_{LP11}) \qquad (3-3)$$

In accordance with the aforementioned procedure, and through the deployment of the mode rotator, we gauged the bending loss of LP11_a and LP11_b under the effective bending radii ($R_{eff}$) of 6.45mm, 10.45mm, 12.95mm, and 15.3mm, respectively. The recorded results were subsequently juxtaposed with the simulated results showcased in Fig.3-3, as illustrated in the ensuing figure:

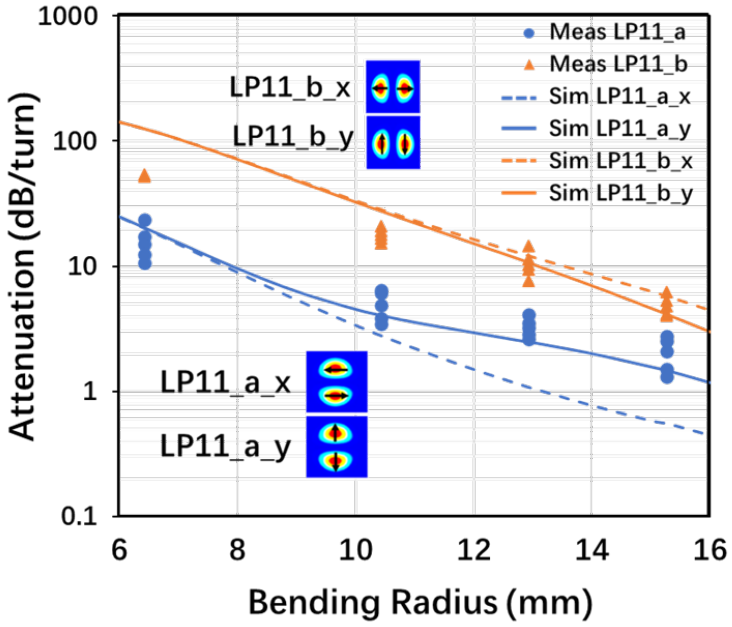


Fig. 3-17 Comparison of measurement and simulation results for LP11 bending loss

In each bending radius, multiple measurements were conducted, and the overall experimental results closely align with the simulation results depicted in Fig.3-13. However, it should be noted that at smaller bending radii, the bending loss of LP11_b becomes extremely large. Even slight changes in the bend angle can lead to significant

power fluctuations, resulting in a relatively larger margin of error in the experimental results.

The bending loss measurement experiment effectively validated the reliability of our simulation model. By utilizing our model, we can confidently design a bending fiber mode filter and accurately predict its effectiveness. This is of utmost importance for data transmission systems reliant on conventional single-mode fiber and 1060nm single-mode VCSEL lasers.

## Reference in Chapter 3


3-1 T. Matsui, K. Nakajima, and T. Sakamoto, "Effective mode-field diameter for few-mode fibers for considering splice loss characteristics," Appl. Opt. 56(26), 7484–7490 (2017).

3-2 “https://www.corning.com/optical-communications/worldwide/en/home/products/fiber/optical-fiber-products/smf-28-ultra.html”

3-3 C. Schulze, A. Lorenz, D. Flamm, A. Hartung, S. Schröter, H. Bartelt, and M. Duparré, "Mode resolved bend loss in few-mode optical fibers," Opt. Express 21(3), 3170–3181 (2013).

3-4 G. S. Glaesemann and R. J. Castilone, "The Mechanical Reliability of Corning® Optical Fiber in Bending," Corning White Paper 3690 (2002).

3-5 F. Xia, Y. Zhao, H. Hu, and Y. Zhang, "Broadband generation of the first-order OAM modes in two-mode fiber by offset splicing and fiber rotating technology," Opt. Laser Technol. 112, 436–441 (2019).

3-6 H. Yao, F. Shi, Z. Wu, X. Xu, T. Wang, X. Liu, P. Xi, F. Pang, and X. Zeng, "A

mode generator and multiplexer at visible wavelength based on all-fiber mode selective coupler," Nanophotonics 9(4), 973–981 (2020).

3-7 Y. Fazea and V. Mezhuyev, "Selective mode excitation techniques for mode-division multiplexing: A critical review," Opt. Fiber Technol. 45, 280–288 (2018).

3-8 W. Mohammed, M. Pitchumani, A. Mehta, and E. G. Johnson, "Selective excitation of the LP 11 mode in step index fiber using a phase mask," Opt. Eng. 45(7), 074602 (2006).

3-9 https://www.aflglobal.com/en/Products/Fusion-Splicing/Field-Fusion-Splicing-Equipment/Splicers-Single-Fiber/Fujikura-90S-Fusion-Splicer

3-10 Z. Hong, S. Fu, D. Yu, M. Tang, and D. Liu, "All-fiber tunable LP 11 mode rotator with 360° range," IEEE Photon. J. 8(5), 1–7 (2016).

# Chapter4

# Design and characterization of 90-degree fiber array based compact mode filter

Based on our analysis and experimental findings, bent fiber emerges as an ideal solution for high-order mode filtering. However, this approach does come with certain limitations. In cases where practical conditions cannot accommodate a large bend radius or multiple bending turns, the fiber may need to be bent with a smaller radius. Unfortunately, the smaller the bending radius, the higher the stress exerted on the fiber, thereby increasing the likelihood of fiber breakage or other forms of damage. Consequently, it is imperative to explore new solutions to address situations involving small-radius bending.

In general, 90-degree fiber arrays exhibit very small bend radii. During their manufacturing process, the fiber is heated to approximately 1300 degrees Celsius, which is around the glass softening point [1]. Bending the fiber at a small radius under these conditions can circumvent the generation of stress, thereby safeguarding the fiber against damage. By selecting an appropriate type of fiber and bend radius during the fabrication of the fiber array, it is possible to achieve the automatic functionality of a mode filter, as illustrated in the following figure:

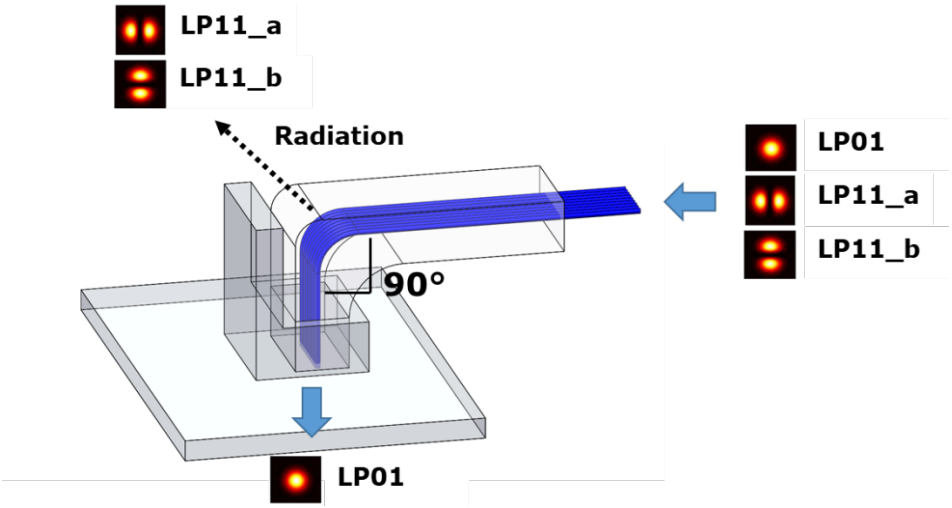


Fig. 4-1 90-degree fiber-array based mode filter

Furthermore, if the 90-degree fiber array can fulfill both light transmission and mode filtering functions, there would be no necessity to introduce additional mode filters into the optical communication system. This would not only lead to cost reduction but also obviate insertion losses associated with other devices.

Moving forward, we will undertake simulations and experiments involving three different types of fibers to elucidate the characteristics of the most suitable fiber for constructing fiber arrays with mode filtering capabilities.

## 4.1 Simulation of bending loss for three different kinds of fiber

We have defined three types of fibers for our study: fiber_A, fiber_B, and fiber_C. These fibers adhere to the G.652-D, G.657-A1, and G.657-B3 standards, respectively, as established by the ITU-T [2]. The primary distinction among them lies in their bending sensitivity. Specifically, G.652-D exhibits the highest bending sensitivity, followed by G.657-A1, while G.657-B3 has the lowest. Consequently, under identical bending radii and angles, these fibers will manifest varying degrees of bending losses.

To accommodate these standards, we have devised distinct structures and parameters for the simulation models of fibers A, B, and C. Fiber_A and fiber_B are step-index fibers, featuring different parameters, while fiber_C is a trench-index fiber. Here is a concise overview of each fiber:

Firstly, let's consider fiber_A and fiber_B. The refractive index distributions and cross-sectional structures of their simulation models are depicted in the ensuing figure. As expounded in Section 3.1, for the sake of computational convenience, we have designed the cladding section in a square shape. As long as the side length of the square is sufficiently large, its shape will not impact the simulation results.

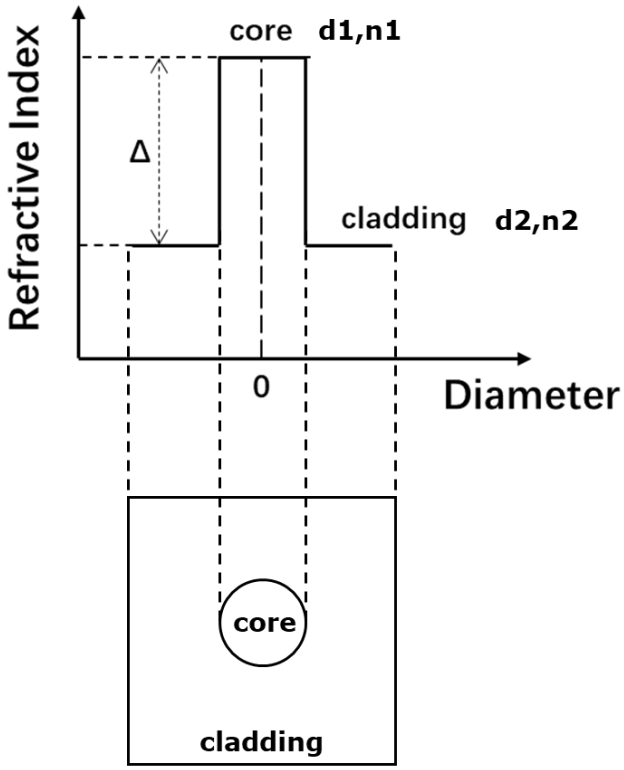


Fig. 4-2 Schematic diagram of simulation model for fiber_A and fiber_B

The parameters of the fiber_A and fiber_B models are shown in the following table:

Table 4-1 Parameters used for fiber_A and fiber_B

| | fiber_A | fiber_B |
|---|---|---|
| n1 | 1.47 | |
| n2 | 1.4647 | 1.4641 |
| Δ | 0.36% | 0.4% |
| d1 (μm) | 9 | 8.2 |
| d2 (μm) | 30 | |

In order to meet the stringent requirements of the G.657-B3 standard, fiber_C adopts a trench-type structure that possesses enhanced field confinement capabilities [3]. The schematic diagram of this structure is presented in the following figure:

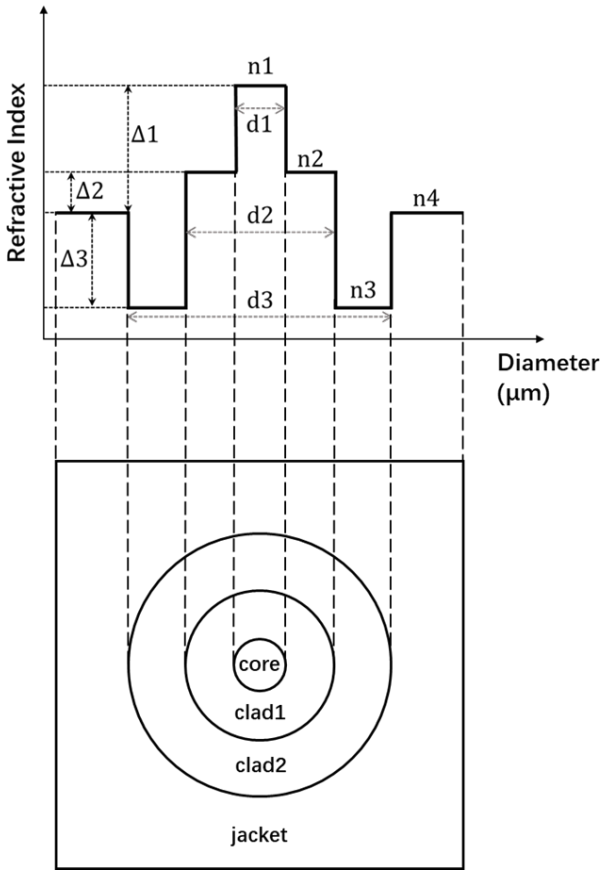


Fig. 4-3 Schematic diagram of simulation model for fiber_C

The trench-type fiber, owing to the inclusion of a low refractive index layer (n3),

facilitates a higher degree of light reflection back into the core. Consequently, when compared to step-index fiber, the trench-type fiber exhibits improved resistance to bending. Notably, certain parameters of fiber_C have been derived from the trench-type bend-insensitive fiber manufactured by Sumitomo company [4]. A comprehensive overview of these parameters is presented in the following table:

Table 4-2 Parameters used for fiber_C

| | Core | Clad1 | Clad2 | Jacket |
|---|---|---|---|---|
| n | 1.4676 | 1.4627 | 1.4537 | 1.4625 |
| d (μm) | 7.3 | 15.21 | 26.55 | 50 |

Utilizing the aforementioned parameters and structure, it has been determined that the mode field diameter of fiber_C measures 8.3μm at 1310nm, while the bending loss at a bending radius of 5mm at 1550nm amounts to 0.15dB/turn. These outcomes align precisely with the specifications set forth by the G.657-B3 standard, thus affirming the validity of the fiber_C model.

Furthermore, the 90-degree bending losses of these three fiber types have been calculated at bending radii ranging from 1mm to 4mm, employing the aforementioned fiber models. The calculation results are illustrated in the subsequent figure:

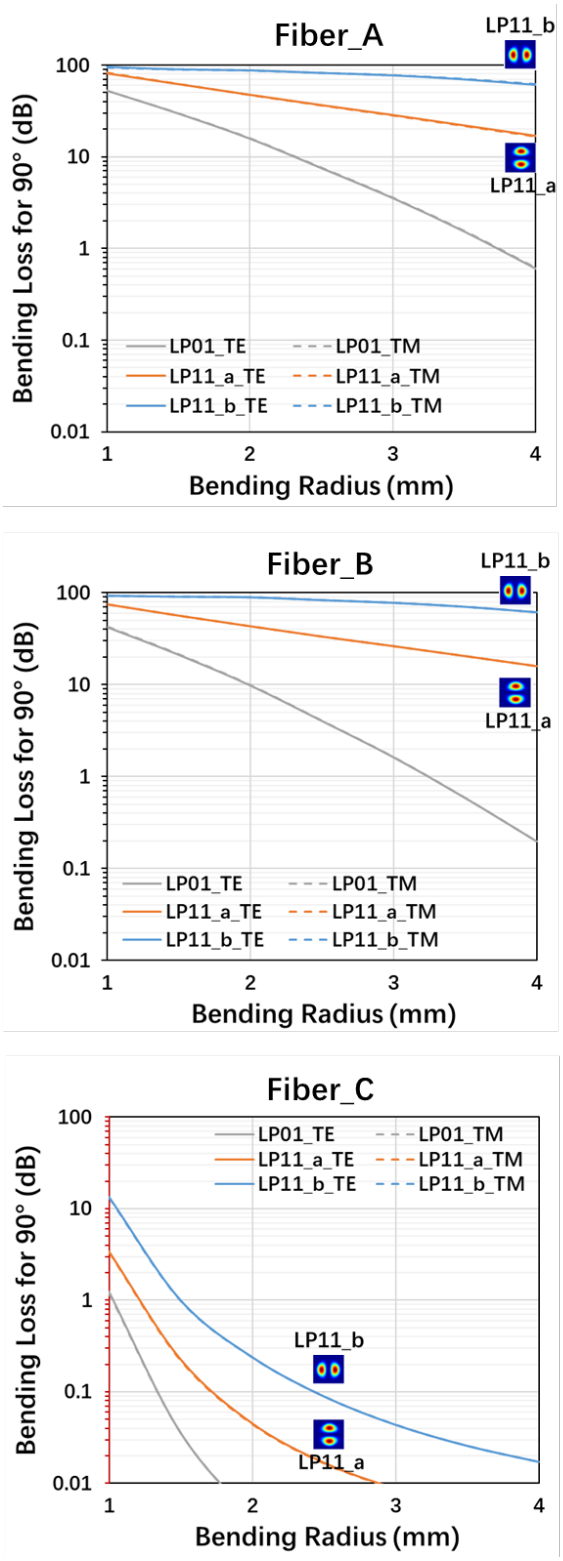


Fig. 4-4 Simulation results of bending loss for 3 types of fiber

The simulation results clearly indicate that fiber_C, with its strong resistance to bending,

exhibits significantly lower bending losses compared to the other two fibers. Remarkably, the LP11 mode loss of fiber_C is even lower than the LP01 mode loss of the other fibers. Consequently, fiber_C ensures that fiber arrays constructed from it possess minimal insertion losses. However, such a low LP11 mode loss renders fiber_C unsuitable for use as a mode filter.

When comparing the simulation results of fiber_A and fiber_B, it becomes evident that their LP11 mode losses are quite similar. However, fiber_B demonstrates only half the LP01 mode loss of fiber_A, owing to its superior bend insensitivity. Consequently, in terms of fabricating fiber arrays endowed with mode filtering functionality, fiber_B proves more suitable than fiber_A, as it introduces smaller insertion losses to the system. Based on the simulation results of fiber_B, a bending radius of 3.5mm appears to be an optimal choice. At this radius, the LP11 mode loss exceeds 20dB, while the LP01 mode loss remains below 1dB. The subsequent step entails validating this outcome through experimental means.

## 4.2 Bending loss measurement

Since fiber_C does not possess the appropriate characteristics to function as a mode filter, we will solely measure the bending losses of fiber_A and fiber_B. For the measurements, we will employ OS2 fiber, which adheres to the G.652-D standard, with its results aligning with the simulation results of fiber_A. As for SMF28-ULTRA fiber, its bend resistance is slightly superior to that of G.657-A1, and its bending loss measurements will be compared against the simulation results of fiber_B.

The experimental setup remains consistent with Fig.3-19. Specifically, LP01 mode is measured using an intact fiber, while the LP11 mode is excited through fiber with a lateral

offset splicing joint of 4μm, as depicted in Fig.3-19(b). By implementing a polarization controller within the fiber to manipulate the direction of intensity distribution of the LP11 mode, we can measure the bending losses of LP11_a and LP11_b individually. It should be noted that the polarization controller we employ is compatible solely with SMF28-ULTRA cable, therefore the measurements for OS2 fiber will not differentiate between LP11_a and LP11_b.

As mentioned in Chapter 3, since both LP01 and LP11 modes coexist in the fiber, it is imperative to first measure the bending loss of the LP01 mode. Subsequently, this result can be integrated with the experimental results of the LP11 mode to calculate the bending loss of the LP11 mode.

To measure the bending loss of the LP01 mode, we utilize the experimental setup illustrated in Fig.3-19(a). The bending loss of the LP01 mode is acquired by calculating the power difference and the number of bending turns between two experiments. This methodology effectively avoids errors stemming from coupling losses in the bent fiber.

When light traverses a bent fiber, its mode field undergoes a shift towards the outer region of the bent fiber. The smaller the bending radius, the more pronounced the mode field shift. At the inception of fiber bending, the connection between the straight fiber and the bent fiber can be considered. On one side of this connection is the straight fiber, with the mode field predominantly concentrated in the core's center. On the other side lies the bent fiber, where the mode field experiences a shift. Consequently, a mode field mismatch transpires at this connection, leading to coupling losses [5], as illustrated in the ensuing figure:

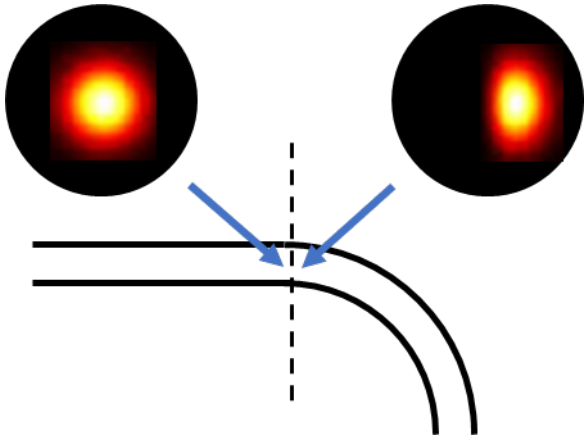

Fig. 4-5 Mode field mismatch between straight and bent fiber

In our experiment, the fiber is wound on a cylinder with a specific radius, and regardless of the number of turns, the coupling loss only occurs once at the beginning and end of the winding. Consequently, by calculating the difference in output power between two different winding numbers, the coupling loss can be effectively eliminated. The resulting power difference is solely determined by the variance in the number of winding turns.

Let's assume that the number of winding turns in the two experiments is denoted as "a" and "b", respectively, and the corresponding output powers are represented as "$P_a$" and "$P_a$". Consequently, the bending loss of the LP01 mode ($BL_{LP01}$) can be determined using the following formula:

$$BL_{LP01} = \sqrt[|a-b|]{|P_a - P_b|} \qquad (4-1)$$

Once the bending loss of the LP01 mode has been determined, we can proceed to measure the bending loss of the LP11 mode. The measurement process mirrors the procedure outlined in Chapter 3. However, since the bending radius employed in Chapter 3 was large, resulting in negligible loss for the LP01 mode, the bending loss of the LP01 mode could be disregarded. In this case, however, the bending loss of the LP01 mode cannot be neglected when the bending radius falls below 4mm. Consequently, we need to modify Eq.3-2 by incorporating the loss of the LP01 mode. The adjusted expression for the

bending loss of the LP11 mode is as follows:

$$BL_{LP11} = \sqrt[n]{\frac{P_T - P_n + BL_{LP01}^n}{P_T - P_{01}}} \qquad (4-2)$$

In the measurement process, $P_T$ represents the output power when the fiber is not bent, reflecting the total power of both the LP01 and LP11 modes. $P_{01}$ corresponds to the output power when the fiber is bent with a radius of 10mm for 5 turns, specifically representing the power of the LP01 mode within the fiber. Consequently, $P_T - P_{01}$ represents the total power of the LP11 mode. On the other hand, $P_n$ represents the output power after bending the fiber at the test radius for n turns. Hence, $P_T - P_n$ reflects the total loss resulting from the fiber bending in this experiment. By subtracting the loss caused by the LP01 mode, denoted as $BL_{LP01}^n$, from this value, we obtain the loss of the LP11 mode. Consequently, the bending loss of the LP11 mode at the specific bending radius can be determined based on the number of bends, $n$.

In our experiment, we have measured the bending loss of two distinct fiber types. The cylinders employed to wind the fiber during the experiment possessed three different radii: 1mm, 2mm, and 3mm. Furthermore, the cable radii ($R_{cable}$) of the OS2 and SMF28-ULTRA fibers were 1mm and 0.45mm, respectively. To calculate the effective bending radius ($R_{eff}$), the sum of the cylinder radius and the cable radius should be utilized.

We have compared the measured bending losses with the simulation results depicted in Fig.4-4, as presented in the subsequent figure. The dots within the figure represent the measurement results, with the corresponding radius representing the actual radius ($R_{eff}$).

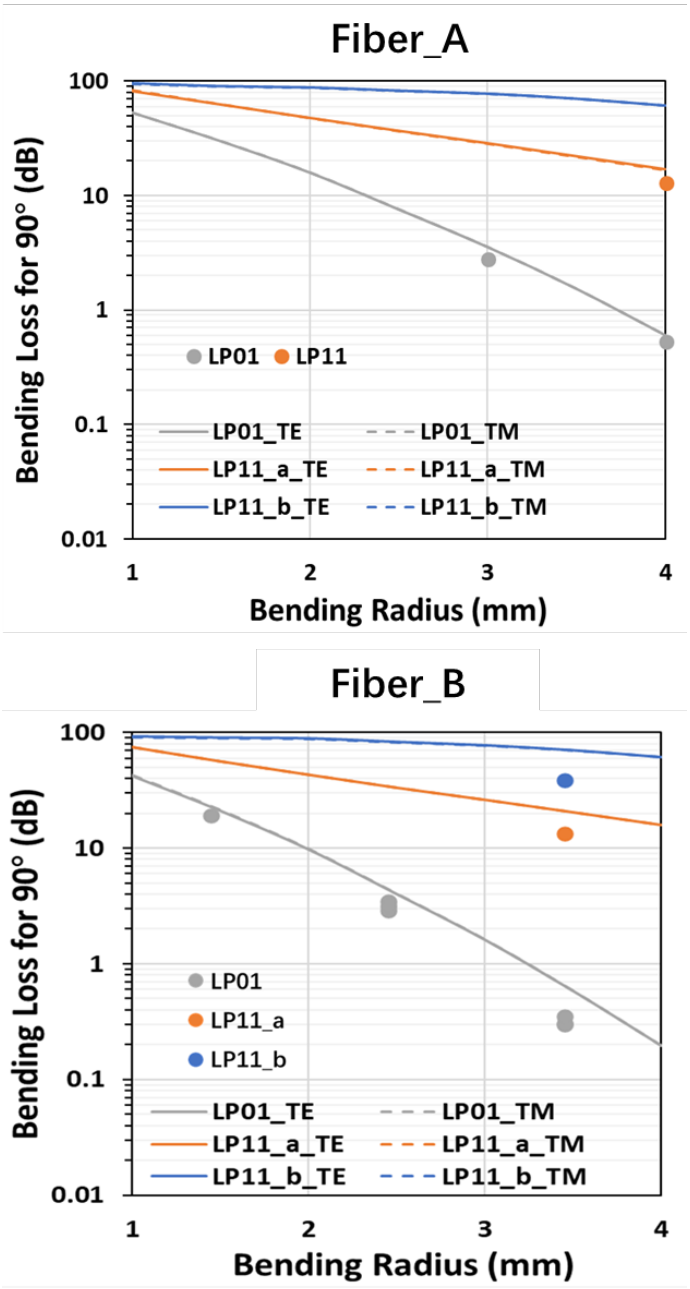


Fig. 4-6 Comparison of simulation and measurement result of bending loss for fiber_A and fiber_B

The experimental results for both types of fibers align closely with their respective simulation results. Due to the significant bending loss of the LP11 mode under small radius bending, we were only able to measure data for a cylinder radius ($R_{mandrel}$) of

3mm within our experimental conditions. As a result, there is only one data point for the measured value of the LP11 mode bending loss in each figure.

The slightly lower bending loss measurements compared to the simulation in the fiber_B figure can be attributed to the stronger bending resistance of SMF28-ULTRA compared to the G.657-A1 standard. This outcome translates to lower insertion loss, which is beneficial for our purposes. At an effective bending radius of 3.45mm, the loss of the LP01 mode is only around 0.3dB. In contrast, even for LP11_a, which exhibits lower bending loss, the loss can still reach nearly 20dB. This level of loss is sufficient to fulfill the mode filtering function.

The results of this experiment validate the accuracy of our established simulation model. They demonstrate that by selecting the appropriate fiber type and bending radius for manufacturing a 90-degree fiber array, the product can inherently possess the functionality of a mode filter. This outcome greatly enhances the transmission capability of 1060nm data transmission systems based on conventional single-mode fiber.

## 4.3 Simulation of coupling loss for straight-to-bent fiber connection

In research concerning 90-degree fiber arrays, the coupling loss that occurs between a bent fiber and a straight fiber is an important factor that must be considered. In the previous section, we provided a brief explanation of the underlying cause of this coupling loss. In this section, we will delve into a more detailed discussion of this phenomenon.

When a bent fiber is connected to a straight fiber, there is a mode field mismatch between them, resulting in coupling loss. In our optical system, since the fiber is capable of

supporting two modes, namely LP01 and LP11, a portion of the energy lost due to LP01 coupling loss can lead to the excitation of the LP11 mode. This process is depicted in the accompanying figure:

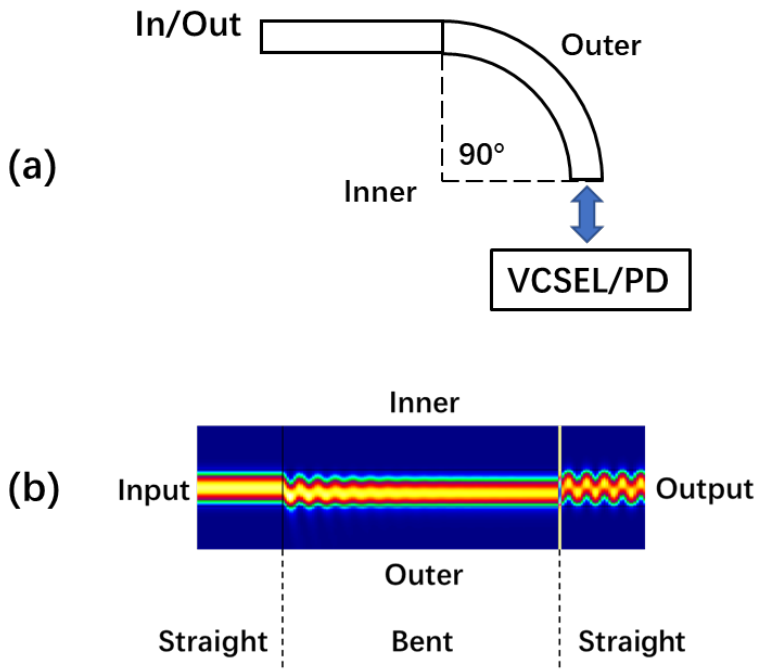


Fig. 4-7 Coupling loss of straight-to-bent fiber connection

In the context of optical communication systems, 90-degree fiber arrays are commonly employed at both the transmitter and receiver ends. At one end of the 90-degree bent section, a straight fiber is connected, while the other end is linked to a light source or optical receiver. Regardless of whether it is a light source or a optical receiver, when discussing the mode field at these ends, we can consider them as equivalent to a section of straight fiber.

Figure 4-7(b) illustrates the variation in the mode field distribution as light propagates through a fiber array. Initially, only the fundamental mode is present when the light is incident from the left. At the first straight-bent junction on the left, coupling loss occurs, leading to the excitation of the LP11 mode. It can be observed that the mode field in the

bent fiber is skewed towards the outer region. Due to the significant loss experienced by the LP11 mode in the bent fiber, its presence gradually diminishes as it propagates through the bent fiber. However, at the second straight-bend interface, coupling loss occurs once again, resulting in the generation of new LP11 modes. This outcome indicates that the 90-degree fiber array has a detrimental effect on the system. We conducted calculations to determine the coupling loss and the excitation ratio of the LP11 mode caused by the straight-bent fiber connection using the fiber_B model. The obtained results are as follows:

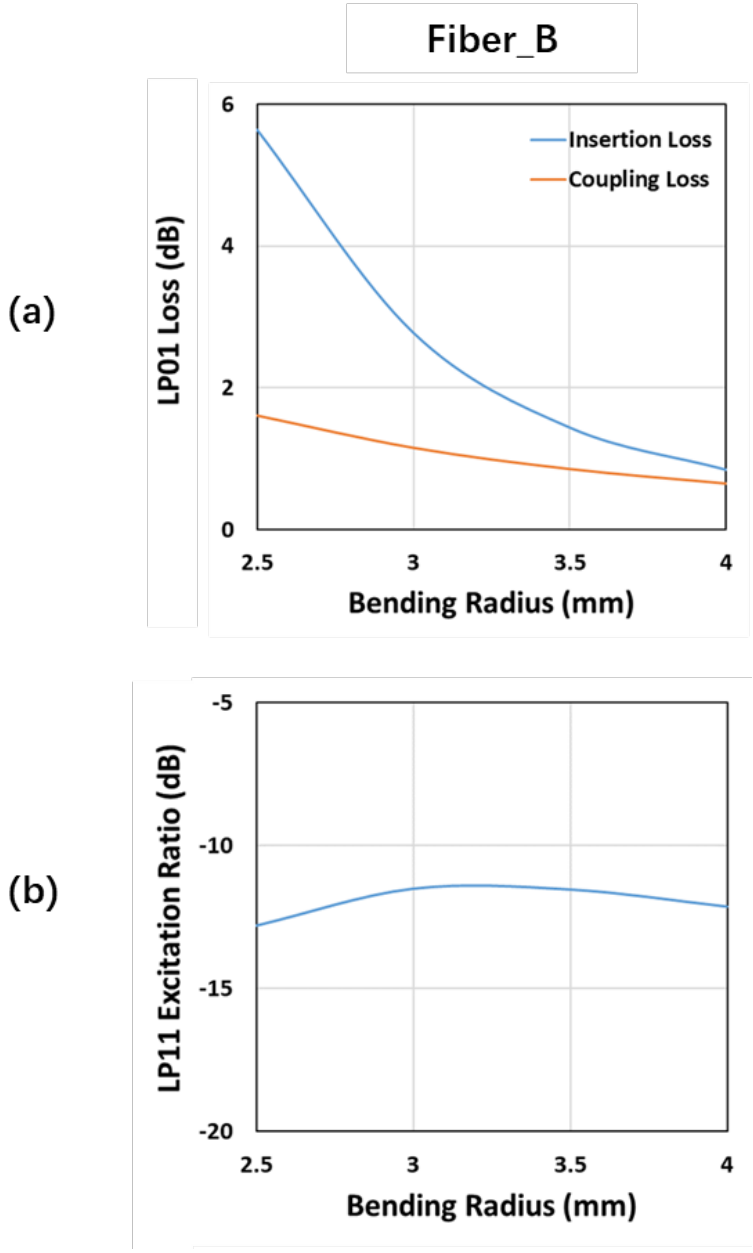


Fig. 4-8 Simulation result of straight-to-bent fiber connection based on the model of fiber_B

The blue line in Figure 4-8(a) represents the insertion loss, which corresponds to the total loss of the LP01 mode, encompassing both the coupling loss and bending loss. Therefore, the difference between the blue curve and the orange curve represents the bending loss. When the bending radius exceeds 3mm, the coupling loss surpasses the

bending loss. At this point, the excitation efficiency of the LP11 mode reaches approximately -10dB, signifying its significant impact. To verify the simulation results, we conducted an experimental setup involving bending the fiber 90 degrees. The experimental configuration is as follows:

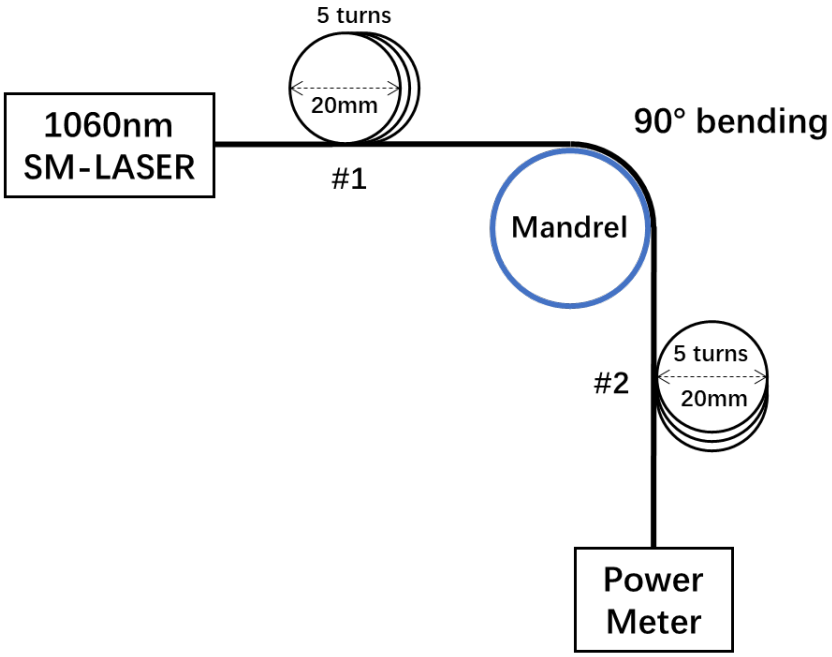


Fig. 4-9 Experiment set-up for straight-to-bent fiber coupling loss measurement

In our experimental setup, we aimed to verify the coupling loss caused by a 90-degree bend by measuring the excitation of the LP11 mode. We bent the fiber 90 degrees on a mandrel with the desired radius to be tested. Two mode filters were introduced: one before and one after the 90-degree bend section. The first mode filter (#1) ensured that only the LP01 mode light entered the 90-degree bend section, as its loss to the LP01 mode was negligible. By measuring the power difference when the second mode filter (#2) was used and not used, we could determine the extent of LP11 mode excitation caused by the 90-degree bend.

During our experiments, we attempted various bending radii below 4mm but did not observe any excitation of the LP11 mode. Upon analysis, we identified that the gradual change in the bending radius of the fiber due to mechanical bending-induced stress played a significant role [6]. This change led to a reduction in coupling losses. However, in the simulation, there was no smooth transition between straight fibers and curved fibers, as illustrated in the figure below:

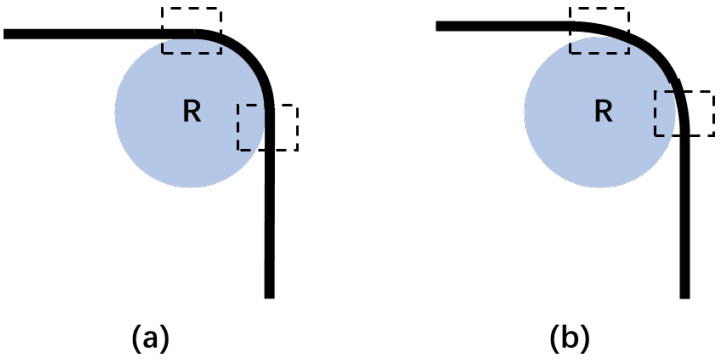


Fig. 4-10 Schematic diagram of sharp bending (a) and gradual bending (b)

The figure provided illustrates the connection between the straight fiber and the bent fiber, with the black dashed box indicating the connection region. Fig. 4-10(a) represents sharp bending, while Fig. 4-10(b) represents gradual bending. In our analysis, we assume that the radius of the 90-degree bending section is R, corresponding to a curvature $C = 1/R$. The bending radius of straight fibers is considered as infinite, resulting in a curvature of $C = 0$. In the case of sharp bending, the fiber experiences a sudden jump in curvature from 0 to $1/R$. Conversely, during gradual bending, the curvature gradually increases from 0 to $1/R$ over the length of the fiber. The longer the length, the slower the change in curvature, leading to reduced coupling losses. We established a model of gradual bending and performed calculations to determine the coupling loss, as depicted in the figure below:

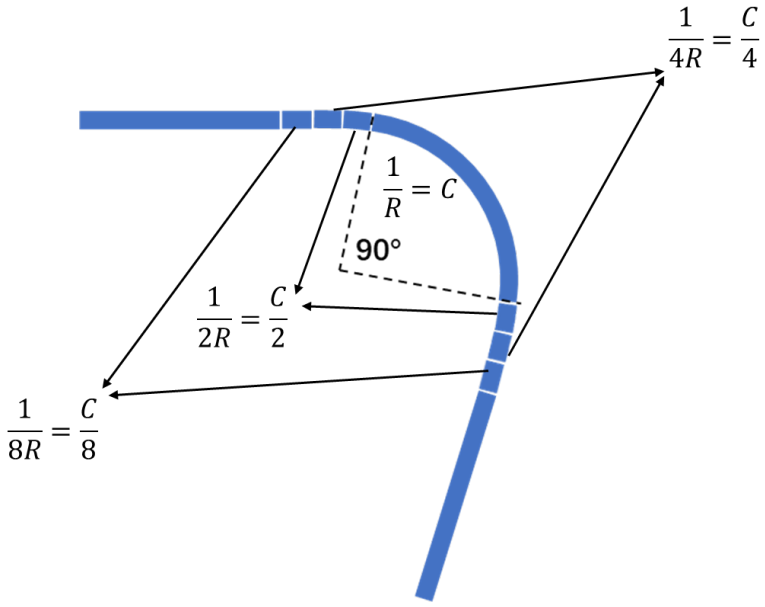


Fig. 4-11 Simulation model of gradual bending

To investigate the coupling loss in the transition region between the straight fiber and the 90-degree bend, we introduced three sections of fiber with larger bending radii. Assuming the radius of the 90-degree bending part is $R$, the bending radii of the transition fibers were set as $2R$, $4R$, and $8R$, respectively, starting from the closest to the 90-degree bend. This allowed for a gradual change in curvature, with curvature changes of $0$, $C/8$, $C/4$, $C/2$, and finally $C$, where $C$ represents the curvature of the 90-degree bend.

In our calculations, we selected R=3.5mm as an example and assumed that each section of the transition fiber had a length of 0.1mm. This configuration ensured that the total length of the transition fiber was much shorter than the length of the 90-degree bending part, which aligns with our experimental setup. We compared the results of the calculations with and without the transition fiber for R=3.5mm. The findings are summarized below:

Table 4-3 Comparison of LP01 coupling loss and LP11 excitation ratio between sharp

bending and gradual bending

| | Sharp bending | Gradual bending |
|---|---|---|
| Insertion loss (dB) | 1.44 | 0.737 |
| Coupling loss (dB) | 0.86 | 0.152 |
| LP11 excitation ratio (dB) | -11.54 | -24.93 |

Because we set R=3.5mm, the bending radii of the three transition fibers are 7mm, 14mm, and 28mm, respectively. According to the results in Chapter 3, the bending loss on LP01 mode of the three transition fibers can be ignored. Therefore, the bending losses of both the sharp bending case and the gradual bending case are only attribute to their 90-degree bending section. Thus, the difference in insertion loss between the two cases is solely due to changes in coupling loss. As can be seen, the coupling loss drops from 0.86dB to 0.15dB, which is a significant change. The excitation efficiency of the LP11 mode also dropped from -11.5dB to -24.9dB, it can be considered that the LP11 mode generated by coupling loss in gradual bending case is negligible.

The gradual bending model in Fig. 4-11 only sets three transition sections with progressively larger bending radii. The change in the bending radius is still step-like. Even so, it has significantly improved the suppression effect on coupling loss and LP11 mode excitation [7]. In actual situations, the gradient of the bending radius is continuous, and the generated coupling loss and LP11 mode would be even lower. This explains why we couldn't measure the excitation of the LP11 mode in experiment. Furthermore, eccentric connection between the straight fiber and the bent fiber also contributes to reducing coupling loss and LP11 mode excitation [8]. This type of connection, as shown in the figure, helps to align the mode fields and minimize the mode field mismatch, resulting in reduced coupling loss and LP11 mode excitation.

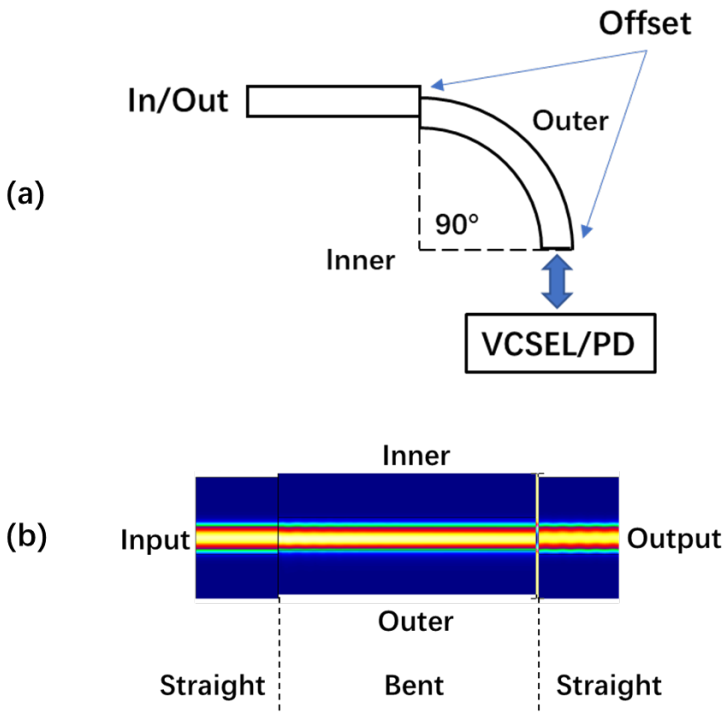


Fig. 4-12 Coupling loss decrease by offset connection between straight and bent fiber

In bent fibers, the mode field is skewed towards the periphery. Appropriately shifting the straight fiber outward can enhance the mode coupling efficiency, thereby diminishing loss. In Fig. 4-12(a), the offset is identical on either side of the bent fiber, and the mode field distribution as light propagates along the fiber is depicted in Fig. 4-12(b). The LP11 mode is virtually non-existent within the fiber, representing a significant improvement relative to Fig. 4-7(b).

We computed the optimal offset for bend radii of 2.5mm, 3mm, 3.5mm, and 4mm, yielding results of 1.6μm, 1.4μm, 1.2μm, and 1μm, respectively. Based on these optimal offsets, we calculated the coupling loss and the excitation efficiency of the LP11 mode under each bending radius. The resultant data are presented in the ensuing figure:

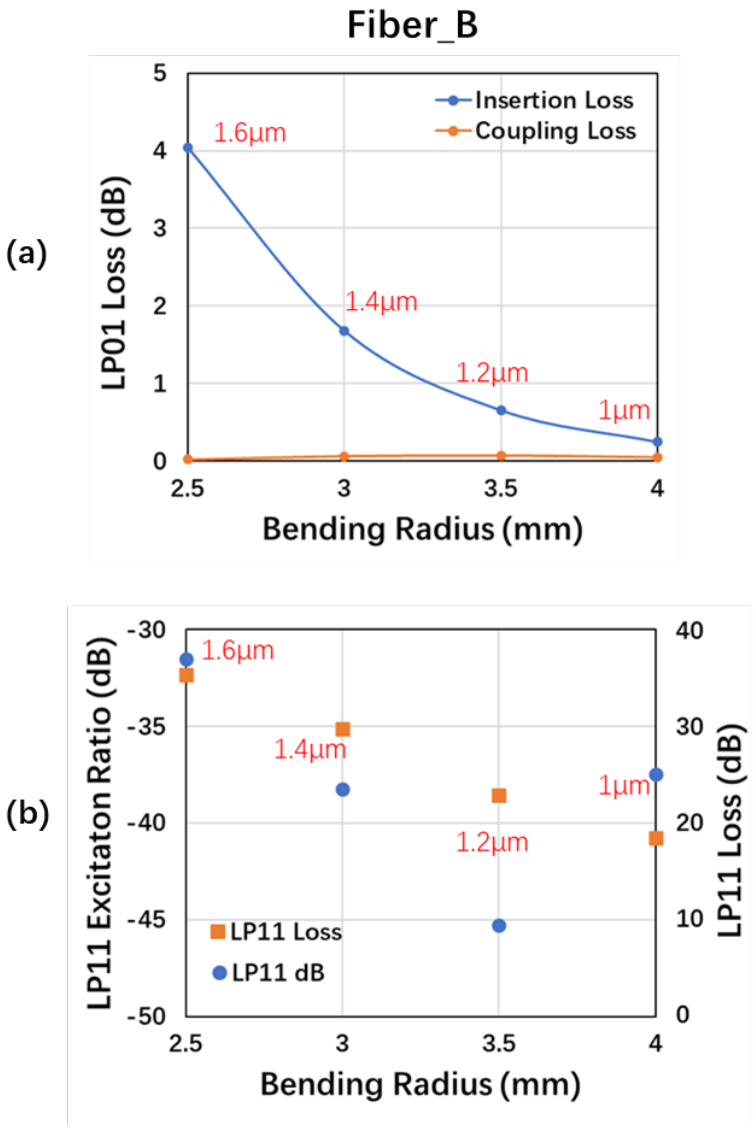


Fig. 4-13 Coupling loss and LP11 excitation ratio under optimal offset

As depicted in Fig. 4-13(a), under optimal offset, the coupling loss is mitigated to an inconsequential degree. Consequently, the resultant insertion loss corresponds to the bending loss. With a bending radius of 3.5mm, the insertion loss approximates 0.65dB, a value that aligns with the result from fiber_B in Fig. 4-4. As for the LP11 excitation ratio, it remains under -30dB with optimal offset, an impact deemed negligible on system performance. Fig. 4-13(b) further demonstrates the LP11 loss for each bending radius under optimal offset. Remarkably, even at a bend radius of 4mm, a nearly 20dB loss

occurs, suggesting that the fiber array is capable of satisfactorily filtering the LP11 mode. Our simulation outcomes address the issues of coupling loss and LP11 mode excitation prompted by the straight-to-bent fiber junction within a 90-degree fiber array. The simulation results reveal that acute bending of the fiber can significantly affect product performance due to increased coupling loss. Potential mitigations for this issue may include facilitating a gradual bending of the fiber or offsetting the straight-to-bent fiber junction. Our computations of these two potential solutions suggest that both approaches can reduce the LP01 coupling loss and the LP11 excitation ratio to a negligible extent. This reveals the feasibility of employing a 90-degree fiber array as a mode filter.

## Reference in Chapter 4


4-1 M. Morimoto and M. Shinoda, "Small-radius 90/spl deg/-bent single mode fiber for optical interconnection," in OFC/NFOEC, 3 (2006).

4-2 D. Boivin, L. de Montmorillon, L. Provost, N. Montaigne, F. Gooijer, E. Aldea, J. Jensma, and P. Sillard, "Recent developments in bend-insensitive and ultra-bend-insensitive fibers," Opt. Components Mater. VII, (7598), 139-150 (2010).

4-3 S. Matsuo, M. Ikeda, and K. Himeno, "Bend-insensitive and low-splice-loss optical fiber for indoor wiring in FTTH," in Optical Fiber Communication Conference (OFC), ThI3, 1-3 (2004).

4-4 T. Konishi, T. Nakanishi, and T. Hayashi, "Optical fiber, optical fiber cord, and optical fiber cable," US Patent 8,724,954, May 13 (2014).

4-5 A. A. Juarez, E. Krune, S. Warm, C. A. Bunge, and K. Petermann, "Modeling of mode coupling in multimode fibers with respect to bandwidth and loss," J. Lightw. Technol., (32), 1549-1558 (2014).

4-6 A. G. L. Junior, A. Frizera, and M. J. Pontes, "Analytical model for a polymer optical fiber under dynamic bending," Opt. Laser Technol, (93), 92-98 (2017).

4-7 T. Kumagai, N. Matsushita, Y. Mitose, Y. Kaneuchi, A. Kataoka, and T. Nakanishi, "Optical fiber array with 90-Degree bend for silicon photonics chip coupling," SEI Tech. Rev. (89), 12 (2019).

4-8 T. Kitoh, N. Takato, M. Yasu, and M. Kawachi, "Bending loss reduction in silica-based waveguides by using lateral offsets," J. Lightw. Technol., (13), 555-562 (1995).

# Chapter5

# Modal noise measurements and transmission characteristics of 1060nm standard single-mode fiber transmission

In this chapter, we will conduct a rigorous experimental evaluation of modal noise in a transmission system based on traditional single-mode fiber, utilizing a 1060nm single-mode Vertical Cavity Surface Emitting Laser (VCSEL). This evaluation will be carried out under both Continuous Wave (CW) and NRZ modulation conditions. The variations in noise levels will be quantified by measuring the Root Mean Square (RMS) of the received power. Simultaneously, we will investigate the effects of the bent fiber mode filter on the system. The empirical results from these experiments will be compared with the theoretical predictions presented in Chapter 2, serving as a validation of the two-mode transmission model we proposed.

## 5.1 Experiment set-up

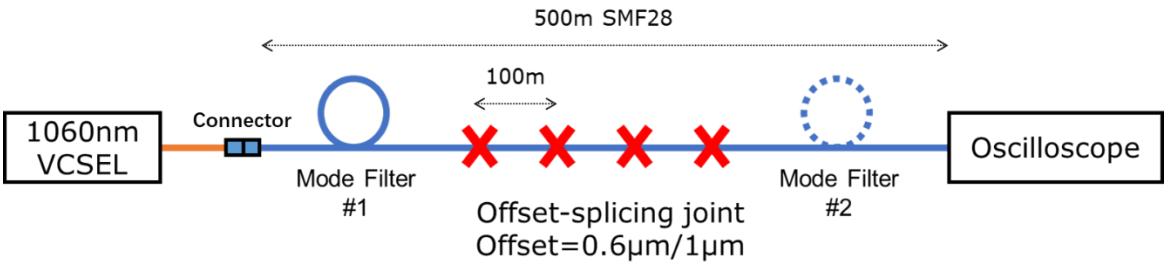


Fig. 5-1 Experiment set-up for modal noise measurement

Fig. 5-1 delineates the experimental apparatus for modal noise assessment. The light

source employed is a 1060nm single-mode VCSEL, while the receiver is an oscilloscope furnished with an 86105D module for the measurement of optical power and RMS values. The specifics of the light source and oscilloscope will be expounded in the subsequent sections.

The 1060nm single-mode VCSEL emits light that is funneled into a lensed fiber (depicted in orange). This lensed fiber is interfaced with a conventional single-mode fiber via a fiber connector. To counteract the influence of higher-order modes incited by coupling loss from the connector, the fiber is looped five times into a 10mm radius to serve as a mode filter (#1), after the fiber connector.

The fiber being scrutinized is a 500m-long SMF28-ULTRA, partitioned into five sections and reconnected through lateral-offset splicing, with uniform offsets at the four splicing junctures. Two separate experiments were performed, one with an offset of 1μm and the other with 0.6μm, yielding coupling losses of 0.3dB and 0.2dB respectively.

Another mode filter (#2), based on bent fiber and mirroring the configuration of #1, is employed preceding the oscilloscope. The efficacy of the mode filter is verified through comparing the modal noise both with and without the utilization of the #2 mode filter.

### *5.1.1 1060nm single-mode VCSEL*

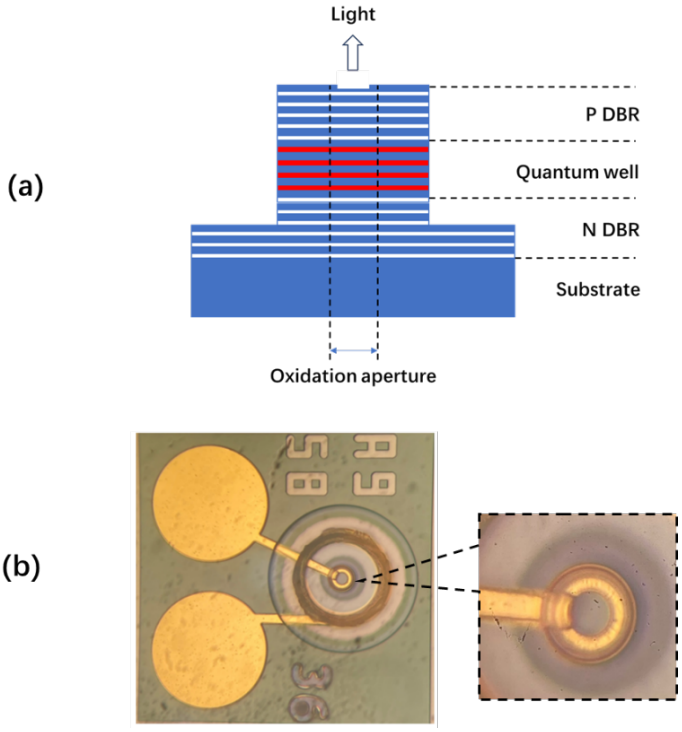


Fig. 5-2 Schematic structure of 1060nm single-mode VCSEL

The schematic structure of the metal-aperture Vertical Cavity Surface Emitting Laser (MA-VCSEL) is illustrated in Fig.5-1(a) [1]. The VCSEL comprises six pairs of Distributed Bragg Reflectors (DBRs) at the top and 30 pairs at the bottom. The etching depth is as minimal as 30nm, and the oxidation aperture diameter measures 5μm. The device operates at a wavelength of 1060 nm. Surface relief etching is implemented at the top to control the lateral modes, ensuring single-mode light output. Fig.5-1(b) provides a photograph of the VCSEL device, with the magnified central part corresponding to the surface relief structure.

To validate the single-mode operation of the VCSEL, we performed spectral measurements, as presented in the subsequent figure. The result shows an over 30dB side-mode suppression ratio (SMSR) which could confirm our VCSEL has excellent single-

mode characteristic, with the center wavelength approximately located at 1061 nm.

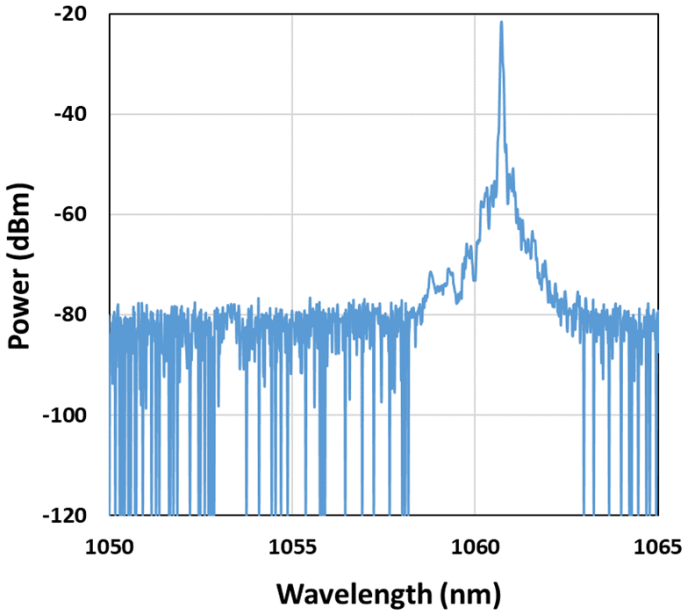


Fig. 5-3 Spectrum of 1060nm single-mode VCSEL

Since the spectrometer we employed is incapable of measuring the precise linewidth of the VCSEL, we had to infer the linewidth under different bias currents indirectly through calculations. The Light-Current (LI) curve of the VCSEL is presented in the following figure:

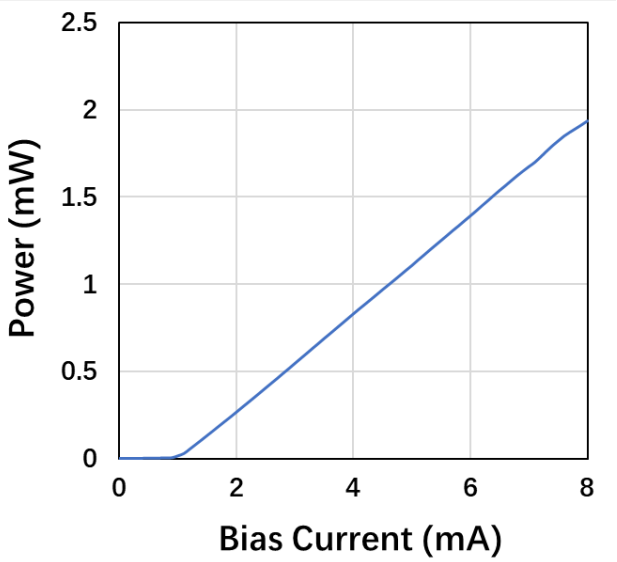


Fig. 5-4 L-I curve of 1060nm single-mode VCSEL

As depicted in Fig.5-4, the threshold current ($I_{th}$) of the VCSEL utilized in the experiment approximates 1mA. Its output power ($P_{out}$) manifests a strong linear correlation with the bias current. Given that a laser's linewidth is inversely related to its output power, and as per EQ.2-27 to EQ.2-29, modal noise is directly correlated to linewidth. Therefore, adjusting the bias current of the VCSEL can engender different levels of modal noise within the same experimental setup. In our experiment, we opted for bias currents of 4.5mA, 6mA, and 7.5mA, which correspond to output powers ($P_{out}$) of 0.97mW, 1.39mW, and 1.82mW, respectively.

The calculation formula for the linewidth of the VCSEL is as follows:

$$\Delta f = \frac{\beta \Gamma \eta_i I_{th} h\upsilon}{4\pi \tau_m P_{out} e}(1+\alpha^2) \qquad (5-1)$$

The parameters involved in the calculation of the linewidth are shown in the following table [2-5]。

Table 5-1 Linewidth calculation parameters

| | |
|---|---|
| Spontaneous emission factor $\beta$ | 0.002 |
| Optical confinement factor Γ | 0.038 |
| Internal quantum efficiency $\eta_i$ | 0.8 |
| Threshold current $I_{th}$ | 1 mA |
| Planck constant $h$ | $6.63 \times 10^{-34}$ J·s |
| Frequency $\upsilon$ | $2.83 \times 10^{14}$ Hz |
| Mirror energy loss $\tau_m$ | 1.23 ps |
| Elementary charge $e$ | $1.6 \times 10^{-19}$ C |
| Linewidth enhancement factor $\alpha$ | 2 |

Based on these parameters, the linewidth of the VCSEL at output powers ($P_{out}$) of 0.97mW, 1.39mW, and 1.82mW are 23.8MHz, 16.7MHz, and 12.7MHz, respectively. This result will be used in subsequent experiments.

### *5.1.2 86105-D oscilloscope*

In the experiment, the optical power and noise are measured using the 86105D optical-electrical detection module manufactured by Keysight, as shown in the following figure:


Fig. 5-5 86105D optical-electrical detection model [6]

In order to measure the modal noise, it is essential to know the thermal noise of the detector. Therefore, we have measured the thermal noise of the 86105D using the experimental setup shown in the following figure.

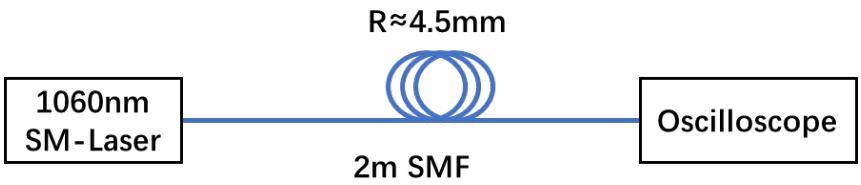


Fig. 5-6 Experiment set-up for thermal noise measurement

We employed a single-mode laser operating at a wavelength of 1060nm, with a threshold current of 15mA. The Root Mean Square (RMS) as measured by the oscilloscope represents the magnitude of noise within the system. However, the laser inherently possesses intensity noise [7], which necessitates its separation from the measurement outcomes to isolate the thermal noise. The intensity noise is contingent on the linewidth and output power of the laser, hence we subjected the laser to varying bias currents (BC) to manipulate its linewidth. The bias currents deployed in this experiment were 22mA, 33mA, and 40mA. In the experimental setup, fiber bending served as an attenuator, enabling the alteration of output power while maintaining a constant bias current, thus facilitating the calculation of relative intensity noise (RIN). The experimental results are demonstrated in the ensuing figure:

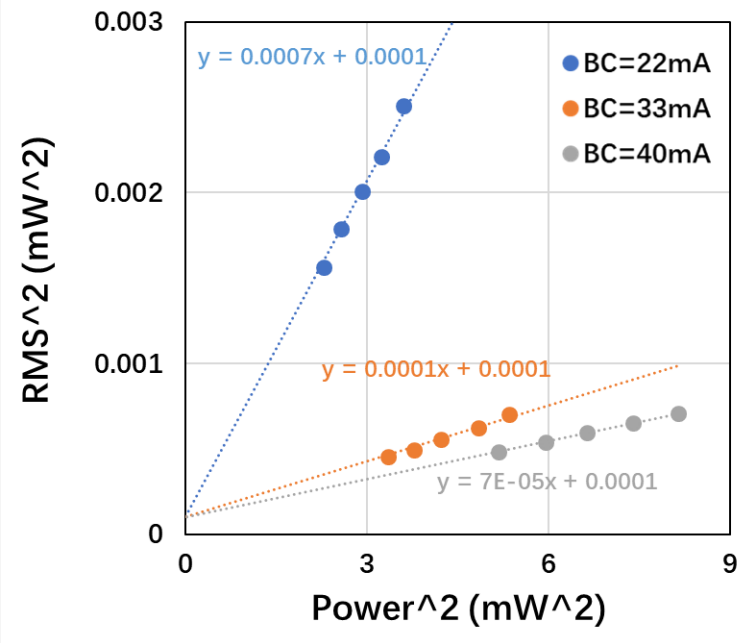


Fig. 5-7 Measurement result under different bias current (BC)

The measured RMS denotes the magnitude of the total noise, symbolized as $\sigma_T$. The intensity noise can be represented as the product of the Relative Intensity Noise (RIN) and the square of the output power, denoted as $\sigma_{RIN}^2 P^2$. We utilize the symbol $\sigma_0$ from the second chapter to represent the thermal noise. Their interrelationship is satisfied by the following formula:

$$\sigma_T^2 = \sigma_{RIN}^2 P^2 + \sigma_0^2 \qquad (5-2)$$

As deduced from Eq.5-2, the square of the RMS demonstrates a linear relationship with the square of the output power. The intercept of this function correlates to the square of the thermal noise. In Fig. 5-7, all three test outcomes exhibit an exemplary linear correlation. Based on these functional expressions, the thermal noise can be estimated as 0.01mW.

## 5.2 Modal noise measurement under CW condition

Grounded on the experimental setup depicted in Fig.5-1, we carried out measurements of modal noise under continuous wave (CW) conditions. We have calculated the modal noise in Chapter 2, a calculation that is based on the assumption of the worst-case scenario. This assumes that the polarization directions of each light source involved in the interference are aligned, and that the interference is in quadrature, thus generating the maximum modal noise as stipulated by Eq.2-16 and Eq.2-17. The comparison of calculation and experiment results are demonstrated in the following figure:

(a)

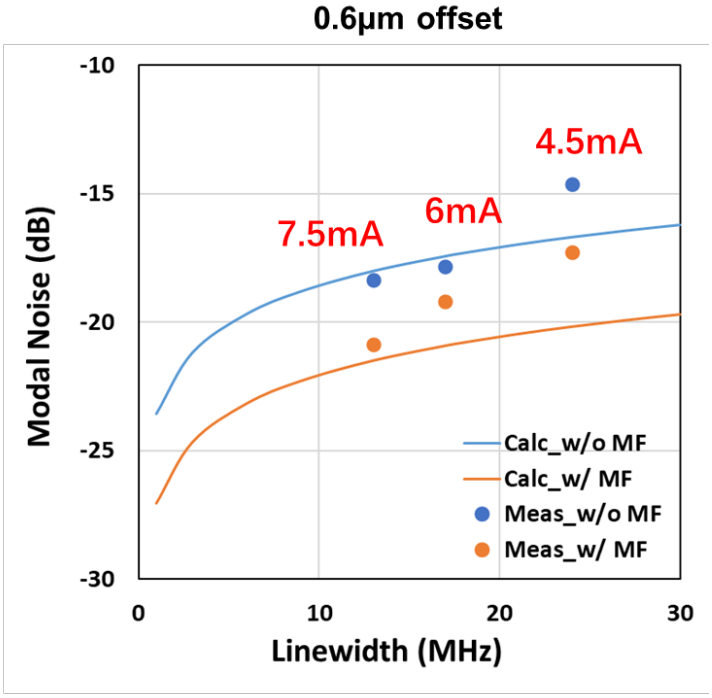


(b)

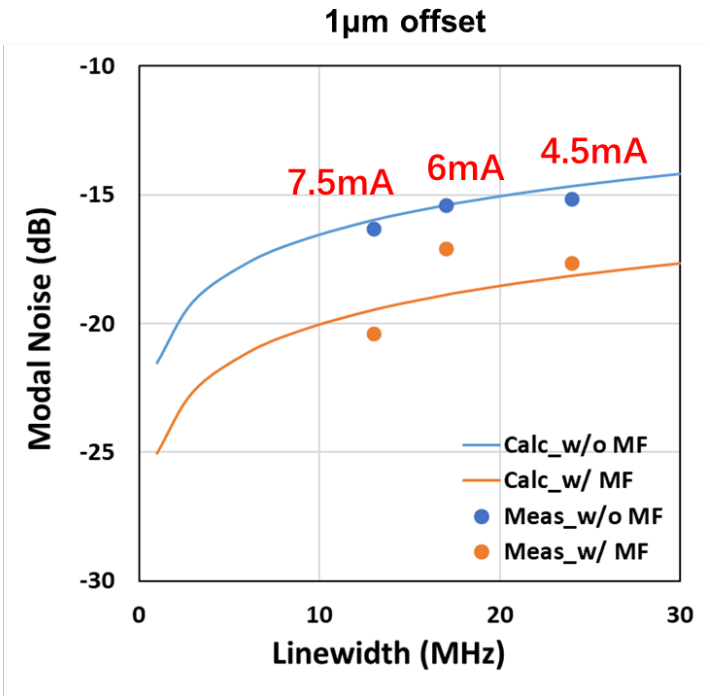


Fig. 5-8 Comparison of modal noise measurement results and calculated results. (a) Offset of 0.6μm, (b) Offset of 1μm.

Fig.5-8(a) and Fig.5-8(b) illustrate the results when the splicing joint offset is 0.6μm and

1μm, respectively. The modal noise unit is in dB, calculated by comparing the modal noise with the received optical power. The RMS of the optical power measured by the oscilloscope represents the system's total noise. In section 5.1.2, we determined the oscilloscope's thermal noise. By subtracting this from the total noise, we can ascertain the modal noise.

In each experiment, three sets of results were measured using three distinct bias currents of 4.5mA, 6mA, and 7.5mA. Thus, as per the calculation in section 5.1.1, the laser linewidth corresponding to each set of results is 23.8MHz, 16.7MHz, and 12.7MHz, respectively. Each set of measurement results contains 2 data points, represent the measured noise with and without using a mode filter.

Both experiments reveal that the overall trend of modal noise variation with laser linewidth, as demonstrated by the measurement results, aligns with the calculation results. This outcome validates the efficacy of our established theoretical model. Moreover, the experimental results demonstrate a decrease in modal noise post the use of the mode filter, attesting to the mode filter's effectiveness in enhancing the transmission capacity of the 1060nm single-mode optical communication system based on conventional single-mode fiber.

## 5.3 Eye-pattern test based on OOK-NRZ/PAM4 modulation

To further corroborate our theoretical model and the effectiveness of the mode filter, we conducted a data transmission experiment based on OOK-NRZ and PAM4 modulation. The experimental setup mirrored that of the CW experiment, with the exception that, in this experiment, we only utilized the test fiber with a splicing joint offset of 1μm.

We performed tests based on 50Gb/s and 70Gb/s NRZ modulation and 100Gb/s PAM4

modulation. The pre-equalizer was used in the experiment. The eye patterns have been measured with and without the utilization of a mode filter. Furthermore, we connected the lensed fiber (the orange fiber in Fig.5-1) directly to the oscilloscope to conduct a back-to-back experiment as a reference. The results of these experiments are displayed in the subsequent figure:

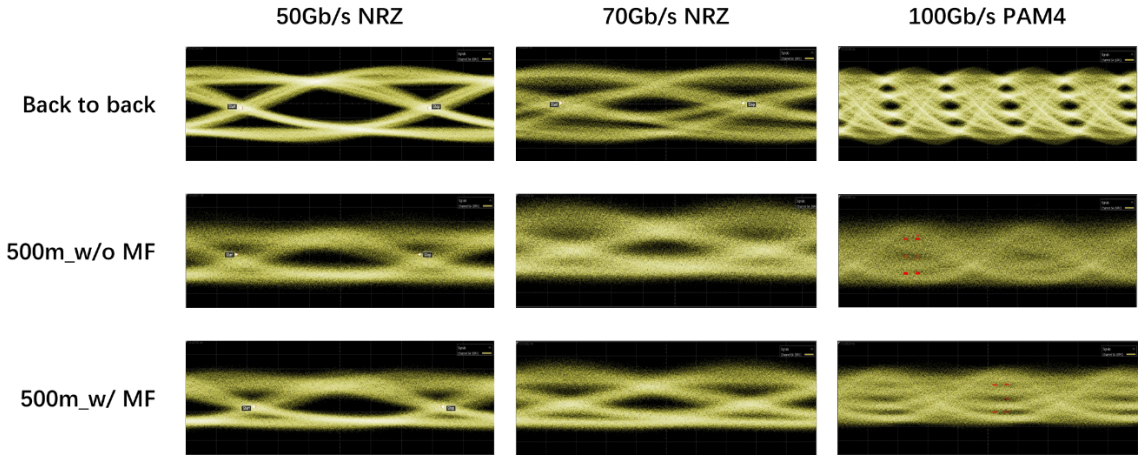


Fig. 5-9 Eye-pattern test result w/ and w/o mode filter

In the three experiments, a noticeable degradation in eye pattern quality was observed when the signal traversed after 500m test optical fiber compared to the back-to-back experiments. This degradation was especially pronounced for the 100Gb/s PAM4 trials. Utilization of a mode filter significantly improved the signal's eye pattern quality. However, since the mode filter cannot mitigate modal noise caused by fundamental mode, and the attenuation and coupling loss introduced during transmission also contributes to a decrease in the Q value, the quality of the eye pattern cannot be restored to the same level as in the back-to-back experiments. This observation aligns well with our previous theoretical analysis. Moreover, based on our computational model, the modal noise of the fundamental mode is influenced by the signal intensity. The modal noise for the “mark” signal should be higher than that for the “space” signal. As can be observed in the eye

pattern post-mode filter application, the upper eye is thicker than the lower eye, indicating higher noise for the “mark” signal compared to the “space”. This also consistent with our expectations.

In the experiments, since a hard electrical filter was not employed, the thermal noise is independent of the signal rate. We calculated the thermal noise for both 50Gb/s and 70Gb/s experiments. In the back-to-back experiments, the signal-to-noise ratios for the 50Gb/s and 70Gb/s were 41.8 and 28.8, respectively. The calculations indicate that the thermal noise for both experiments is strikingly similar, with an average value of -19.08dBm.

Taking into account the thermal noise, we calculated the maximum and minimum Q value for the 50Gb/s and 70Gb/s experiments, both with and without the use of a mode filter. We then compared these calculated results with our experimental findings. The outcomes are illustrated in the subsequent figure.

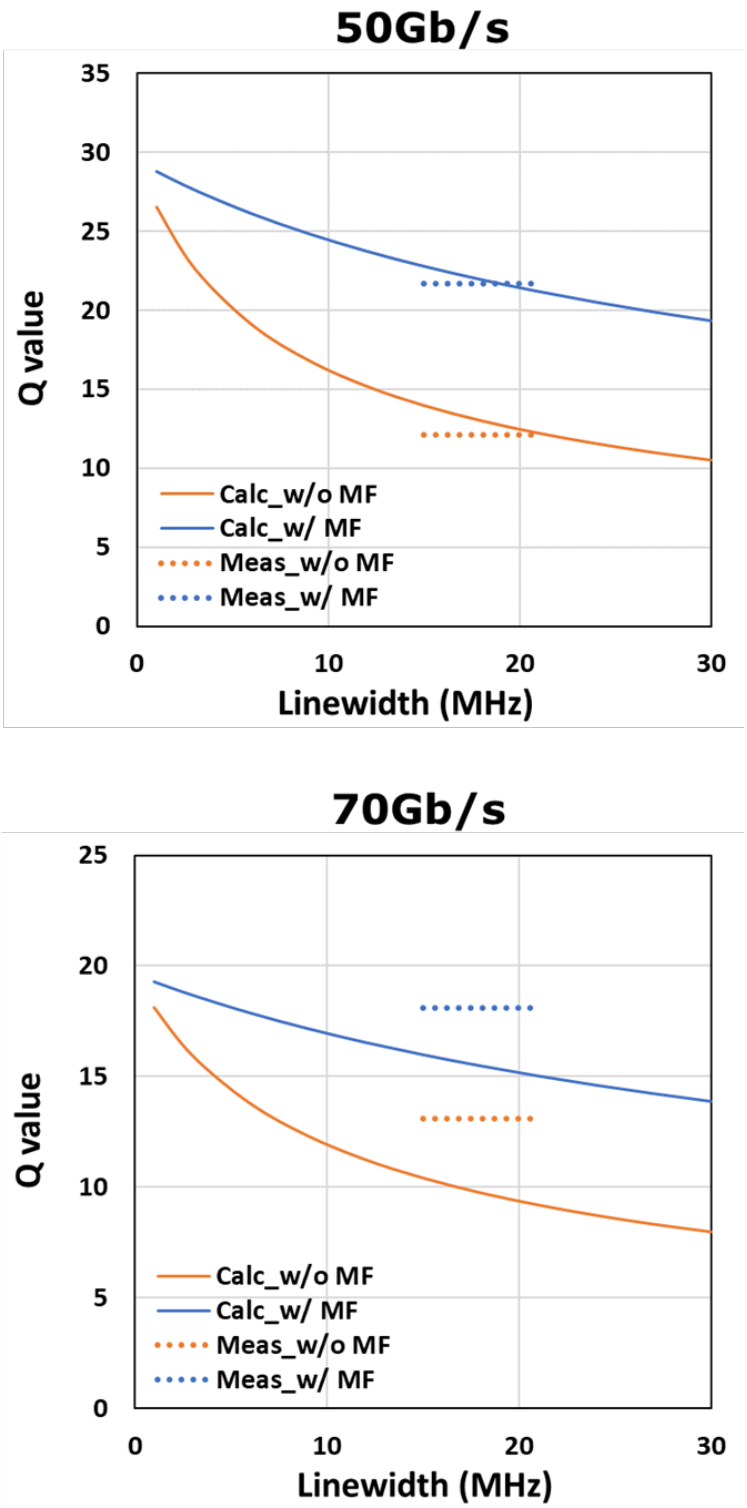


Fig. 5-10 Comparison of SNR measurement results and calculated results w/o and w/ using mode filter

Given the inability to obtain an accurate laser linewidth, the measured Q values cannot be represented as a singular point on the graph. Instead, they are depicted with dotted lines across a certain linewidth range.

According to our calculations, the linewidth of the laser we employed falls between 16MHz and 21MHz. In the context of data transmission at 50Gb/s, it is evident that when the laser linewidth is 20MHz, the experimental measurements align perfectly with the calculated results. However, in the 70Gb/s scenario, the measured values exceed the calculated ones. This discrepancy may be attributed to our calculations being based on a worst-case scenario, which might not manifest in actual experimental conditions, thus leading to higher measured values. Nevertheless, the closeness in the Q-value difference between the two sets of data still validates the reasonableness of the calculations. This observation underscores the reliability of our theoretical approach, even when confronted with the complexities of higher data rate transmissions.

Across both experiments, the deployment of the mode filter resulted in an average enhancement of the Q value by 1.8dB. As the transmission distance is elongated or the number of fiber connectors augmented, the adverse impact of noise on the Q value intensifies. In such scenarios, the significance of the mode filter becomes even more pronounced. These transmission experiments not only vindicate the veracity of our established transmission model but also illuminate the pivotal role of mode filters in elevating the SNR for data transmission systems based on G.652 standard single-mode fibers operating at 1060nm.

## Reference in Chapter 5

5-1 C. Ge, B. Zhang, X. Gu, S. Kinoshita, and F. Koyama, "Full 3-inch Wafer

Processed 1060 nm Single-mode Transverse Coupled-cavity VCSEL for Data Transmission in Standard 1300nm Single-mode Fiber," Optical Fiber Commun. Conf., Th2A-9, (2023).

5-2 H. Dalir, "Study on High Speed VCSEDs Based on Lateral Resonator Integration for Optical Interconnects,", 東京工業大学 (2014).

5-3 D. Kuksenkov, S. Feld, C. Wilmsen, H. Temkin, S. Swirhun, and R. Leibenguth, "Linewidth and α-factor in AlGaAs/GaAs vertical cavity surface emitting lasers," Appl. Phys. Lett. (66), 277-279 (1995).

5-4 M. Novarese, F. Bertazzi, P. Debernardi, M. Goano, and A. Tibaldi, "Linewidth modelling and measurements of single-mode VCSELs,", Politecnico di Torino (2019).

5-5 T. Kondo, M. Arai, M. Azuchi, T. Uchida, A. Matsutani, T. Miyamoto, and F. Koyama, "Singlemode fibre transmission using 1.2 μm band GaInAs/GaAs surface emitting laser," Electron. Lett. (38), 901-903 (2002).

5-6 “https://www.testunlimited.com/productDetail.aspx?product_id=4845”

5-7 R. Michalzik, "VCSEL fundamentals," in VCSELs: Fundamentals, Technology and Applications of Vertical-Cavity Surface-Emitting Lasers, 19-75, Springer (2012).

# Chapter6

# Conclusion

This study addresses critical phenomena such as mode coupling and modal noise within optical communication systems based on conventional single-mode optical fiber and 1060nm single-mode VCSEL, employing both theoretical analysis and empirical verification. Initially, a dual-mode optical transmission model was constructed, facilitating an in-depth analysis of the mode coupling process. Subsequent discussions centered around the genesis of modal noise, culminating in a quantitative analysis via computations. Furthermore, the impact of modal noise on the system bit error rate (BER) and the resultant power penalty were computed. The proposed resolution to issues stemming from the LP11 mode-generated modal noise is the deployment of a mode filter, the effects of which were predicted in tandem with the dual-mode transmission model.

Empirically, an experimental system was established employing a 500m conventional single-mode fiber and a 1060nm single-mode VCSEL. The fiber showcased controllable coupling loss facilitated by lateral-offset splicing, simulating coupling loss due to mode field mismatch within real-world fiber-optic transmission systems. Initial measurements focused on system modal noise under continuous wave (CW) conditions, yielding results consistent with the calculations. Furthermore, in data transmission experiments based on various modulation rates and techniques, the eye pattern results vividly demonstrated the impact of modal noise on the system's signal-to-noise ratio. The efficacy of the mode filter in enhancing the quality of the eye pattern was also evident. By comparing the calculated and measured signal-to-noise ratio, further validation was provided for the

accuracy of our transmission model.

The implementation and effect of mode filters were evaluated in both CW and eye-pattern experimental scenarios, conclusively demonstrating that mode filters effectively diminish modal noise and enhance system transmission capacity.

This study outlines the design of two mode filters - a bending fiber-based mode filter and a compact mode filter premised on a 90-degree fiber array, each catering to different scenarios.

For the bending fiber-based mode filter, a simulation model was established to compute bending loss, a result subsequently validated through experimentation. The experiment proposed the use of lateral-offset splicing fiber to excite the LP11 mode, a method the efficacy of which was scrutinized both theoretically and empirically.

Concerning the compact model filter based on a 90-degree fiber array, preliminary calculations of the bending loss of three fiber types adhering to G.652-D, G.657-A1, and G.657-B3 standards assessed its feasibility. Findings concluded that the fiber adhering to the G.657-B3 standard, due to its low bending loss, could not function as a mode filter. The bending loss of the fibers adhering to the remaining two standards was then measured empirically, and results concurred with the computations.

Moreover, given that 90-degree fiber arrays typically employ smaller bending radii (less than 4mm), the coupling loss incurred at the junction between the straight and bending fiber is significant and warrants consideration. This issue was analyzed based on the simulation model, alongside the effects of two strategies for mitigating coupling loss - gradual bending and eccentric connection. Both methods proved effective in reducing bending fiber-induced coupling loss. Selecting an appropriate fiber type and bending radius allows a 90-degree fiber array to achieve an insertion loss less than 1dB and an

LP11 mode rejection ratio exceeding 20dB.

In summary, this research offers theoretical and pragmatic insights into understanding and managing modal noise issues within optical communication systems based on conventional single-mode optical fiber and 1060nm single-mode VCSEL. These results contribute to the optimization and enhancement of optical communication system performance, laying a firm theoretical groundwork for further investigation and application of innovative optical communication technologies.

## Reference in Chapter 6


6-1 K. Li, X. Chen, J. Ko, J. E. Hurley, J. S. Stone, K. J. Park, B. Y. Kim, and M.-J. Li, "25Gb/s Mode Division Multiplexing VCSEL Transmission over Two Modes Using Standard Single-Mode Fiber at 850 nm," in Proc. OECC, M3F-2 (2021).

6-2 N. Hanzawa, K. Saitoh, T. Sakamoto, T. Matsui, S. Tomita, and M. Koshiba, "Demonstration of mode-division multiplexing transmission over 10 km two-mode fiber with mode coupler," in Proc. OFC, OWA4 (2011).

6-3 K. Li, X. Chen, J. Ko, J. E. Hurley, J. S. Stone, K. J. Park, B. Y. Kim, and M.-J. Li, "Mode division multiplexed 850-nm single-mode VCSEL transmission using standard single-mode fiber," IEEE Photonics Technol. Lett., 33(22), 1231–1234 (2021).

# Publication list

## (a) Journal Papers (as first author)

[J-1] Boxuan Zhang, Xiaodong Gu, Chang Ge and Fumio Koyama, "Modal Noise Suppression and High-speed Data Transmission in Standard Single-mode Fiber using 1060nm Single-mode VCSEL and Mode Filter," Chinese Optics Letters, 2024

[J-2] Boxuan Zhang, Xiaodong Gu, Susumu Kinoshita and Fumio Koyama, "Bending-Fiber Mode Filter for 1060nm Data Transmission in Standard Single-Mode Fiber," Jpn. J. Appl. Phys. 2024.

[J-3] Boxuan Zhang, and Fumio Koyama, "Filter in Compact Mode Constructed Using an Optical Fiber Array with a 90-Degree Configuration," IEICE Electronics Express, 2024.

## (b) International Conferences

[I-1] Chang Ge, Boxuan Zhang, Xiaodong Gu, Susumu Kinoshita and Fumio Koyama, "*Full 3-inch Wafer Processed 1060 nm Single-mode Transverse Coupled-cavity VCSEL for Data Transmission in Standard 1300nm Single-mode Fiber,*" Optical Fiber Communication Conference 2023, Th2A.9, 2023 (as co-author)

## (c) Domestic Conferences

[D-1] Boxuan Zhang, Xiaodong Gu, Susumu Kinoshita, Chang Ge and Fumio Koyama, "*Modal Noise Reduction in Data Transmission through Standard Single-Mode-Fiber with 1060nm Single-mode VCSEL and Mode Filter,*" 2023IEICE General Conference, C-3/4-60, 2023.

[D-2] Boxuan Zhang, Xiaodong Gu, Susumu Kinoshita and Fumio Koyama, "*Bending-Fiber Mode Filter Evaluation for 1060nm Data Transmission in Conventional Single-Mode Fiber*," 2022IEICE Society Conference, C-3/4-59, 2023

# 謝辞 Acknowledgement

At this juncture, I would like to extend my deepest gratitude to Professor Fumio Koyama. I am immensely grateful for the opportunity he offered me to pursue my doctorate in Japan. My past three years of study have been abundant in learning experiences, for which I have to thank Professor Koyama for his guidance and patience. This educational journey will forever hold a treasured place in my life.

Additionally, I owe a special thanks to Professor Kinoshita Susumu for his meticulous guidance concerning my research. He pointed out and addressed many issues I encountered during my study, and provided valuable assistance in editing my thesis, thereby enabling my research to progress smoothly.

Equally, I am grateful for the guidance and motivation provided by Professor Gu Xiaodong.

Beyond my esteemed professors, I would like to extend my appreciation to the secretaries in our research laboratory for their consistent support and assistance in various matters. Also, I am thankful for my fellow students: Dr. Li Ruixiao, Dr. Dong Liang, and Dr. Ge Chang. Throughout these three years, they have offered me considerable support and help in both academic and personal aspects, and I am proud to call them my friends.

Last but not least, my gratitude is directed towards my family. It is their unwavering support that enabled me to achieve all of this.